

MECHANICAL PROPERTIES AND MICROSTRUCTURE OF A HIGH CARBON STEEL

THÈSE N° 3089 (2004)

PRÉSENTÉE À LA FACULTÉ SCIENCES DE BASE

Institut de physique de la matière complexe

SECTION DE PHYSIQUE

ÉCOLE POLYTECHNIQUE FÉDÉRALE DE LAUSANNE

POUR L'OBTENTION DU GRADE DE DOCTEUR ÈS SCIENCES

PAR

Iva TKALCEC

ingénieur physicien, Université de Zagreb, Croatie
et de nationalité croate

acceptée sur proposition du jury:

Prof. W. Benoit, directeur de thèse
Prof. G. Kostorz, rapporteur
Dr D. Mari, rapporteur
Prof. C. Prioul, rapporteur
Dr M. Weller, rapporteur

Lausanne, EPFL
2004

Abstract

This work is focussed on a high carbon tool steel used for the production of files. The mechanical properties of the files depend on a hardening thermal treatment that produces a martensitic structure. Thus, the motivation for this work is technological: we want to understand the effects of two types of thermal treatment on the file's mechanical properties. The first is a traditional thermal treatment in a cyanide bath (CN), while the other is performed in a conveyor belt furnace (BF). The files resulting from BF treatment have sometimes a poorer performance. In order to improve the quality of BF files, we study the relationship between the mechanical properties and the microstructure resulting from a particular thermal treatment.

Transmission electron microscopy does not reveal a change in the microstructure produced by different thermal treatments, yet it does permit visualization of the complex material microstructure, consisting of a martensitic matrix with embedded carbides. On the other hand, thermoelectric power measurements allow a differentiation between CN and BF files in a fast and non-destructive manner: the measurements performed on the whole files show that the thermopower of BF files is lower. This result is attributed to a higher concentration of carbon soluted in the martensitic matrix. The yield stress and compression strength determined by compression testing, as well as the hardness measured by nanoindentation, are higher for the bulk of BF files, emphasizing the importance of soluted carbon in hardening the martensite.

The mobility of point defects and dislocations, and their interaction, are studied by mechanical spectroscopy. The martensitic structure is characterized by a rich internal friction spectrum comprising several overlapping relaxation and material transformation peaks. The internal friction measured at room temperature is related to an athermal background due to the interaction between soluted carbon and dislocations. This background is higher for BF files. The internal friction spectrum indicates that, upon heating above 375 K, the material structure irreversibly changes due to tempering processes.

Tempering effects on the material are studied combining several experimental techniques. A first stage of tempering, observed by differential scanning calorimetry, starts around 375 K and is related to carbon precipitation in the form of transition carbides. At this temperature, the thermopower and Young's modulus increase, and the internal friction and hardness decrease, implying that all these quantities are sensitive to soluted carbon. The hardness continuously decreases with tempering and no precipitation hardening is observed. A second stage of tempering is observed around 525 K, leading to cementite precipitation.

X-ray diffraction allows quantitative determination of the concentration of carbon in solid solution by measuring the tetragonality of the martensite lattice. The evolution of carbon content during tempering is compared to the evolution of internal friction and thermoelectric power revealing a strong correlation between these quantities. Internal friction measured at room temperature is directly proportional to the carbon content.

The measurement of the concentration of carbon by X-ray diffraction is used to determine the variation of carbon content in the file profile. Thermopower measurements indicate that BF files have a lower concentration of carbon in the teeth than in the bulk, while the opposite is found for CN files. This is confirmed by X-ray diffraction. Moreover, diffraction performed on the very surface of the teeth reveals a lower carbon concentration in BF than in CN files teeth, which is probably the origin of their lesser performance.

It can be concluded that the concentration of carbon in solid solution in martensite is responsible for the steel's hardness and therefore for its resistance to wear.

Version abrégée

Cette étude concerne principalement un acier à outils à haute teneur en carbone utilisé pour la production de limes. Les propriétés mécaniques des limes dépendent du traitement thermique de trempe qui produit une structure martensitique. Ainsi, la motivation de ce travail est d'abord technologique : il s'agit de comprendre les effets de deux types de traitement thermique des limes sur leurs propriétés mécaniques. Le premier est un traitement thermique traditionnel dans un bain de sel de cyanure (CN), tandis que le deuxième est effectué dans un four à bande (BF). Les performances des limes issues du traitement en four à bande sont parfois de qualité inférieure. Pour améliorer la qualité des limes de type BF, on étudie le lien entre les propriétés mécaniques et les microstructures issues d'un traitement thermique particulier.

La microscopie électronique à transmission ne montre pas de différences de microstructure entre traitements thermiques, mais elle permet de visualiser la microstructure complexe du matériau, formée d'une matrice martensitique entourant des carbures. D'autre part, la mesure du pouvoir thermoélectrique permet de différencier entre les limes de type CN et les limes de type BF de manière non-destructive. Des mesures effectuées sur des limes complètes montrent en effet que le pouvoir thermoélectrique des limes BF est inférieur. Ce résultat est attribué à une concentration supérieure du carbone en solution dans la matrice martensitique. La limite élastique et la résistance mécanique déterminées dans les tests de compression, de même que la dureté mesurée par nano-indentation, sont supérieures dans les limes de type BF, mettant ainsi en évidence l'importance du carbone en solution dans le durcissement de la martensite.

La mobilité des défauts ponctuels et des dislocations, ainsi que leurs interactions, sont étudiées par spectroscopie mécanique. La structure martensitique est caractérisée par un spectre de frottement intérieur très riche, résultant de la superposition de plusieurs pics de relaxation et de phénomènes de transformations du matériau. Le frottement intérieur mesuré à température ambiante est corrélé avec un fond athermique dû à l'interaction entre dislocations et carbone en solution. Le spectre de frottement intérieur indique qu'après chauffage au-dessus de 375 K la structure du matériau change de manière irréversible à cause du revenu de l'acier.

Les effets des revenus sur le matériau sont étudiés en combinant différentes techniques expérimentales. Un premier stade de revenu, observé par calorimétrie différentielle, commence autour de 375 K et est déterminé par la précipitation du carbone sous forme de carbures de transition. A cette température, le pouvoir thermoélectrique et le module de Young augmentent, tandis que le frottement interne et la dureté diminuent, ce qui implique que toutes ces quantités sont sensibles au carbone en solution. La dureté décroît de manière continue avec le revenu et l'on n'observe pas de durcissement par précipitation. Un deuxième stade de revenu est observé à 525 K, conduisant à la précipitation de cémentite.

La diffraction de rayons X permet de déterminer de manière quantitative la concentration de carbone en solution solide en mesurant la tétragonalité du réseau cristallin de la martensite. L'évolution de la teneur en carbone pendant le revenu est comparée avec l'évolution du frottement intérieur et du pouvoir thermoélectrique, montrant une étroite corrélation entre ces quantités. Le frottement intérieur mesuré à température ambiante est directement proportionnel à la concentration du carbone.

La diffraction de rayons X nous a permis également de déterminer le profil de concentration du carbone dans l'épaisseur de la lime. Les mesures de pouvoir thermoélectrique indiquent que les limes de type BF ont une concentration de carbone supérieure à l'intérieur de la lime tandis que l'effet opposé est présent dans les limes de type CN. Ceci est confirmé par diffraction de

rayons X. D'ailleurs, la diffraction effectuée à la surface des dents montre que la concentration de carbone dans les dents des limes de type BF est inférieure à celle des dents des limes de type CN, ce qui est probablement à l'origine de leur moindre performance.

On peut conclure que la concentration de carbone en solution solide dans la martensite est la source principale de la dureté de l'acier et par conséquent de sa résistance à l'usure.

Contents

Introduction	1
1. Martensitic steel: basic description	5
1.1 Crystal forms and interstitial solubility of iron: iron-carbon phase diagram ...	5
1.2 Martensitic transformation	6
1.3 Martensite morphology	9
1.4 Aging and tempering of martensite	9
2. Experimental techniques and relevant results from literature	11
2.1 Thermomechanical treatment during file processing	11
2.2 Microstructural analysis	11
2.2.1 Transmission electron microscopy	11
2.2.2 Atomic force microscopy	12
2.2.3 X-ray diffraction	13
Principles and experimental procedure	13
Relevant experimental results found in literature	14
2.3 Thermoelectric power	15
2.3.1 Principles and experimental procedure	15
2.3.2 Relevant experimental results found in literature	17
2.4 Mechanical tests	19
2.4.1 Compression	19
2.4.2 Nanoindentation	20
2.5 Mechanical spectroscopy	22
2.5.1 Phenomenology and definitions	22
2.5.2 Experimental installations	25
Free-free vibrating reed installation	26
Inverted torsion pendulum	27
2.5.3 Relevant experimental results found in literature	28
2.6 Differential scanning calorimetry	32
2.6.1 Principles and experimental procedure.	32
2.6.2 Relevant experimental results found in literature	33
3. Material properties at room temperature	35
3.1 Microstructure	35
3.1.1 Chemical composition	35
3.1.2 Atomic force microscopy	35
3.1.3 Transmission electron microscopy	36
3.2 Thermoelectric power	41

3.3	Mechanical tests	46
3.3.1	Compression	46
3.3.2	Nanoindentation	46
3.4	Conclusions	48
4.	Mechanical spectroscopy	51
4.1	Temperature spectra	51
4.1.1	High and low frequency spectra for martensite	51
4.1.2	Evolution of martensitic spectra with ageing and tempering	55
4.1.3	Internal friction for tempered martensitic, ferritic and bainitic structure	61
4.1.4	Effects of cold work on deeply tempered martensite and ferrite	61
4.1.5	Difference between thermal treatments of files	63
4.2	Discussion	65
4.3	Conclusions	73
5.	Tempering effects	75
5.1	Differential scanning calorimetry	75
5.2	Transmission electron microscopy	76
5.3	Thermoelectric power	77
5.4	Internal friction	80
5.5	Young's modulus	80
5.6	Nanoindentation	81
5.7	Discussion	82
5.8	Conclusions	85
6.	X-ray diffraction	87
6.1	Tempering effects on carbon concentration	87
6.1.1	Carbon content fitting	88
6.1.2	Correlation with TEP and internal friction	90
6.2	Variation of the amount of carbon in solid solution within a file	93
6.2.1	Experiments on the bulk and whole teeth of files	93
6.2.2	Experiments on the surface of file teeth	95
6.3	Conclusions	97
7.	Conclusion	99
	Bibliography	103
	Acknowledgments	109

Introduction

Despite constant development of new materials, steel is still one of the most reliable, most used, and most important materials of today. Depending on the chemical composition and the thermomechanical processing history during the manufacturing process, its mechanical properties can vary tremendously, covering an extensive range of strength, toughness and ductility. Steel can also be relatively cheaply manufactured in large quantities to very precise specifications. Therefore, it is not surprising that irons and steels account for over 80% by weight of the alloys used in industry [Honeycombe 1980]. Carbon steels are widespread materials because of the possibility to induce in them, by means of a rapid quenching, an extremely hard phase: martensite. Due to the complexity of the microstructure of martensitic carbon steels, their characterization often remains empirical.

The material in focus of this research is a high carbon tool steel used for the production of files. After shaping, the files are heated above the temperature of austenitization and then quenched. Traditionally, this heat treatment giving the necessary hardness and grip to the files, is performed manually in a cyanide salt bath. This process has a low productivity, it requires specially trained personnel and the costs of ecologically safe elimination of the waste are very high. The alternative is a heat treatment in a conveyor belt furnace, but the resulting quality is not always satisfactory. Therefore, the technological objective of this work is to understand the effects of thermal treatment on the mechanical properties of carbon steel designated for the production of files. The research is performed in collaboration with one of the most important file producers in the world, UMV Vallorbe, Switzerland.

The properties of interest for a file user are the grip (bite) of the file and its longevity. Each file produced in UMV Vallorbe passes through a quality control where the grip of the file is tested manually by an experienced staff. This process is rather subjective. A more quantitative measure for the mechanical performance can be obtained by tracing the filing behavior under controlled conditions (normal force and stroke speed). An instrument developed by UMV enables the measurement of the force necessary to move a file on a test material, i.e. the grip, and the mass of the test material removed by that action. The later quantity can be related to a file longevity if the test is performed during long enough time: after sufficient number of strokes the degradation of the file is reflected in the reduced increase of the total mass of the test material removed by filing. The results of a test performed on both cyanide bath (CN) and conveyor belt furnace (BF) treated files for a total number of 3000 strokes are presented in fig. 1 and fig. 2. As seen from the graphs, some types of files clearly show different performances. In fig. 1, we observe that the files treated traditionally have a superior grip (with the exception of the first

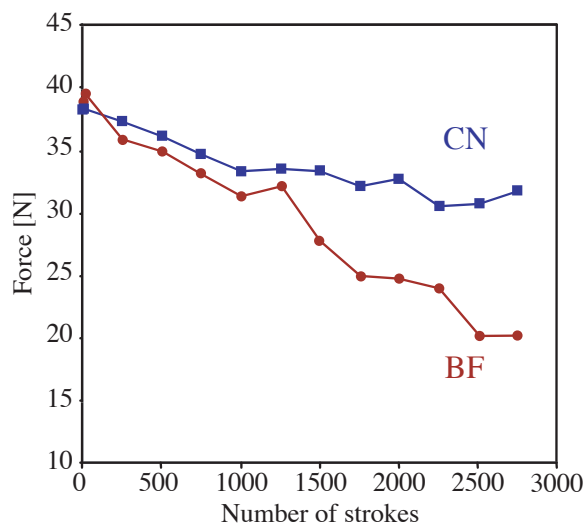


FIGURE 1. The force of the grip of the file as a function of the number of strokes performed on a test material under controlled conditions. The force decreases with use, but the decrease is smaller for CN files.

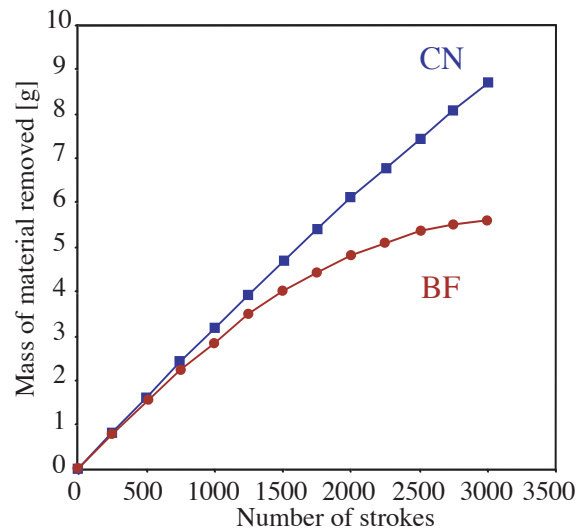


FIGURE 2. The mass of the test material removed by filing as a function of the number of strokes. CN files continue to remove the test material after 3000 strokes with almost the same rate as when new. BF files show deterioration starting from 500 strokes, and after 3000 strokes material is no longer removed.

few strokes). The grip is diminishing with the use, but this deterioration is more pronounced for the files treated in the conveyor belt furnace. Moreover, CN treated files keep removing the test material after 3000 strokes with almost the same efficiency as when they were new (fig. 2). On the contrary, although not showing a great difference at the beginning (up to 500 strokes), BF treated files with further use remove less and less material, reaching after 3000 strokes a state when the material is no longer removed by filing.

The files have the same initial chemical composition and by traditional testing methods (Vicker's hardness tests, observation of structure by optical or SEM microscope) the files resulting from two types of thermal treatment cannot be distinguished. Therefore, a more scientific approach, using various experimental techniques is necessary to relate macroscopic mechanical properties of steel to the microstructure emanating from a particular heat treatment. This thesis will show that the carbon in solid solution is responsible for the resistance of the material to deformation, in particular its hardness.

Because of the huge industrial and economical importance of steel and also its great complexity, a vast amount of literature exists covering the topic. Hence it is not possible to condense that huge amount of information in a traditional thesis chapter entitled "Bibliography". Chapter 1 aims to briefly describe the fundamental terminology related to martensitic steel starting from crystal structure and carbon solubility in pure iron, martensitic transformation and resulting martensite morphology.

Several experimental techniques are used in this work. Microstructural analysis is made complementing transmission electron microscopy (TEM), atomic force microscopy (AFM) and X-ray diffraction. Thermoelectric power is also used as a very sensitive probe of the microstructural state of the material. The mobility of defects (point defects and dislocations) and their interaction is studied by mechanical spectroscopy. Mechanical properties are investigated by nanoindentation and compression testing. Finally, differential scanning calorimetry is used for thermal analysis. A short description of each technique and the used parameters is given in Chapter 2 together with basic results obtained by other authors.

Experimental results are presented in four distinct chapters ending with a discussion and conclusions. Chapter 3 contains the description of the material properties at room temperature, showing the base differences between CN and BF treated files. A comparison of the measurements of thermoelectric power and the mechanical tests emphasizes the importance of the carbon in solid solution. Mechanical spectroscopy is thus used to get a better insight into the interactions of soluted atoms and dislocations and their mobility. An extensive study of the internal friction spectra is presented in Chapter 4. The internal friction spectra indicate that the material microstructure continuously changes at temperatures higher than 375 K. The effects of tempering, examined in more detail with a wide range of techniques, are described in Chapter 5. Finally, Chapter 6 contains the results of X-ray diffraction experiments, giving an explanation for the differences in mechanical properties resulting from the two types of thermal treatment and material evolution during tempering.

The scientific conclusions are summarized in Chapter 7.

Martensitic steel: basic description

There are evidences of use of meteoritic iron as early as around 2700 BC in Egypt, but it took another one and a half millennia for iron to start to replace bronze around 1200 BC [Maddin 1992]. In effect, pure iron has a lot of disadvantages in comparison with bronze: the melting temperature of iron is 1536°C, which was impossible to reach with the means of that time, therefore it could not have been cast, moreover, it corrodes easily. Although iron ores were more readily found than tin, which was required in addition to copper for making bronze, it was necessary to develop hardening processes in order to make iron more appealing. By dissolving carbon into iron (and thus forming steel) and quenching it to martensite, an immense improvement over bronze could be achieved.

The following paragraphs aim to briefly describe the basic terminology used further on in this thesis. The properties of steel are conditioned by certain properties of pure iron, namely its crystal structure and other element solubility characteristics. As it suffices to add carbon to iron to form steel, the carbon solubility will be regarded in more detail, without discussing the effects of other alloying elements. The thermal treatment producing the characteristic steel morphology will also be shortly discussed.

1.1 Crystal forms and interstitial solubility of iron: iron-carbon phase diagram

Pure iron is polymorphic: depending on temperature, two allotropic phases exist in solid state. One is body centered cubic (bcc) and the other face centered cubic (fcc). The bcc crystalline form (α -iron, ferrite) is stable from low temperatures to 910°C when it transforms to fcc (γ -iron, austenite). The austenite remains stable until 1390°C, and then it reverts to the bcc form, now called δ -iron, which is stable until the melting point of 1536°C. High purity iron is very weak (the resolved shear stress can be as low as 10 GPa for single-crystals, and 150 GPa for polycrystalline samples). The ability of iron to accommodate heavy interstitials, namely carbon and nitrogen, is mostly responsible for hardening effects.

It is interesting that the fcc structure, which is more closely packed than bcc, contains larger cavities. The largest voids in the fcc structure are situated at the centers of the cube edges, and are surrounded by six atoms in the form of an octahedron, therefore called octahedral (fig. 1.1a). The radius of the largest sphere fitting in this space is $0.41r$, r being the atomic

radius of iron (1.28 \AA). Second largest are tetrahedral interstices (fig. 1.1b), which can accommodate a sphere up to the radius of $0.23r$.

The largest cavities ($0.29r$) in the bcc structure are found between two edge and two central atoms forming a tetrahedron (tetrahedral sites, fig. 1.1d). The second largest ($0.15r$) are octahedral sites found at the centers of the cube faces and of the cube edges (fig. 1.1c). The surrounding atoms form a flattened octahedron.

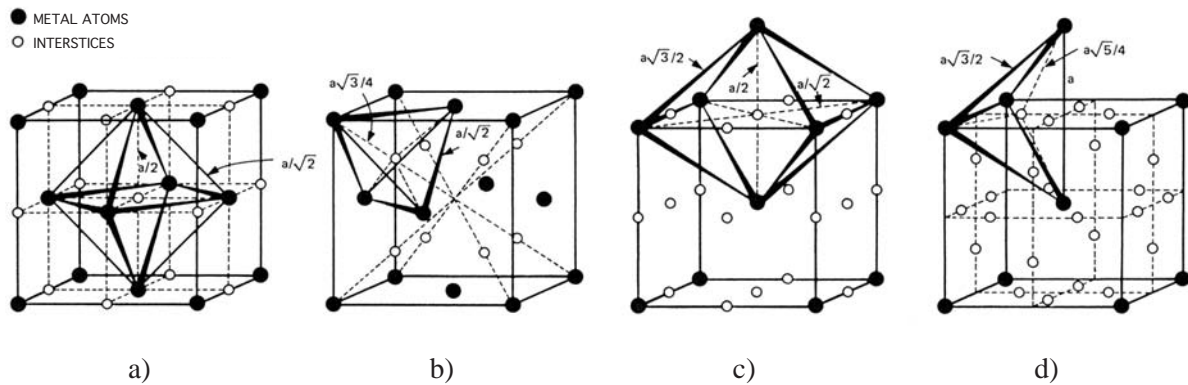


FIGURE 1.1. Interstitial voids in iron. Octahedral (a) and tetrahedral (b) voids in fcc structure. Octahedral (c) and tetrahedral (d) voids in bcc structure. Taken from [Leslie 1981].

The atomic radius of a carbon atom in iron is sufficiently small ($0.6r$) to enter the interstitial sites, however with some lattice distortion. The fact that there are larger interstitial cavities available in the fcc than in the bcc structure explains the much larger solubility of carbon in γ than in α -iron. The maximum carbon solubility in austenite reaches 2.04 wt.% at 1147°C , compared with 0.02 wt.% in ferrite at 723°C . These and other equilibrium features are best described by means of the iron-carbon phase diagram (fig. 1.2). It should be mentioned that the true equilibrium exists between iron and graphite (occurring in cast irons with 2-4 wt.% C). As graphite is difficult to obtain in steels, the metastable equilibrium between iron and cementite is considered. Cementite is an iron-carbide with the chemical formula Fe_3C and an orthorhombic crystal structure.

The much greater solubility of carbon is reflected in a much larger phase field of austenite than ferrite. For the carbon content higher than 0.008 wt.%, α -iron is accompanied by iron carbide. The transformation temperature of 910°C between austenite and ferrite for pure iron is progressively lowered by the addition of carbon to the eutectoid temperature of 723°C and the eutectoid composition of 0.8 wt.% C.

1.2 Martensitic transformation

Sufficiently rapid cooling of austenite containing carbon will prevent the formation of ferrite + cementite which would happen with adequately slow cooling, i.e. if the diffusion of carbon atoms is allowed. The carbon atoms soluted in austenite remain trapped, causing the tetragonal distortion of the bcc lattice and the formation of a very hard metastable phase: martensite. The martensitic transformation in steel is just one example of a more general phenomenon of martensitic transformations described as shear-dominant, lattice-distortive, diffusionless transformations occurring by nucleation and growth [Olson 1992].

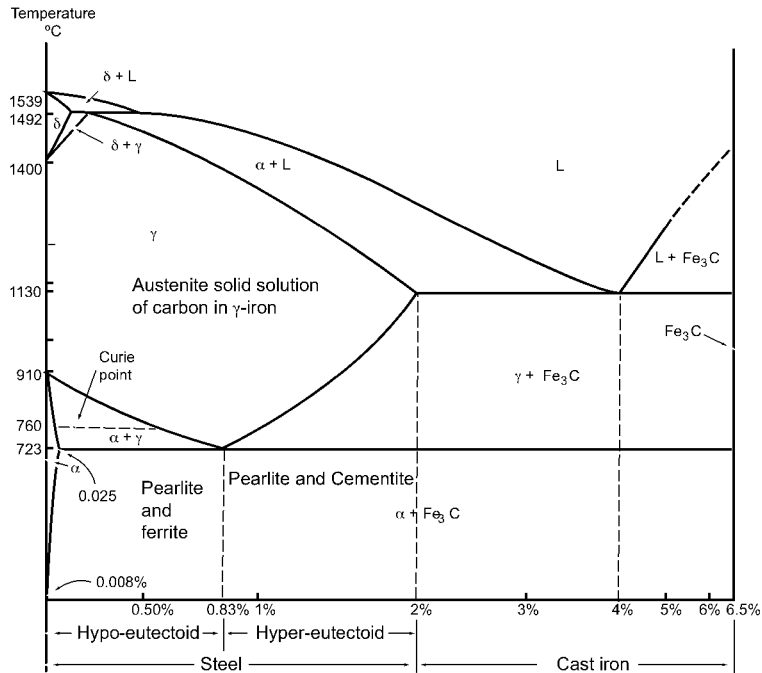


FIGURE 1.2. Iron - iron carbide phase diagram. Carbon content is expressed in wt.% on a logarithmic scale.

What is meant by sufficiently rapid cooling depends strongly on the chemical composition. For each particular steel, a characteristic time-temperature-transition or TTT diagram can be obtained. An example of a TTT diagram for a high carbon steel is given in fig. 1.3. The rate of cooling must be high enough to reach the martensitic start temperature M_s , suppressing the higher temperature diffusion-controlled pearlite formation reactions (region marked P in fig. 1.3), or intermediate reactions (region marked B in fig. 1.3) such as the formation of bainite. Both pearlite and bainite are mixtures of ferrite and cementite, but pearlite has a typical eutectic lamellar structure, while bainite is a fine aggregate of ferrite and cementite.

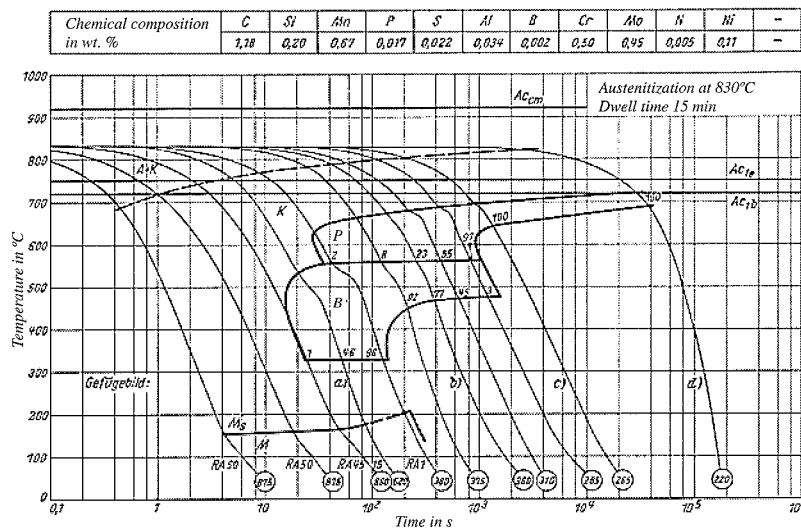


FIGURE 1.3. Temperature-time-transformation (TTT) diagram for a steel with a given chemical composition. Cooling curves for different cooling rates are plotted accompanied by the value of the Vicker's hardness of the microstructure obtained. For a pure martensitic transformation, the cooling has to be fast enough so that the temperature of the start of the martensitic transformation, M_s , is reached without passing through the regions marked P (pearlite formation) or B (formation of bainite) [Rose 1972].

The correspondence between austenite and ferrite lattices was first described by Bain. As shown in the figure 1.4, octahedral interstitial sites in fcc would be converted to c-oriented octahedral sites in bcc. However, to convert this cell to a martensite cell, a contraction of about 17% of the c-axis and an expansion of about 12% of the a-axis is necessary (Bain strain). Such a deformation would require a considerable amount of energy to overcome the potential barrier for the development of a martensite nucleus in the surrounding austenite. On the contrary, experiments show that the martensitic transformation occurs practically without thermal activation and that it propagates at the a speed close to the speed of sound. The minimization of the strain energy requires an invariant plane separating the parent and the product phase (undistorted and unrotated habit plane) and such interfaces are observed experimentally. This means that the transformation strains must constitute an invariant plane strain (S). The existence of a habit plane can be achieved by the combination of Bain's homogeneous shape deformation (B) with an inhomogeneous lattice invariant deformation, as for example shear (P). All that is then necessary is to rotate the strained region by a rotation R in order to make the habit plane both undistorted and unrotated. So, mathematically, a martensitic transformation can be represented by the multiplication of three transformation matrices:

$$S = RPB. \quad (1.1)$$

In general, the indices of the habit plane are irrational. The required shear could result from dislocation glide (dislocations are found in martensites in high concentrations of 10^{11} to 10^{12} cm^{-2} , which is a value found for heavily cold worked metals) producing slip, or from twinning. Twinning is facilitated at high carbon concentrations. As a consequence, different martensite morphologies can be found depending on the carbon content.

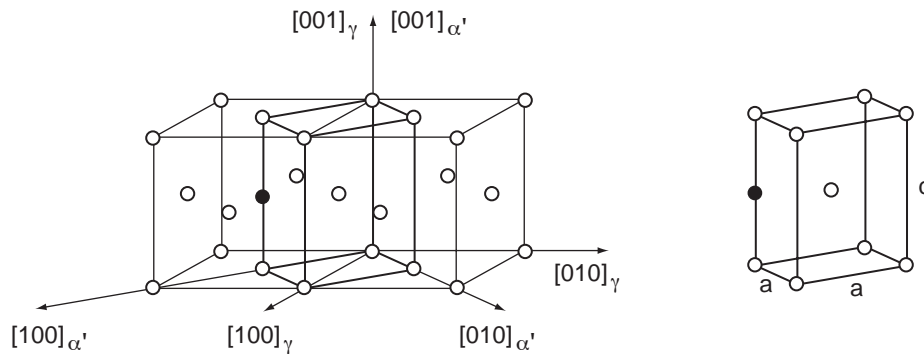


FIGURE 1.4. The lattice correspondence for formation of martensite from austenite as described by Bain. A tetragonal unit cell is outlined in austenite. The interstitial atom (black circle) in an octahedral site in fcc is positioned in the c-oriented octahedral site in bcc. Such tetragonal unit cell has to be compressed along c (about 20%) and expanded along a (about 12%) to be transformed into the martensite unit cell.

The tetragonal distortion of the ferritic bcc matrix due to the martensitic transformation highly depends on the carbon content. This dependence of lattice parameters a and c is described by

$$c = a_0 + 0.116x \quad (1.2)$$

$$a = a_0 - 0.013x \quad (1.3)$$

where a_0 is the lattice parameter of bcc iron (2.8663 Å) and x is the concentration of carbon in weight percent [Kurdjumov 1976, Cheng 1990].

1.3 Martensite morphology

Lath martensite (fig. 1.5a) is normally found in steels with lower concentrations of carbon (up to 0.5 wt.%). The structure units are laths, mostly separated by low angle boundaries, grouped into packets. The substructure is characterized by a very high concentration of dislocations. Plate martensite (fig. 1.5b) is characteristic for high carbon steels (more than 1.3 wt.%). The structure is made of lenticular plates of martensite units, each consisting of fine twins about 5 nm apart. These twins gradually merge into an array of dislocations near the periphery of the plate. The microstructure of steels containing carbon in the range 0.5 to 0.8 wt.% is generally complicated, with lath martensite, plate martensite and residual, non-transformed austenite coexisting together (fig. 1.6a). The effect of carbon content on the volume percent of lath and plate martensite, the temperature of the martensitic transformation and the volume percent of residual austenite are shown in fig. 1.6b [Speich 1972a].

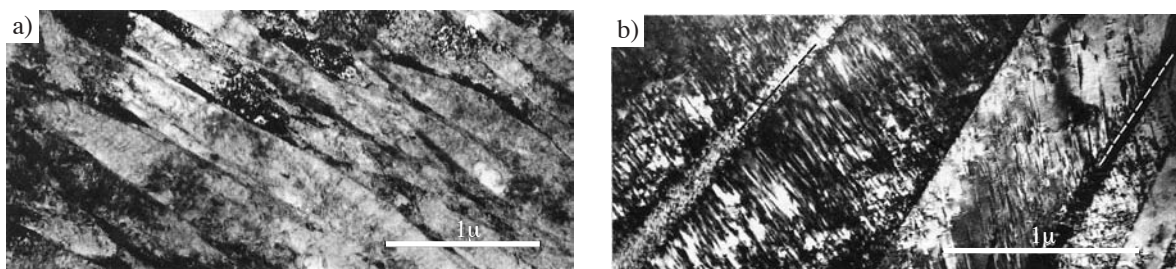


FIGURE 1.5. a) Microstructure of lath martensite in a steel containing 0.2 wt.% carbon. Laths are usually separated by low angle boundaries and grouped into a packet. b) Plate martensite microstructure found in a steel containing 1.4 wt.% carbon, characterized by fine twinning. Taken from [Nishiyama 1978].

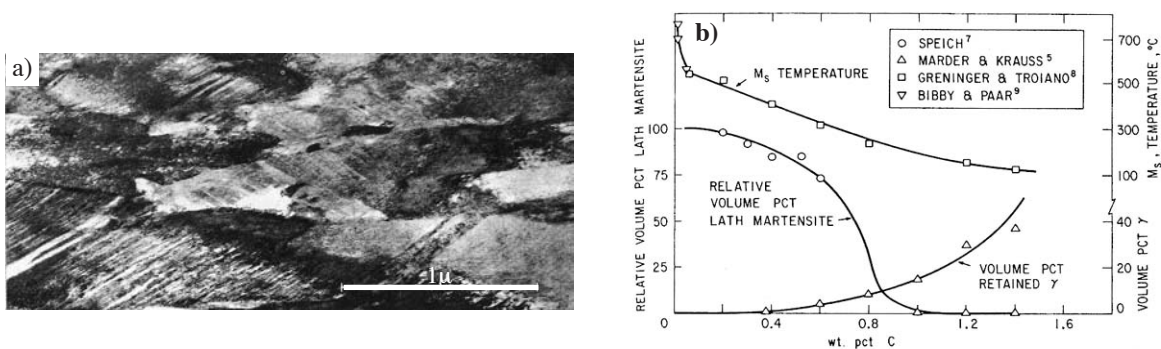


FIGURE 1.6. a) Microstructure of steel containing 0.8 wt.% C. Both lath and plate martensite can be distinguished [Nishiyama 1978]. b) Effect of carbon content on relative volume percent of lath and plate martensite, M_s temperature, and volume percent of retained austenite in Fe-C alloys [Speich 1972a].

1.4 Aging and tempering of martensite

Iron-carbon martensite is a metastable structure, and as such it can undergo structural changes even at low temperature. Historically, the term tempering is used for a process of heating martensitic steels to elevated temperatures so that they become more ductile. The term aging is referring to the processes that occur during the storage of martensite at room temperature.

The aging and tempering behavior of iron-carbon martensite has been the subject of intensive investigation for more than 60 years and a large amount of literature exists covering the subject

[Schmidtman 1965, Speich 1969, Speich 1972a, Inoue 1978, Olson 1983, Samuel 1983, Krauss 1984, Chang 1986, Cheng 1988, Mittemeijer 1991, Cheng 1990, Ohmori 1992, Speich 1992, Van Genderen 1997, Han 2001]. Research has shown that the decomposition processes are complex and involve many overlapping phenomena. The temperature ranges at which they occur are dependent on heating rate, composition and structural details. They can be summarized as follows (for iron carbon martensite containing about 1 wt.% C and for heating rates of the order of 10 to 20 K/min [Mittemeijer 1991]):

- a) Transformation of a part of the retained austenite into martensite between 115 and 215 K
- b) Redistribution of carbon atoms (preprecipitation processes) around and slightly above room temperature, ascribed to:
 - i) Segregation of carbon atoms to lattice defects (~ 0.2 wt.% C).
 - ii) Transfer of carbon atoms at a/b octahedral interstices to c octahedral interstices
 - iii) Formation of carbon enrichments in the matrix for the predominant part of the carbon atoms
- c) First stage of tempering between 355 and 455 K: precipitation of transition carbides
- d) Second stage of tempering between 475 to 625 K: decomposition of retained austenite into ferrite and cementite
- e) Third stage of tempering between 525 and 625 K: precipitation of the stable carbide, cementite
- f) Recovery of dislocation substructure, recrystallization, grain growth and spheroidization of cementite between 600 and 900 K.

Experimental techniques and relevant results from literature

This chapter contains a brief description of file processing and experimental methods used in the course of this work. Significant works from the literature are described in order to illustrate the possibilities of experimental methods to study the mechanical behavior and microstructure of carbon steel martensite.

2.1 Thermomechanical treatment during file processing

The thermomechanical treatment of the material during the file production can be divided into three operations: normalization, shaping, and hardening. The raw material is first normalized by annealing for 15 min at 1150 K and subsequent air-cooling, in order to obtain a ferritic structure with embedded spheroidized carbide particles. Next, the material is machined to obtain the final file form. This shaping is performed in several steps, each involving more or less heavy plastic deformation. The shape of the studied files is approximately rectangular, with the dimensions $19 \times 1.4 \times 0.22 \text{ cm}^3$. The teeth, 0.2 mm high with 0.5 mm step size, are cut on two sides. Finally, the thermal treatment producing the hard martensitic phase and thus giving necessary hardness to the file consists in rapid quenching after about 15 min of austenitization at 1100 K. The austenitization can be performed either traditionally, in the cyanide salt bath (CN) or in the conveyor belt furnace (BF) under protective and slightly nitriding atmosphere.

2.2 Microstructural analysis

2.2.1 Transmission electron microscopy

Transmission electron microscopy (TEM) is used with the aim of visualizing the microstructure of the material. Particular attention is dedicated to the study of the martensite morphology, dislocation structure and the presence of residual austenite.

TEM is such a widely used technique that it needs no special presentation. A point that requires more attention is the sample preparation method. In order to study the microstructure by TEM,

it is necessary to make a sample transparent for electrons (thickness of the order of 100 nm). Two constraints make this preparation particularly difficult in our case: first, the thinning of the surface or of the bottom of the file tooth, and second, the need to maintain the temperature of the sample below 80°C to avoid changes of the microstructure (tempering effects). Accordingly, we have developed a method of sample preparation that satisfies both of the above mentioned criteria. Rectangular elements containing the file teeth are cut into small bars of $3 \times 0.6 \times 0.6 \text{ mm}^3$. One side is then polished to reduce the sample thickness to 0.3 mm as shown in fig. 2.1a. The second side is polished with a tapering angle of 0.7° until the transparency for electrons is reached in the zone of interest (fig. 2.1b). Final thinning is achieved by ion bombardment for 20 to 30 min. under cooling by liquid nitrogen.

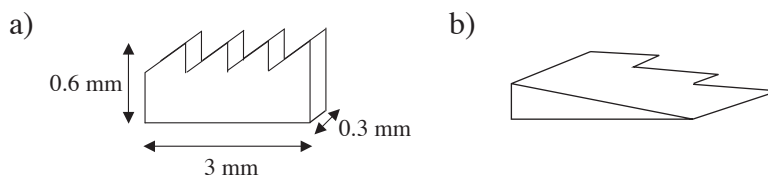


FIGURE 2.1. Scheme of sample preparation for TEM.

It should be mentioned that the method described above worked well for the cyanide treated files. For the files treated in the conveyor belt furnace it was not possible to make the region at the very tip of the file tooth transparent for the electrons. The region of 3-5 μm from the tip seemed to be harder than the core of the tooth and it remained too thick to be transparent after ion bombardment. If the ion bombardment was prolonged, a hole was formed in the tooth core, which grew until the tip was detached. This region is probably a remainder of oxides or hydroxides formed during quenching.

TEM images are obtained using a Philips CM20 microscope with the acceleration voltage of 200 kV.

2.2.2 Atomic force microscopy

Topography images that can be obtained by atomic force microscopy give an interesting insight into the general microstructure of the material using a magnification of the order of 5000 to 10000 \times .

The atomic force microscope (AFM) is based on probing the interaction between a sample and a sharp tip at the end of a cantilever. The interaction, usually Van der Waals force, causes the deflection of the cantilever, which is then detected by means of a laser reflection onto the photodiode (fig. 2.2). In the contact mode, the sample surface is scanned in a rasterizing motion, while the cantilever deflection is kept constant by means of a piezo-scanner elongating or contracting when necessary. The sample topography (more precisely equipotential surface) can then be extracted from the voltage needed for the piezo-scanner movement.

Topography images are obtained using uncoated, sharpened silicon-nitride microlevers and a Park Scientific Instruments M5 commercial AFM. The surface examined is a file cross-section, mechanically polished, using colloidal silica solution of 0.1 μm particle size on a Logitech PM5 polishing machine.

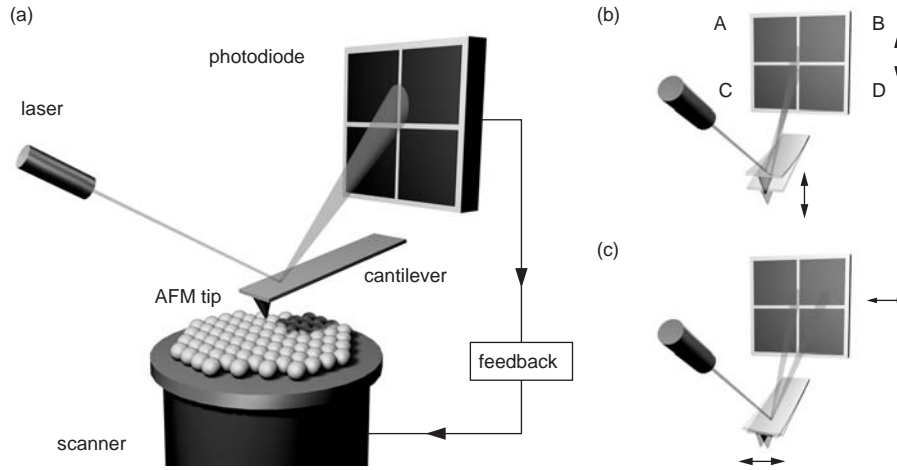


FIGURE 2.2. a) Scheme of the AFM setup based on the laser beam deflection method for detecting normal (b) and lateral (c) deformation of the AFM cantilever (taken from [Kis 2003]).

2.2.3 X-ray diffraction

Principles and experimental procedure

The atomic planes of a crystal cause the waves present in an incident beam of X-rays (if the wavelength is approximately the magnitude of the interatomic distance) to interfere with one another as they leave the crystal. The phenomenon is called X-ray diffraction. Diffraction from crystals is described by the Bragg law:

$$n\lambda = 2d\sin\theta \quad (2.1)$$

where n is an integer (the order of scattering), λ is the wavelength of the radiation, d is the spacing between the scattering entities (e.g. planes of atoms in the crystal) and θ is the angle of scattering.

X-ray diffraction may be used in order to quantify the amount of interstitial carbon in the martensitic matrix, and particularly to verify if a variation exists between the bulk and the teeth of the files. Effectively, in a crystal with tetragonal symmetry, the spacing d between the atomic planes can be calculated from the lattice parameters a and c , and from the Miller's indices of the plane (hkl) according to:

$$d_{hkl} = \frac{ac}{\sqrt{(h^2 + k^2)c^2 + l^2a^2}}. \quad (2.2)$$

As pointed out in the previous chapter, the tetragonalization, i.e. the lattice parameters of the martensitic matrix, depends on the carbon content. The values of a , c , and d -spacings calculated for different carbon concentrations for the three strongest martensite peaks, are given in fig. 2.3 according to eq. 1.2, eq. 1.3 and eq. 2.2.

Therefore, the equivalence of e.g. crystal planes $\{011\}$, $\{101\}$ and $\{110\}$ in the bcc structure, which contribute to one X-ray diffraction peak, determined by the common d -spacing of 2.027 \AA , is not present in the tetragonal martensite. Due to the slight shortening of parameter a and the larger lengthening of the parameter c with the addition of carbon, a slight decrease of the d -spacing is expected for the $\{110\}$ planes, and an increase of the d -spacing for the planes $\{011\}$ and $\{101\}$. The two types of planes will consequently contribute to two diffraction

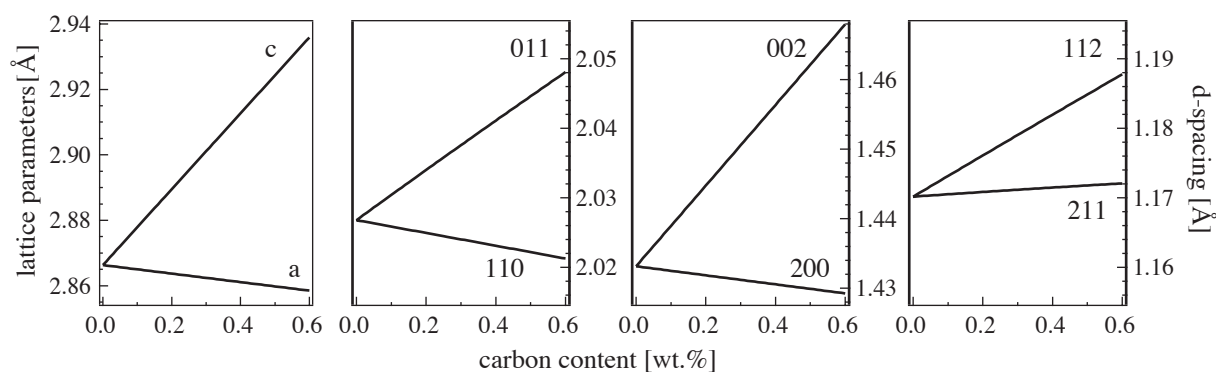


FIGURE 2.3. Lattice parameters a and c of the tetragonal crystal lattice and d -spacings for the three strongest martensite peaks as a function of carbon content.

peaks. The corresponding splitting of the peak depending on the amount of carbon is also existing for other martensite peaks.

The d -spacings can be calculated from the positions of the peaks determined by an appropriate fitting procedure. Comparison of these d -spacings with values calculated for different carbon concentrations allows the assessment of the amount of soluted carbon in the tetragonal martensitic matrix.

The X-ray diffraction experiments were performed at the Swiss-Norwegian Beamline at the ESRF in Grenoble, France. As iron is a strong X-ray absorber, high-energy radiation is required to obtain an adequate penetration depth. At the wavelength of 0.3 Å, a penetration depth of 200 μm can be achieved (50% of the intensity of the incident beam). A high resolution diffractometer with 6 counting chains (each equipped with a Si-111 analyzer crystal and a Na-I scintillation counter) is used to collect the diffraction patterns in a 2θ range from ca. 7 to 20° comprising the three strongest martensite peaks.

Relevant experimental results found in literature

The use of X-ray diffraction as a technique to study lattice parameters of the iron-carbon martensite can be illustrated by works of [Moss 1967, Kurdjumov 1976, Cheng 1991, Van Genderen 1993, Van Genderen 1997]. Figure 2.4 shows an X-ray diffraction pattern of an iron-carbon martensite containing 1.15 wt.% C after different aging times [Cheng 1991]. The splitting of the $\{200\}/\{002\}$ and $\{211\}/\{112\}$ peaks due to the tetragonality is clearly evidenced.

The distribution of carbon atoms in the martensitic matrix varies with time during aging at room temperature due to the pre-precipitation processes (namely transfer of carbon atoms at a/b octahedral interstices to c octahedral interstices, formation of carbon enriched and carbon depleted regions). This has a strong influence on the peak intensities.

A carbon atom causes static displacements [Moss 1967] of the two directly adjacent iron atoms along the c axis (the effects on the a axis are much smaller). This attenuates the intensity of the $\{002\}$ and $\{112\}$ peaks. Hence, an intensity ratio $I\{002\}/I\{200\}$ and $I\{112\}/I\{211\}$ smaller than 1/2 (assumed from peak multiplicity) is found even shortly after quenching. The formation of local carbon enrichments with aging leads to the increase of the mean square displacement of the iron atoms in the c direction (while the mean displacement remains constant), leading to a further decrease of the intensity ratio (dashed line fig. 2.4).

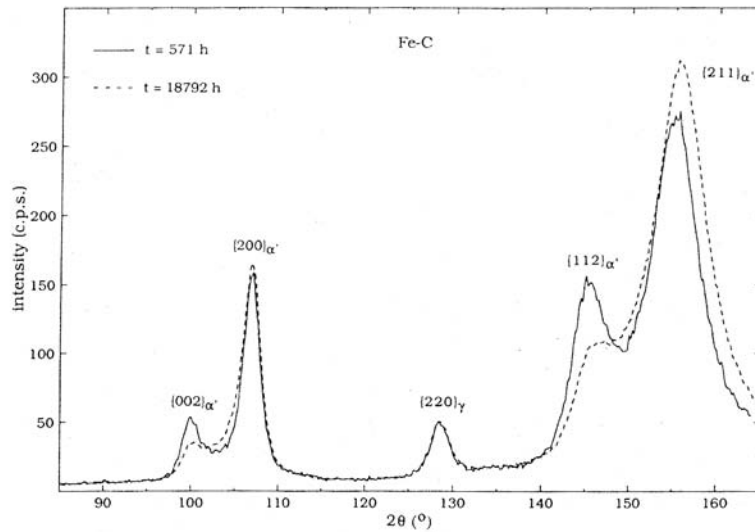


FIGURE 2.4. X-ray diffraction patterns ($Cr K_{\alpha}$ radiation) of an iron-carbon martensitic specimen (5.3C per 100Fe; i.e. 1.15 wt.% C) after 571 h and after 18792 h of aging at room temperature [Cheng 1991].

When martensite peaks are not as clearly separated, which is the case for our material, the information about the intensity ratio is very important to have a reliable fit of the peak positions. Fitting simultaneously several martensite double peaks may increase the fit precision when the intensity ratio cannot be precisely determined.

2.3 Thermoelectric power

2.3.1 Principles and experimental procedure

The thermoelectric power (TEP), also known as Seebeck coefficient (S) or simply thermopower, is a measure of the Seebeck effect. This effect consists in the appearance of an open-circuit voltage, ΔV , when a temperature difference, ΔT , is applied along a sample. The thermoelectric power is then defined by

$$S = \lim_{\Delta T \rightarrow 0} \left(\frac{\Delta V}{\Delta T} \right). \quad (2.3)$$

Physically, the phenomenon arises because charge carriers at higher temperature regions of the sample diffuse into suitably available states of lower energy at lower temperature regions of the sample. The accumulation of charge carriers at the cold side will set up an electric potential difference or electric field along the material. This electric field builds up until a state of dynamic equilibrium is established between the charge carriers that diffuse down the temperature gradient and those that are forced upstream the temperature gradient by the electrostatic repulsion due to excess charge at the cold end [Barnard 1972].

Thermoelectric studies have significantly advanced our understanding of metals, especially of their electronic structures and scattering processes. The thermoelectric power involves the first power of the electronic charge, so this coefficient provides information about the sign of particles, i.e. electrons or holes, and their different mobilities. Another important advantage of the

measurements of TEP over measurements of electric resistivity is that they are independent of the sample geometry.

The thermoelectric phenomena in metals are related to fundamental features of electronic energy levels and to interactions of conduction electrons with their environment. A metal, even an ideal pure single crystal, is a complex many-body system. The theory of transport properties is even more complicated for transition metals, which have overlapping s- and d-bands at the Fermi surface, responsible for many interesting properties: the TEP of transition metals is roughly an order of magnitude greater than that of “simple” metals. Additionally, magnetic effects have to be taken into account when the TEP of iron is considered. A detailed description of thermoelectric phenomena in metals can be found, for example, in [MacDonald 1962, Barnard 1972] or [Blatt 1976]. Some basic notions of different contributions to the TEP in metals are described below.

The contribution to thermoelectric power due to electron diffusion, S_d , can be described by the Mott expression:

$$S_d = -\frac{\pi^2 k^2 T}{3|e|} \left(\frac{\partial \ln \sigma(E)}{\partial E} \right)_{E=E_F}, \quad (2.4)$$

where $\sigma(E)$ is the electric conductivity in the metal for electrons of energy E , k is the Boltzmann constant and e the electron charge. The derivative has to be evaluated at the Fermi energy E_F . This contribution to the TEP is associated with a system of electrons that interacts with a random distribution of scattering centers in thermal equilibrium at the local temperature T .

In a real system, the effect of temperature gradient on the lattice has to be considered as well as the effect of the gradient on electrons. The temperature gradient causes an energy flow from the hotter to the colder region of the material in the form of phonons. The streaming phonons can interact with electrons, producing a contribution to thermopower, especially important at low temperatures. This phenomenon is called the phonon-drag and the contribution to TEP, S_g , can be approximately described by:

$$S_g = \frac{C_g}{3Ne} \alpha, \quad (2.5)$$

where C_g is the specific heat of the lattice (subscript g is coming from the German word “Gitter” for lattice), N is the density of conduction electrons and α , which lies between 0 and 1, is a measure of the probability of a phonon colliding with an electron.

The effect analog to phonon-drag, when lattice vibration waves, phonons, are replaced by spin waves, magnons, can appear in ferroelectric metals. It is described with an expression analog to eq. 2.5, only in the expression for S_m , C_g has to be replaced by C_m , the magnon specific heat.

Thermopower measurements were performed on an apparatus made at INSA, Lyon [Borrelly 1985], schematized in fig. 2.5. The ends of the sample are fixed by teflon screws to two copper blocks marked A and B , the temperatures of which are kept constant by the regulatory system. The distance between the blocks can be regulated so that the length l ranges between 4 and 11 cm. The block A is maintained at temperature T using a cooling Peltier module M , while the block B is held at temperature $T+\Delta T$ by means of a heating resistor R . Both blocks are connected with copper wires W to the isothermal switch I . This way the sample forms a differential thermocouple with copper as a reference material and the ratio of the electrical potential difference ΔV developed because of the temperature difference ΔT gives the relative thermopower ΔS :

$$\Delta S = S_{sample} - S_{Cu} = \frac{\Delta V}{\Delta T}. \quad (2.6)$$

The expression 2.6 is valid under two conditions. First, that ΔT is sufficiently small, so that $S(T)$ between T and $T+\Delta T$ can be considered as linear, and second, that the heat flux through the sample can be considered as negligible. The temperature difference ΔT is measured by a differential thermocouple placed just under the contact points of the sample. The ratio between the amplified values of ΔV and ΔT is obtained using a voltage divider, and the value acquired is displayed (fig. 2.6).

The temperature T is set to 15.0 ± 0.1 °C and ΔT to 10.0 ± 0.1 °C. The absolute thermopower of copper at 20 °C, S_{Cu} , is 1.80 ± 0.01 $\mu\text{V/K}$ [Blatt 1976], and this value should be added to the measured one to get the absolute thermopower of the sample. As the nominal precision of the measured value, 0.3%, with the resolution 0.002 $\mu\text{V/K}$, is better than the precision of the absolute thermopower of copper, it is the relative thermopower that is presented in the following chapters.

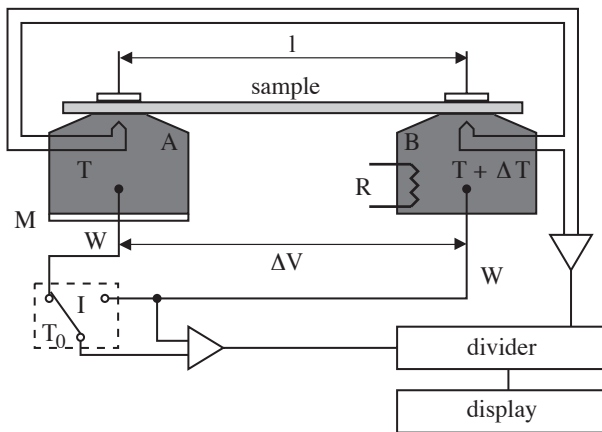


FIGURE 2.5. Schematic representation of the installation for TEP measurements.

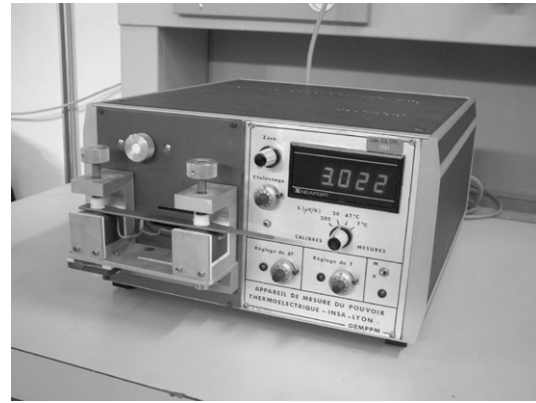


FIGURE 2.6. Installation for TEP measurements.

2.3.2 Relevant experimental results found in literature

Thermopower measurements are found to be a very sensitive probe for the material microstructure. The applications are broad, from verifying the purity of metals (detecting elements in solid solution), through the study of martensitic and order-disorder transformations, precipitation processes, to plastic deformation effects (work hardening) [Borrelly 1979].

The TEP of iron exhibits a very large peak near 200 K (fig. 2.7), the effect of which is still very strong at room temperature. Blatt et al. [Blatt 1967] suggested that the peak arises out of magnon drag because phonon-drag peaks at temperatures as high as 200 K are unusual and because cold working produced a barely perceptible difference in the thermopower-temperature relation. However, other mechanisms, like spin-orbit scattering, electron-electron scattering or even phonon drag are not completely excluded [Blatt 1976].

The effects of cold work as well as those of nitrogen and carbon on the TEP of iron were studied by [Borrelly 1985] and [Benkirat 1988]. Both dislocations and interstitials are found to decrease the TEP measured at room temperature. The decrease of TEP with cold rolling is found to be a linear function of the thickness reduction (fig. 2.8, TEP is measured relative to a reference material with $S_{ref} = 13.2$ $\mu\text{V/K}$). The sensitivity of TEP to the concentration of car-

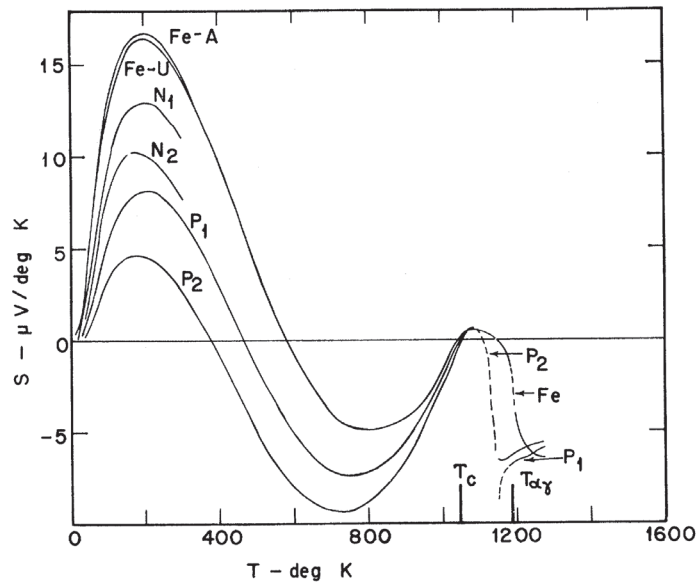


FIGURE 2.7. Thermopower of iron and iron alloys: Fe-A, annealed iron; Fe-U, unannealed iron; N_1 , Fe-0.6 at.% Ni alloy; N_2 , Fe-1.45 at.% Ni; P_1 , Fe-1 at.% Pt; P_2 , Fe-2 at.% Pt [Blatt 1967].

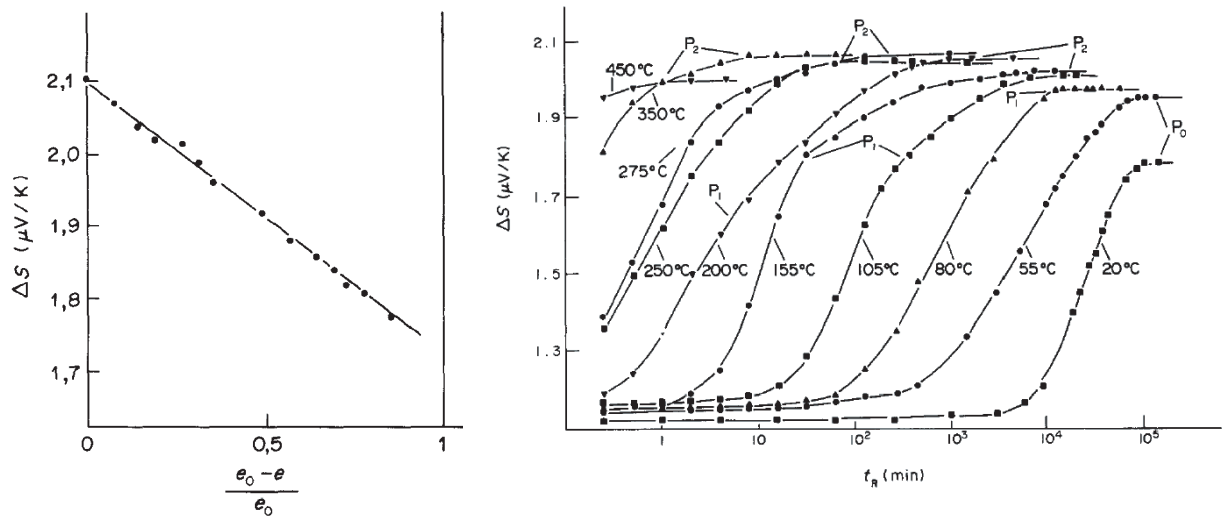


FIGURE 2.8. TEP of pure iron at 20 °C as a function of the relative variation of thickness during cold rolling [Borrelly 1985].

FIGURE 2.9. Evolution of room temperature TEP as a function of aging time at various temperatures for a quenched Fe-0.018 wt.% C alloy. Stabilization levels P_0 , P_1 , and P_2 are related to the residual equilibrium concentration of carbon in the presence of carbides [Benkirat 1988].

bon is used to study the kinetics for isothermal tempering (fig. 2.9, TEP is measured relative to a reference material with $S_{\text{ref}} = 13.2 \mu\text{V/K}$). TEP stabilization levels P_0 , P_1 , and P_2 are related to the residual equilibrium concentration of carbon in the presence of different carbides. No effect on the TEP is attributed to carbides. A linear dependence of thermoelectric power on carbon concentration is proposed for extra-mild steels based on a comparison of TEP with measurements of the Snoek peak in internal friction (the height of which is proportional to the carbon concentration, see section 2.5) [Borrelly 1993]. This proportionality enables a quantitative evaluation of the interstitial content. The method proposed by [Borrelly 1993] includes the

measurement of the TEP before and after precipitation of carbon in the region between 100 and 250 °C. An alternative, rather sophisticated method is proposed by [Lavaire 2004]. It is based on the segregation of carbon to dislocations created by cold rolling. In fact, it was established that the effect of interstitial atoms in solid solution disappears when these atoms are segregated to dislocations.

2.4 Mechanical tests

The aim of this thesis is to relate the mechanical properties with the microstructure issued by a particular heat treatment. Two methods are chosen for measuring mechanical properties: compression tests and nanoindentation. The compression test is a relatively simple and fast way of probing material strength and elastic limits. The advantage of using nanoindentation is the possibility of testing mechanical properties not only for the bulk material, but also for the different regions of the file profile.

2.4.1 Compression

Compression tests were performed at room temperature in a Schenk RMC 100 testing machine, operating in inverse compression (see fig. 2.10) and supporting loads up to 25 kN at room temperature. The TZM pistons are separated from the sample by two WC-Co plates insuring a protection of the piston surface from a possible formation of indents. The applied force is measured by a load cell connected with the movable piston. The displacement is measured by two extensometers.

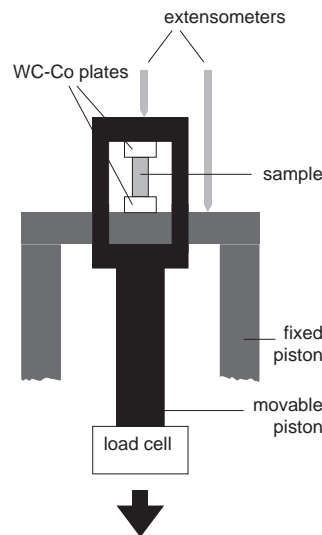


FIGURE 2.10. Scheme of the installation for compression tests. The sample is compressed between two TZM pistons whose positions are detected by extensometers. WC-Co plates protect the piston surface from formation of indents.

The stress σ exerted on the sample is calculated from the applied force F taking into account the changes of the sample cross-section (under constant volume approximation) according to:

$$\sigma = \frac{F}{S_0} \cdot \frac{l}{l_0} \quad (2.7)$$

where S_0 and l_0 are initial sample cross-section and length, respectively, and l its length under load. The strain is calculated from the measured variation of the sample length as following:

$$\varepsilon = \ln\left(1 + \frac{\Delta l}{l}\right) \quad (2.8)$$

Because WC-Co plates and TZM pistons also deform elastically during compression (however little) the slope of the elastic part of the compression curve gives the apparent Young's modulus E_{app} , which is lower than the real Young's modulus of the sample E . Supposing that a part of the installation deforms in series with the sample, the apparent modulus is given by:

$$\frac{1}{E_{app}} = \frac{1}{E} + \frac{1}{E_m} \quad (2.9)$$

where E_m is an installation contribution depending on the sample size.

The stress-strain curves give also some information about the yield stress and the compression strength. The yield stress is defined in connection with the plastic strain and is established by an offset method. It is common to define as engineering yield stress the stress that would cause a permanent deformation of 0.2%. The ideal elastic stress relaxation line is drawn parallel to the elastic portion of the stress-strain curve upon loading, but offset from it by 0.2%. The stress read at the intersection of this line with the stress-strain curve is the yield stress. This procedure does not take into account anelastic effects. The compression strength (also called the ultimate strength) is defined as the maximum stress a material is capable to attain.

Samples for compression tests are spark-cut from the bulk of the file to the dimensions $4.5 \times 1.8 \times 1.9 \text{ mm}^3$ taking special care to make the compressed surfaces parallel. Experiments are performed at constant piston speed, set to $40 \text{ }\mu\text{m}/\text{min}$, giving a starting strain rate of 0.0146 s^{-1} .

2.4.2 Nanoindentation

Hardness is generally defined as the resistance of a material to plastic deformation, usually by indentation, although the term may also refer to resistance to scratching, abrasion or cutting. It is clear that, lacking a more precise definition, hardness can be expressed quantitatively only within a defined measurement procedure. Several relatively simple hardness test methods applying different indent geometries are widely used in industry (Rockwell, Brinell, Vickers hardness etc.). A big advance in hardness measurement came with the development of instruments that continuously measure force and displacement as an indentation is made. Moreover, it is possible to test the mechanical properties at submicron scale. The analysis of the load-displacement data is made according to the method proposed by Oliver and Pharr [Oliver 1992].

For each indentation test, the indenter penetrates the material with a given rate until reaching the defined peak load P_{max} or penetration depth h_{max} (fig. 2.11a). The peak load is maintained constant during a short time, then the indenter is withdrawn. Figure 2.11b shows a cross-section of an indentation and the parameters used in the analysis. Oliver and Pharr proposed a power law to describe the unloading curve:

$$P = a(h - h_f)^m \quad (2.10)$$

where a and m are phenomenological parameters, and h_f is the residual impression depth after unloading, all determined by a least squares fitting procedure. The initial unloading slope S

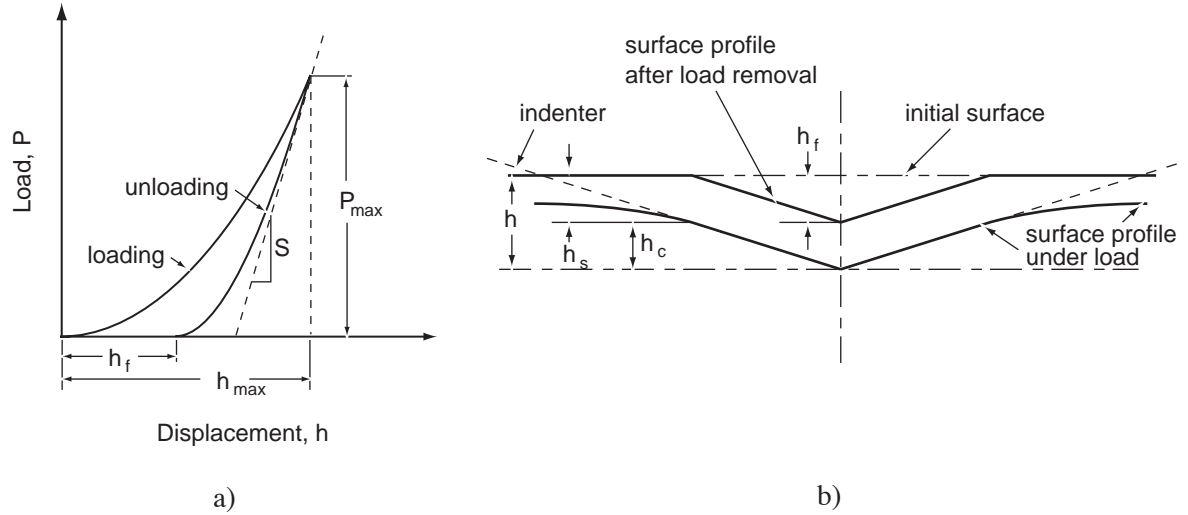


FIGURE 2.11. a) A schematic representation of load versus indenter displacement for an indentation experiment. The quantities shown are the maximal indentation load P_{max} and the indenter displacement h_{max} , the final depth of the contact impression after unloading h_f and the initial unloading stiffness S . b) A schematic representation of elasto-plastic deformation induced by the indenter. At any time during loading, the total displacement h is a sum of h_s , the displacement of the surface at the perimeter of the contact, and the distance along which the contact is made (the contact depth), h_c .

(contact stiffness) is then found by analytically differentiating this expression and evaluating the derivative at the peak load and displacement:

$$S = \left. \frac{dP}{dh} \right|_{h=h_{max}} = ma(h_{max} - h_f)^{m-1}. \quad (2.11)$$

The vertical distance along which the contact is made (the contact depth) h_c can then be calculated according to:

$$h_c = h_{max} - \kappa \frac{P_{max}}{S} \quad (2.12)$$

where κ is a constant depending on the indenter geometry.

The mechanical properties of the sample that can be obtained from one complete cycle of loading and unloading are hardness and elastic modulus. Hardness is defined as:

$$H = \frac{P_{max}}{A} \quad (2.13)$$

where P_{max} is the peak indentation load and A is the projected area of the elastic contact, calculated as $A = f(h_c)$, depending on the indenter geometry. Taking into account the influences of a non-rigid indenter, one can define the reduced elastic modulus E_r through the equation

$$\frac{1}{E_r} = \frac{(1 - \nu^2)}{E} + \frac{(1 - \nu_i^2)}{E_i}, \quad (2.14)$$

where E and ν are Young's modulus and Poisson's ratio for the sample, and E_i and ν_i are the same parameters for the indenter (for diamond the values are $E_i = 1141$ GPa and $\nu_i = 0.07$). The reduced modulus defined above can be obtained from the experimentally measured stiffness S for unloading according to:

$$E_r = \frac{1}{\beta} \cdot \frac{\sqrt{\pi}}{2} \cdot \frac{S}{\sqrt{A}} \quad (2.15)$$

where β is a correction factor arising from the fact that the indenter shape does not have a rotational symmetry.

Nanoindentation experiments were performed on a Nano Indenter XP system with a Berkovich type diamond tip (triangular based pyramid, giving $\kappa = 0,75$ and $\beta = 1.034$), using the continuous stiffness method. This technique superimposes an oscillating load of small amplitude and high frequency to the nominal indenting load allowing continuous measurements of elastic modulus and hardness as the indenter penetrates the material. A more detailed description of the installation and dynamic measurements is given in [Azcoitia 2002] and the original Oliver and Pharr paper [Oliver 1992].

As already pointed out, the aim of the nanoindentation tests was to probe the mechanical properties not only in the bulk, as with compression tests, but more locally. For that reason, a cross-section of the file is obtained perpendicularly to the teeth (on one file side) to allow the measurements on the teeth as well (otherwise not meaningful because of the deformation of the tooth). 5 mm thick samples extracted from the files were mechanically polished as for AFM, using colloidal silica solution of 0.1 μm particle size.

2.5 Mechanical spectroscopy

The concept of anelastic relaxation that has been introduced in 1948 by Zener [Zener 1948], and related topics such as internal friction and mechanical spectroscopy, are described in detail in the classic book by Nowick and Berry [Nowick 1972a] and more recently in the textbook resulting from the summer school “Mechanical spectroscopy Q^{-1} 2001” [Schaller 2001].

2.5.1 Phenomenology and definitions

Under the condition that the stress applied on a material is sufficiently low (lower than the elastic limit), the material will not deform plastically. In that case, the response of the material will be a deformation that can be completely recovered upon release of the applied stress, composed of an elastic and an anelastic part. The elastic deformation, in addition to the complete recoverability, fulfills the requirement of being linearly proportional to the applied stress and being instantaneous. The anelastic part, usually much lower in magnitude, differs from the elastic one merely in the way that the equilibrium response is achieved after sufficient time. The anelastic response is related with the motion of defects in the material and results in a dissipation of energy.

The internal friction (IF), also called the mechanical loss, is a measure of this energy dissipation in the case of an applied cyclic stress. It is defined as:

$$\text{IF} = \frac{1}{2\pi} \frac{\Delta W}{W} \quad (2.16)$$

where ΔW is the energy dissipated and W the energy stored during one cycle. The internal friction is directly related to the number and kind of mobile microstructural units inside the solid, as well as to the characteristic motion that they undergo. Therefore, the measurement of internal friction can be used to obtain information about the microstructure of the material in a non-destructive way. Mechanical spectroscopy is a spectroscopic technique in which a

mechanical oscillating stress of frequency ω interacts with the solid. The response of the solid involves the absorption of mechanical energy that we measure as a function of frequency, giving an internal friction spectrum.

To describe the anelastic behavior (fig. 2.12), it is convenient to use a rheological model. The model for a standard anelastic solid is shown in fig. 2.13. The elastic part of the response, ε_{el} , is controlled by the elastic spring with the compliance J_u . The compliance J can be considered as the inverse of the modulus, $J = 1/E$. The anelastic part, ε_{anel} , is controlled by an elastic spring with the compliance δJ and a dashpot with a viscosity η . The viscosity η is conveniently expressed as $\tau/\delta J$, where τ is the relaxation time.

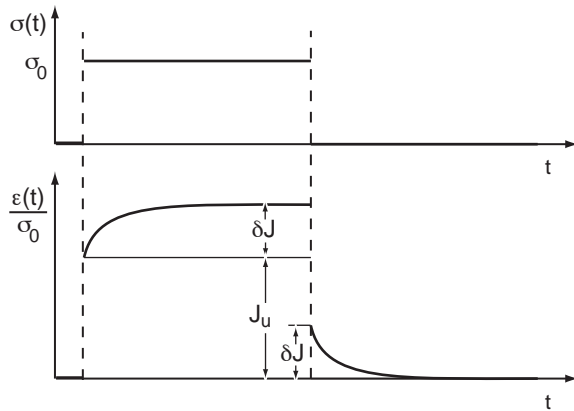


FIGURE 2.12. Stress and normalized strain response for an anelastic solid as a function of time.

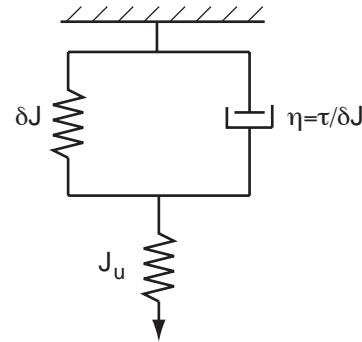


FIGURE 2.13. Three-parameter rheological model of the standard anelastic solid.

Based on the rheological model and starting from the equation:

$$\varepsilon = \varepsilon_{el} + \varepsilon_{anel}, \quad (2.17)$$

a general stress-strain differential equation describing the anelastic behavior can be easily derived:

$$\varepsilon + \tau \dot{\varepsilon} = \sigma(\delta J + J_u) + J_u \tau \dot{\sigma}. \quad (2.18)$$

In the case of an applied cyclic stress, with amplitude σ_0 and frequency ω :

$$\sigma = \sigma_0 e^{i\omega t}, \quad (2.19)$$

assuming a linear stress-strain relationship:

$$\varepsilon = J^* \sigma, \quad (2.20)$$

where $J^* = |J|e^{-i\phi}$ is a complex compliance, generally dependent on ω , the solution of eq. 2.18 can be expressed in form:

$$\varepsilon = \varepsilon_0 e^{i(\omega t - \phi)}, \quad (2.21)$$

where ϕ is the angle by which the strain lags behind the stress, often called the loss angle. It can be shown that the ratio of the dissipated and stored energy during one cycle, defined as internal friction in eq. 2.16, is related to the loss angle by:

$$\text{IF} = \text{tg}\phi. \quad (2.22)$$

Another useful quantity is the relative variation of the dynamic compliance (or correspondingly, the so called modulus defect):

$$\frac{\delta J(\omega)}{J_u} = \frac{\operatorname{Re}(J^*(\omega)) - J_u}{J_u} \quad (2.23)$$

From equations 2.18 - 2.23, and in the case of $\delta J \ll J_u$, it follows that:

$$\operatorname{IF} = \operatorname{tg} \phi = \frac{\delta J}{J_u} \frac{\omega \tau}{1 + \omega^2 \tau^2} = \Delta \frac{\omega \tau}{1 + \omega^2 \tau^2} \quad (2.24)$$

$$\frac{\delta J(\omega)}{J_u} = \Delta \frac{1}{1 + \omega^2 \tau^2}. \quad (2.25)$$

The above mentioned equations 2.24 and 2.25 are referred to as Debye equations. When plotted as a function of $\log \omega \tau$ (fig. 2.14), the IF has the form of a peak symmetrical around $\log \omega \tau = 0$ (the Debye peak), where it reaches the maximum value, $\Delta/2$. The ratio $\Delta = \delta J/J_u$ is often called the relaxation strength.

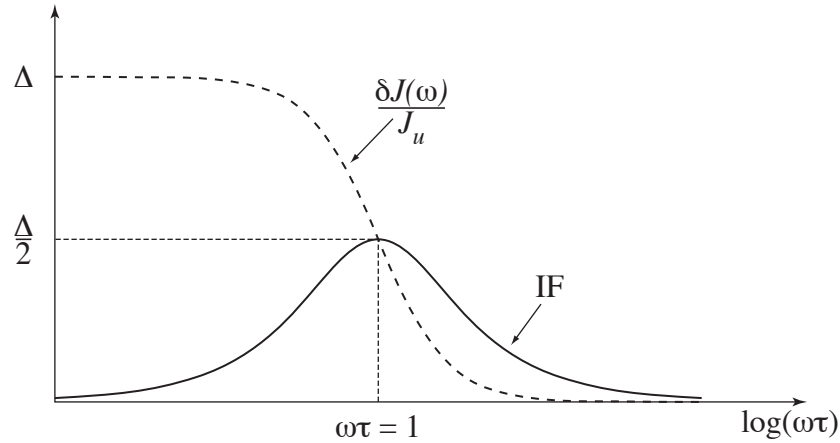


FIGURE 2.14. Internal friction and relative variation of compliance plotted as a function of $\log \omega \tau$. IF has the form of a Debye peak with the maximum situated at $\omega \tau = 1$.

For thermally activated relaxation phenomena, the relaxation time follows the Arrhenius law:

$$\tau = \tau_0 e^{\frac{H}{kT}} \quad (2.26)$$

where H is the activation enthalpy of the process, k is the Boltzmann constant and τ_0 is the limit relaxation time (inverse of the attempt frequency, ν_0). The importance of such a relation is that the quantity τ may be varied over a wide range simply by changing the temperature. Because of this equivalence between frequency and temperature (the condition for the Debye peak is $\omega \tau = 1$), the term “temperature spectrum” is often used when IF is plotted as a function of temperature. It should be noted, introducing eq. 2.26 into eq. 2.25, that when a relaxation peak appears, the dynamic modulus should decrease when increasing the temperature.

If a series of IF peaks is measured as a function of temperature at different frequencies (or vice versa, as a function of frequency at different temperatures), the relaxation parameters H and τ_0 can be calculated using the Arrhenius plot, where the logarithm of the peak frequency is plotted as a function of the inverse of the peak temperature. The slope of the straight line obtained

gives H , and the intercept with the y-axis gives τ_0 . Analogously, knowing one temperature and frequency of the peak together with its activation energy, enables the prediction of the peak temperature for a given frequency (or frequency for a given temperature) according to the expression:

$$\ln \frac{\omega_1}{\omega_2} = \frac{H}{k} \left(\frac{1}{T_2} - \frac{1}{T_1} \right) \quad (2.27)$$

that is easily derived combining eq. 2.26 and the peak condition $\omega\tau = 1$. There are many cases where there is no single relaxation time associated with a physical process. It is often necessary to define a distribution of relaxation times. In that case, the internal friction can be described by the expression:

$$\text{IF} = \Delta \frac{(\omega\tau)^\alpha}{1 + (\omega\tau)^\alpha}, \quad 0 < \alpha \leq 1. \quad (2.28)$$

where α is a broadening factor [Fuoss 1941].

Experimentally, IF can be measured by imposing a forced vibration to the system, and by determining the phase lag ϕ between the applied stress and the responding strain (fig. 2.15). Another method, more suitable for measuring low IF, consists in observing the oscillations in free decay, after inducing the oscillations at the resonant frequency f_0 . In the case of low IF (lower than 0.1 [Zener 1947, Parke 1966]), the oscillations are exponentially damped (fig. 2.16). The internal friction is then directly related (by the factor $1/\pi$) to the dimensionless quantity α called the logarithmic decrement, representing the natural logarithm of the ratio of amplitudes A_n and A_{n+1} of two successive vibrations:

$$\text{IF} = \frac{1}{\pi} \cdot \ln \left(\frac{A_n}{A_{n+1}} \right) \quad (2.29)$$

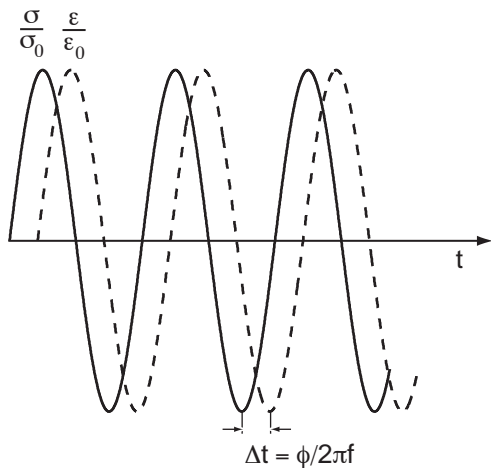


FIGURE 2.15. Normalized stress and strain versus time, in the case of forced oscillations with frequency $f \ll f_0$. The IF can be calculated from the phase lag ϕ .

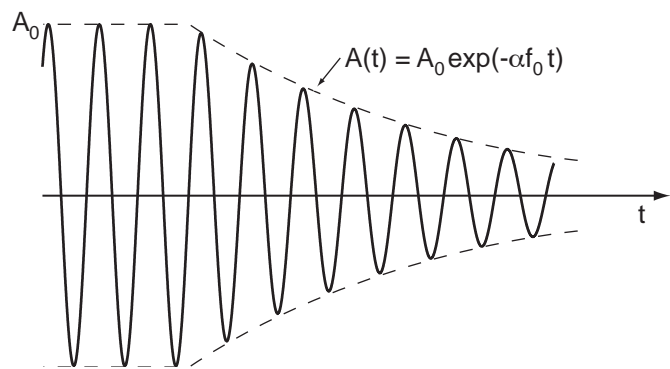


FIGURE 2.16. The free decay of natural vibrations (at resonant frequency) after the removal of the exciting force. The IF can be calculated from the logarithmic decrement α .

2.5.2 Experimental installations

As the relaxation processes in the material depend both on temperature and frequency, the measurements of internal friction are performed on different types of installations. The free-free vibrating reed installation is used to study the IF at high frequencies (1-3 kHz) and the inverted torsion pendulum to study the IF at low frequencies (0.5 - 3 Hz). The temperature range is 80-800 K for high and 90-700 K for the low frequency installation. The standard heating rate used is 1 K/min, if not otherwise mentioned.

Free-free vibrating reed installation

The principle of measuring internal friction in the free-free vibrating reed installation has been described in detail by [Vittoz 1963]. A rectangular sample suspended between two pairs of thin wires, placed at nodal lines of the first flexural vibration mode, is excited to oscillate at its resonant frequency by means of an excitation-detection electrode (fig. 2.17). The electrode, positioned above the center of the sample, forms with it a capacitor.

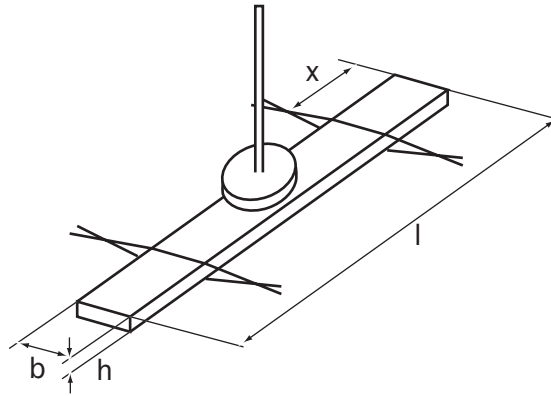


FIGURE 2.17. Scheme of the free-free vibrating reed installation. A rectangular sample suspended between two pairs of wires placed at the nodal lines of the first flexural vibration mode is excited to oscillate at its resonant frequency by means of an electrode.

When a voltage of the form

$$U = U_0 + U_1 \sin(\omega t) \quad (2.30)$$

is applied to the electrode, an electrostatic force F acts on the sample:

$$F = \frac{\epsilon_0 A}{d^2} \left[U_0 U_1 \sin(\omega t) - \frac{1}{4} U_1^2 \cos(2\omega t) + \frac{1}{2} \left(U_0^2 + \frac{1}{2} U_1^2 \right) \right], \quad (2.31)$$

where A is the surface of the electrode, d the interelectrode gap and ϵ_0 the vacuum permittivity. Under the condition that $U_0 > U_1$, the electronics part of the installation filters the frequency of the excitation in order to be the resonant frequency of the sample. A resonant frequency $f = \frac{\omega}{2\pi}$ for the first flexural vibration mode is found to be [Vittoz 1963]:

$$f = \frac{9\pi}{16\sqrt{3}} \frac{h}{l^2} \sqrt{\frac{E}{\rho}} = \frac{9\pi}{16\sqrt{3}} \frac{h^{3/2} b^{1/2}}{l^{3/2}} \sqrt{\frac{E}{m}} \quad (2.32)$$

where h is the thickness, b the width and l the length of the sample, E its Young's modulus and ρ and m its density and mass, respectively. The distance x of the nodal line from the end of the sample is in this case $0.2241l$. The detection of the oscillations is made by including the

sample-electrode capacitor into an RCL circuit oscillating at high frequency (3.6 MHz). The variation of the electric capacitance due to the changing distance between the sample and the electrode causes a frequency modulation of the high frequency carrier signal (radio principle). A servo-motor holds the electrode gap constant so that no variation occurs in the carrier frequency and the vibrating amplitude as a result of the thermal dilatation of the electrode-sample system. A more detailed description of the installation can be found in [Fornerod 1968] and [Isoré 1973].

After stopping the excitation, the number n of oscillations in free decay between two fixed amplitudes A_i and A_{i+n} is recorded. Internal friction is then calculated according to:

$$IF = \frac{1}{n\pi} \cdot \ln\left(\frac{A_i}{A_{i+n}}\right) \quad (2.33)$$

The chosen length of the samples is 40 mm in order to have the nodal points of the first flexural oscillation mode at the distance fixed in the setup, the width of the sample is 4 mm and the thickness is varied between 0.3 and 1 mm. The maximum strain amplitude varies from 10^{-7} to 10^{-6} .

Inverted torsion pendulum

Internal friction at low frequencies is studied in an inverted torsion pendulum. The scheme of the excitation and the detection of torsional vibrations is shown in fig. 2.18 .

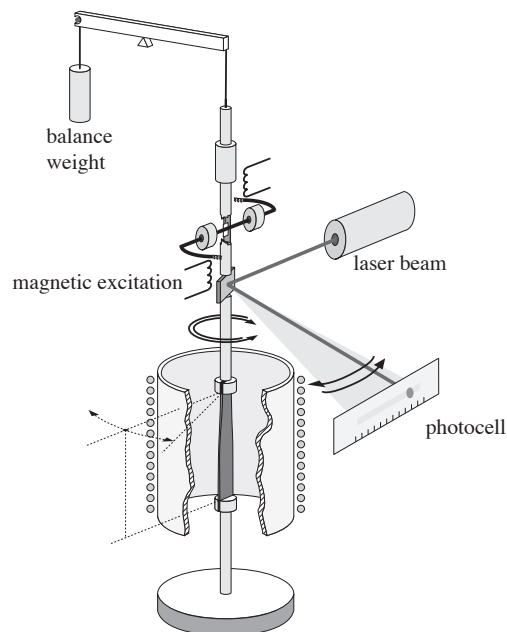


FIGURE 2.18. Scheme of the inverted torsion pendulum. The sample mounted on a rod is excited to oscillate at its resonant frequency by means of two coils and permanent magnets mounted on the rod. The oscillations are detected with the help of a laser pointing on a mirror mounted on the rod; the reflected beam is detected by a photodiode.

The rectangular sample is clamped at each end on a rod. The lower rod is then fastened to the fixed part of the installation and the upper one is suspended with a wire and a counterweight to avoid a compressive force on the sample. Torsional vibrations are induced with the help of two coils and permanent magnets attached on the rod. The oscillations are detected by means of a laser pointing on a mirror on the rod and the reflected beam is then detected by a linear photodiode. A more detailed description of the installation can be found in [Mercier 1974].

Again, as in the case of torsional vibrations, the frequency of oscillations is the resonant frequency, which depends on the sample parameters:

$$f = \frac{1}{2\pi} \sqrt{\frac{\beta G b h^3}{I l}} \quad (2.34)$$

where G is the shear modulus, I the moment of inertia of the rod-sample system, b and h are the previously described sample dimensions, while l is in this case the free length of the sample (between clamps). A numerical coefficient β is necessary to describe the torsional rigidity of a rectangular bar and it is dependent of the b/h ratio [Timoshenko 1963]. Typical sample dimensions (between the clamps) are $10 \times 4 \times 0.3 \text{ mm}^3$, resulting in a value of $\beta = 0.319$. The maximum strain amplitude is 10^{-5} . The internal friction is measured as in the case of the vibrating reed setup, observing the free decay of the oscillations.

Some measurements are also made in a forced inverted torsion pendulum where the sample is forced to oscillate at a chosen frequency well below the resonant one. The scheme of the pendulum is similar to the one presented in fig. 2.18, but the internal friction is measured from the phase lag (fig. 2.15, eq. 2.24) between excitation and the mechanical response of the sample. The advantage of using a forced pendulum is the possibility to vary the oscillation frequency in a broad range on a single sample. The measurements in free decay, on the other hand, give a better possibility to measure very low levels of internal friction.

2.5.3 Relevant experimental results found in literature

Various relaxation mechanisms are found to contribute to the internal friction in bcc metals, involving point defects, dislocations, or both when interacting. They are briefly described in the following paragraphs. In addition to relaxation mechanisms, internal friction is also influenced by phase transformations resulting in features which are not thermally activated. One of these phenomena is the martensitic transformation. The isothermal martensitic transformation has been studied by internal friction in Fe-Ni and Fe-Ni-C alloys [Rodriguez 1984]. As the martensitic transformation in our material only occurs upon quenching, and is completely finished at room temperature, these results are of little relevance for this work. The reverse transformation upon heating is not sudden. The diffusion of carbon and the formation of carbides depletes the martensitic matrix of carbon in solid solution and martensite gradually decomposes into ferrite.

One of the most famous point defect relaxation mechanisms is certainly the one causing the so called Snoek IF peak [Nowick 1972b, Weller 2001]. The term Snoek relaxation refers to the anelastic relaxation in bcc metals produced by interstitial solutes in the process of strain-induced ordering. It was first observed by Snoek [Snoek 1939] in α -iron loaded with nitrogen and carbon, but it is now known that other bcc metals (e.g. Ta, Nb, Cr, V) exhibit a relaxation of the same type with different interstitials (H, O, in addition to C and N). The prerequisite for an anelastic relaxation by point defects is the existence of several defect positions. An interstitial atom occupying the octahedral interstitial position in a bcc crystal lattice (fig. 1.1c) constitutes an elastic dipole of tetragonal symmetry, with the symmetry axis lying along the mayor axis of the octahedron. The tetragonal axis may lie along any of the cube axes. Therefore, in case of equilibrium without external stress, the octahedral sites may be divided into three groups of crystallographically equivalent sites. Under the effect of an applied stress, one orientation is preferred and the interstitials jump between neighboring octahedral sites causing the reorientation of elastic dipoles. This relaxation process results in the formation of an internal friction peak with an amplitude proportional to the concentration of interstitials in

solid solution and an activation energy which is that of diffusion of the interstitial solute. The relaxation parameters for the Snoek peak found in α -iron due to interstitial carbon and nitrogen are given in table 2.1 [Weller 1996].

interstitial type	H [eV]	τ_0^{-1} [10^{14}s^{-1}]	T_m [K] ($f=1\text{Hz}$)
N	0.82±0.01	4.2±2	300
C	0.87±0.01	5.3±2	314

TABLE 2.1 Snoek relaxation parameters for interstitial nitrogen and carbon in α -iron [Weller 1996].

A rigorous theoretical calculation of the relaxation strength in case of a polycrystalline sample is not possible because of the effects of texture and grain size. However, the Snoek relaxation can still be used as an analytical method for measuring the quantity of interstitial solutes if combined with a calibration by other methods (e.g. chemical analysis, electrical resistivity) using specimens with the same grain size and texture. A level of interstitial carbon as low as 1 at. ppm can be detected. On the other hand, if the concentration of interstitials is very high, the Snoek peak can be influenced by interactions between interstitial atoms, leading to a broadening of the peak. Finally, the interaction of interstitials with substitutional impurities generally leads to a decrease of the peak [Saitoh 2004].

The movement of dislocations through a crystal lattice controlled by thermally activated processes can also produce relaxation peaks in internal friction spectra [Benoit 2001]. Pure body centered cubic metals, such as Ta, Nb, W, Mo and Fe, exhibit relaxations associated with internal friction peaks due to kink pair formation and migration. They appear in the following order upon increasing temperature: the α' -peak related to the migration of kinks on screw dislocations [San Juan 1987b], the α -peak related to kink pair formation on non-screw dislocations [Seeger 1976] and the γ -peak related to kink pair formation on screw dislocations [Schultz 1991].

The presence of light interstitial atoms shifts the peaks observed in pure materials to higher temperatures [Seeger 1979], as their movement influences the thermal activation. The interaction of interstitials with kink pairs formed on dislocations is generally called Snoek-Köster (S-K) relaxation [Weller 1983]. Thus, the presence of hydrogen transforms the α -peak occurring in α -iron at 30 K for 1 Hz to S-K(H) observed around 100 K [San Juan 1987a]. Correspondingly, with the addition of carbon, the γ -peak found around room temperature [Astié 1980] is transformed into a S-K peak that appears around 500 K at 1 Hz [Magalas 1981]. Some examples of the mentioned peaks in different bcc materials are shown in fig. 2.19.

The Snoek-Köster relaxation involves the dragging of interstitial solute atoms. More generally, when rather mobile point defects are segregated on dislocation segments of an average length \bar{L} (fig. 2.20), they can be dragged by the dislocation under the effect of an applied stress [Gremaud 2001]. This process gives rise to an internal friction peak with the following value of the relaxation strength Δ :

$$\Delta = \frac{\Lambda b^2 \bar{L}^2}{12\gamma J}, \quad (2.35)$$

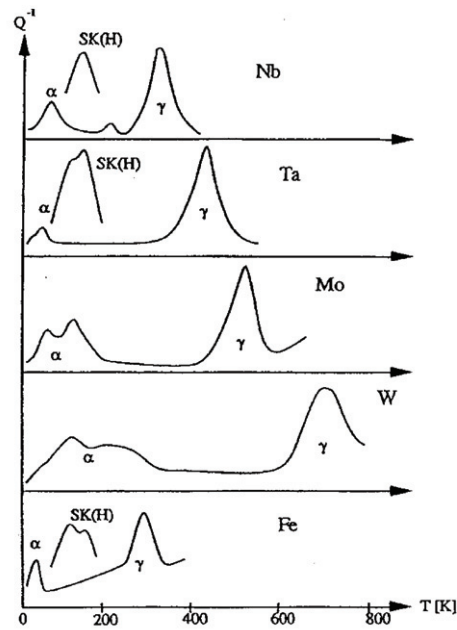


FIGURE 2.19. Relaxation peaks in some bcc materials, after [Schultz 1991].

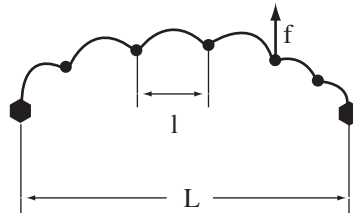


FIGURE 2.20. Schematic illustration of the mechanism of dragging of mobile segregated point defects (circles) by a dislocation segment of length L between strong pinning points (hexagons) under the effect of an applied stress.

and the relaxation time:

$$\tau = \frac{kT\bar{L}^2}{12\gamma\bar{l}D}, \quad (2.36)$$

where Λ is the dislocation density, b is the dislocation Burger's vector, J is the elastic compliance, k is the Boltzmann constant, \bar{l} is the average distance between point defects and D is the diffusion coefficient of the point defects. The dislocation line tension γ can be expressed as $\gamma = \mu b^2/2$, where μ is the shear modulus. The activation energy of the peak is the one regulating the defect diffusion, and it enters eq. 2.36 through the expression:

$$D = D_0 e^{H^S/(kT)} \quad (2.37)$$

The refinement of the theory of the Snoek-Köster peak by considering a kink mechanism as responsible for the dislocation movement leads to a correction of eq. 2.36 considering the peak activation energy [Seeger 1979]. To the activation energy due to the diffusion of point defects, H^S , (also related to the Snoek peak), the energy of the formation of kink pairs, $2H^k$, and possibly even the binding energy between dislocations and point defects, H^B , have to be added. A

detailed description of the thermal activation in the Snoek-Köster relaxation is given for example in [Weller 1983].

The Snoek-Köster peak (named also the cold-work peak) is regularly found in internal friction spectra around 500 K for 1 Hz for cold worked ferrite containing carbon and/or nitrogen and in iron martensites (see for example [Kamber 1961, Petarra 1967, Mura 1961, Klems 1976]).

A recent paper by Bagramov et al. [Bagramov 2001] presents a groundwork study of relaxation phenomena in the martensitic carbon steel that is in the focus of this research. Internal friction spectra are obtained in a temperature range from 80 to 580 K for high frequency (kHz) and from 90 to 700 K for low frequency (Hz) oscillations (fig. 2.21).

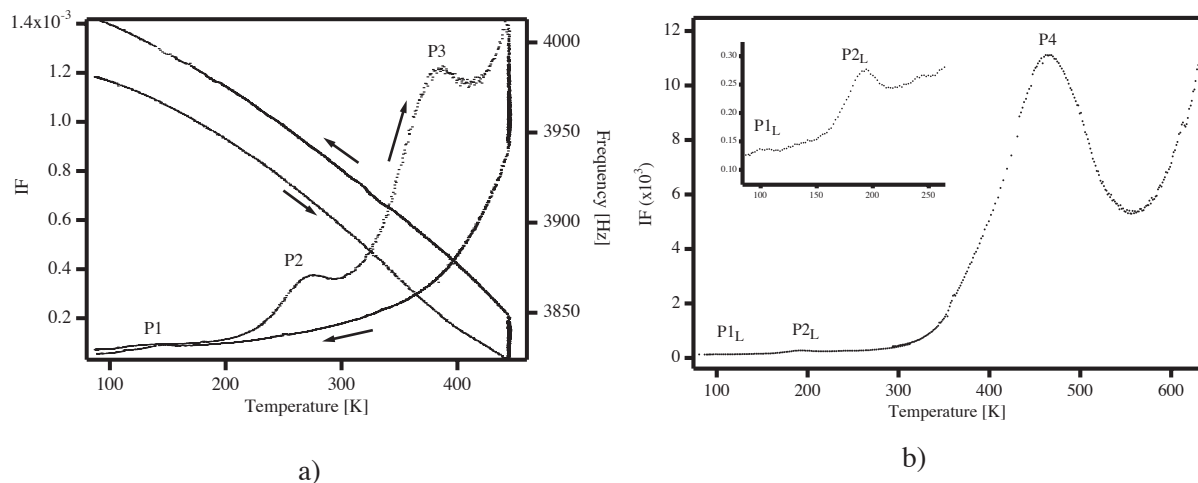


FIGURE 2.21. Characteristic IF spectra of as-received material measured at high (a) and low (b) frequency. After tempering for 40 h the peaks are erased as seen upon cooling [Bagramov 2001].

Three relaxation peaks (P1, P2 and P4) are observed and are all related to the presence of the martensite as they disappear after high temperature tempering. These peaks can be partially restored by room temperature cold work (fig. 2.22). Therefore, they are all related to the presence of dislocations. The relaxation parameters of the peaks obtained from the peak position at low and high frequency are given in table 2.2. The peak P1 is attributed to a relaxation of Snoek-Köster type involving non-screw dislocations and hydrogen atoms. The origin of P2 is not clarified. The peak P4 is identified with the traditional iron S-K (carbon, nitrogen) relaxation. An IF maximum, called P3 is found in high frequency IF spectrum at 370 K (fig. 2.21a). In the low frequency spectrum, it is hidden by the low temperature flank of the peak P4, but otherwise its position does not depend on the frequency. The amplitude of this maximum is found to depend on the heating rate (the higher the heating rate, the higher the amplitude), and it is attributed to a transformation of the material associated with carbon precipitation.

The frequency spectra displayed in fig. 2.23 reveal some important features as the frequency is proportional to the square root of the modulus. A decrease in the modulus slope is observed in coincidence with peak P3 (A); a decrease in the modulus is observed in coincidence with the peak P4 measured in the Hz range (B); a plateau starting around 500 K is noted in both high and low frequency measurements (C). The plateau is shorter in the high frequency measurements as the modulus rapidly decreases because of the presence of P4. In cooling, these features are missing and the modulus is strongly increased.

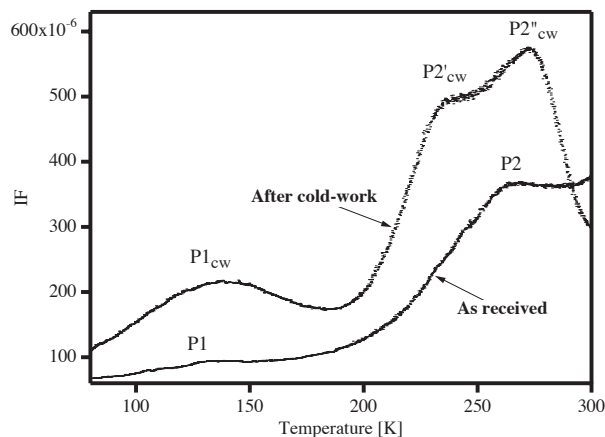


FIGURE 2.22. Comparison of internal friction spectra of martensitic (as received) and 600 K-tempered and room temperature cold-worked material. Peaks P1 and P2, erased by tempering, reappear after cold work with higher amplitude [Bagramov 2001].

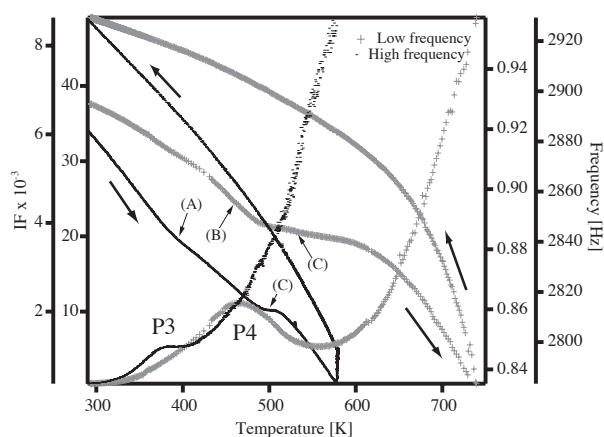


FIGURE 2.23. Comparison of frequency spectra obtained by inverted torsion pendulum (low frequency) and vibrating reed technique (high frequency) [Bagramov 2001].

Peak	Peak position (Low frequency)	Peak position, (High frequency)	Activation energy [eV]	Peak amplitude as-received	Peak amplitude tempered and cold worked
P1	99.1K (1.09Hz)	132.6K (3115Hz)	0.26	1.0×10^{-4}	1.9×10^{-4}
P2	197.9K (0.85Hz)	265.1K (3910Hz)	0.57	2.2×10^{-4}	5.0×10^{-4}
P3	-	373.0K (3855Hz)	-	depends on heating rate	-
P4	470K (0.9Hz)	-	-	1.1×10^{-2}	1.4×10^{-3}

TABLE 2.2 Summary of internal friction results [Bagramov 2001].

2.6 Differential scanning calorimetry

2.6.1 Principles and experimental procedure

Differential scanning calorimetry (DSC) monitors heat effects associated with phase transitions, structural changes and chemical reactions as a function of temperature. In a DSC, the sample and the reference are subjected to identical temperature regimes, i.e. heating at a constant rate. The difference of the amount of electric energy required to maintain the temperatures of the sample and the reference equal is then recorded as a function of temperature. Since the DSC is performed at constant pressure, the heat flow is equivalent to enthalpy changes:

$$\Delta \frac{dH}{dt} = \left(\frac{dH}{dt} \right)_{\text{sample}} - \left(\frac{dH}{dt} \right)_{\text{reference}} \quad (2.38)$$

It is possible to calculate the activation energy for each transformation exhibited in a DSC scan. Several scans have to be made applying different heating rates, and for each heating rate r the temperature T_f , at which a fixed stage of transformation is reached, has to be determined.

Using the following equation:

$$\ln \frac{T_f^2}{r} = \frac{E}{RT_f} + \text{const} \quad (2.39)$$

where R is the gas constant ($8.314 \text{ J mol}^{-1} \text{ K}^{-1}$), when $\ln(T_f^2/r)$ is plotted as a function of $1/T_f$, the slope of the straight line obtained provides a value for the activation energy. In most cases, the temperature of the peak maximum is used as T_f , because the peak maximum approximately corresponds with a fixed degree of transformation [Mittemeijer 1992].

The differential scanning calorimetry measurements are performed on a Mettler Toledo DSC822e calorimeter under N_2 protective atmosphere. Samples (same as in the compression tests, with the dimensions $4.5 \times 1.8 \times 1.9 \text{ mm}^3$ and a mass of the order of 0.11 g) are closed into an aluminium crucible, while an empty crucible is used as reference. The temperature scan rates are varied between 1 K min^{-1} and 10 K min^{-1} .

2.6.2 Relevant experimental results found in literature

An interesting work illustrating how aging and tempering can be evidenced by calorimetry is the study by Van Genderen et al. [Van Genderen 1997]. The aging and tempering behavior of FeNiC and FeC martensite was studied combining DSC and X-ray diffraction. The DSC curve of an iron-carbon martensite containing 4.31 at.% C, aged for about 0.5 h at room temperature, is presented in fig. 2.24. Roman numerals mark different transformation processes summarized in table 2.3

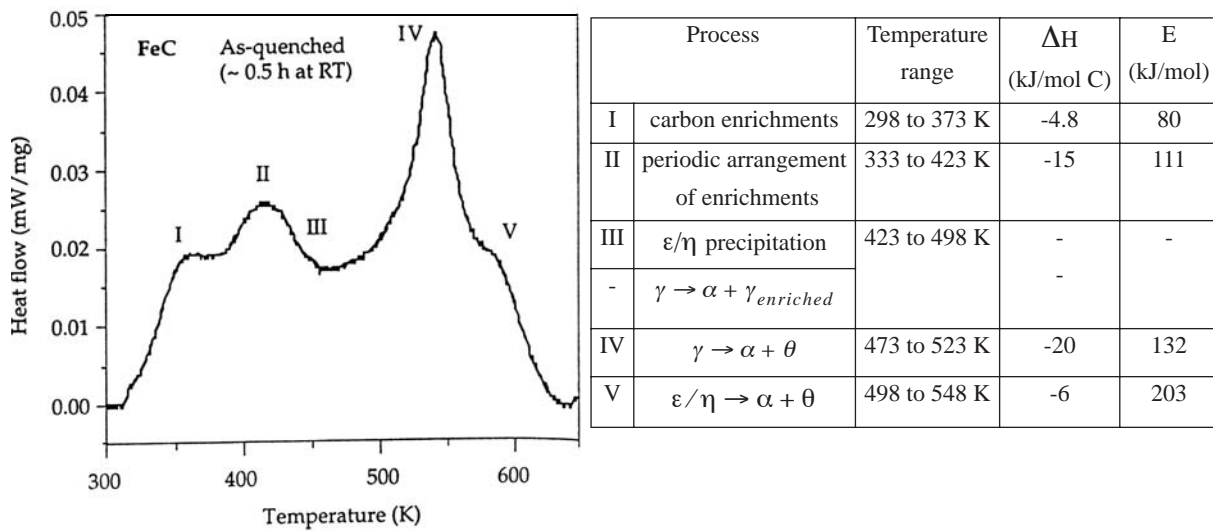


FIGURE 2.24. DSC curve of an as-quenched (i.e., about 0.5 h at RT) Fe-4.31 at.% C martensitic specimen (heating rate = 10 K/min). The stages of transformations are indicated with Roman numerals [Van Genderen 1997].

TABLE 2.3 Identification of the transformations occurring during decomposition of FeC martensite, their transformation enthalpies ΔH and activation energies E [Van Genderen 1997].

Material properties at room temperature

In this chapter, the properties of the material at room temperature are described through the presentation of the results of microstructural analysis, measurements of thermoelectric power and mechanical tests. A primary discussion of the results is given in parallel with their presentation and the conclusions are summarized at the end of the chapter.

3.1 Microstructure

3.1.1 Chemical composition

At first glance, the material under study is relatively simple; its nominal chemical composition is presented in table 3.1. The only elements that can be considered as more than impurities in the iron base are carbon, which is present in a rather high amount when we think of steel, 1.23 wt.%, and chromium: 0,64 wt.%. Scanning electron microscopy / energy-dispersive spectroscopy (EDS) analysis shows that most of the chromium is contained in the cementite [Bagramov 2001]. In the case of addition of chromium, the chemical formula for cementite becomes $(\text{Fe, Cr})_3\text{C}$ instead of Fe_3C . The chromium-to-iron atomic concentration ratio for the carbide particles is determined by EDS to be 0.22 ± 0.03 . The chemical simplicity of the material is deceiving, because its microstructure is highly complex and greatly dependent on thermomechanical history.

Element	Fe	C	Cr	Mn	Si	S	P	Ni	Mo	Cu	Al
Content	balance	1.23	0.64	0.34	0.22	0.006	0.006	0.07	0.02	0.10	0.018

TABLE 3.1 Chemical composition of the base material (wt%).

3.1.2 Atomic force microscopy

Atomic force microscope (AFM) scans of a polished cross-section of a file gives an interesting insight into the general microstructure of the material (fig. 3.1). The bright particles with a size ranging from 0.2 to 2 μm are cementite carbides. Because of their higher hardness, after polishing they remain higher than the surrounding matrix (10 ± 1 nm) which allows their clear dis-

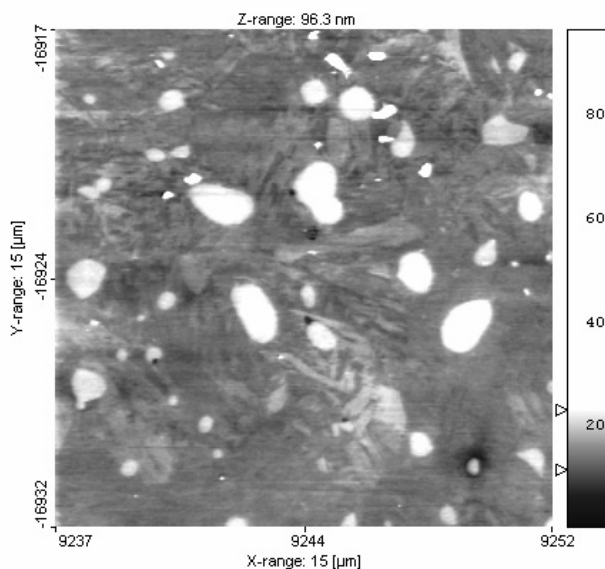


FIGURE 3.1. AFM topography image of the polished surface of the material as found in the files. White particles are $(Fe,Cr)_3C$ carbides embedded in the martensitic matrix occupying 12 ± 2 vol.%.

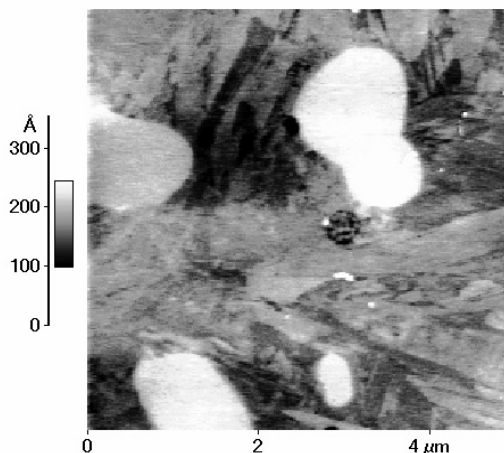


FIGURE 3.2. Some features of the matrix morphology are also discernible in the topography image.

tion. Image analysis of the AFM topography images indicates that carbides occupy 12 ± 2 % of the volume. Some features of the matrix structure are also discernible in the AFM topography images (fig. 3.2). The comparison with TEM images below clearly shows that martensite laths are indeed observed, maybe also some twins. These topological features should come from an unequal resistance to polishing of differently oriented martensite variants.

3.1.3 Transmission electron microscopy

TEM observations of the file material reveal a complex structure. The matrix in which $(Fe,Cr)_3C$ carbides are embedded is typical for steels with an intermediate carbon content [Nishiyama 1978], where both lath and plate martensite are present (fig. 3.3). The martensite is mostly composed of laths without any particular preferred mutual orientation (fig. 3.4) and with a high density of defects (dislocations and stacking faults). The dislocation density is very high, but it is difficult to determine it quantitatively (fig. 3.5 and fig. 3.6).

Plate martensite can be distinguished by its twinned structure (fig. 3.7 and fig. 3.8). However, as the contrast of twins depends on the sample orientation, they are not always visible, and plate martensite can pass unnoticed. A simple calculation can give us a rough estimate of the soluted carbon content. Taking the total amount of carbon in the material to be 1.23 wt.%, the cementite concentration of 12 ± 2 vol.% leaves the matrix with 0.4-0.5 wt.% C (presuming that the unit cell of cementite containing 12 Fe and 4 C atoms occupies 0.1553 nm^3 and taking the total density of the material to be 7660 kg/m^3). The concentration of carbon in solution of 0.4-0.5 wt.% should therefore (fig. 1.6b) lead to the concentration of plate martensite of the order of 20 vol.% [Speich 1972a], which is consistent with the observations.

The presence of the residual austenite was confirmed by indexation of TEM diffraction patterns. It is found between certain laths of martensite and also at the former austenite grain boundaries (fig. 3.9 and fig. 3.10), but the total amount is very small, of the order of 1 vol.%.

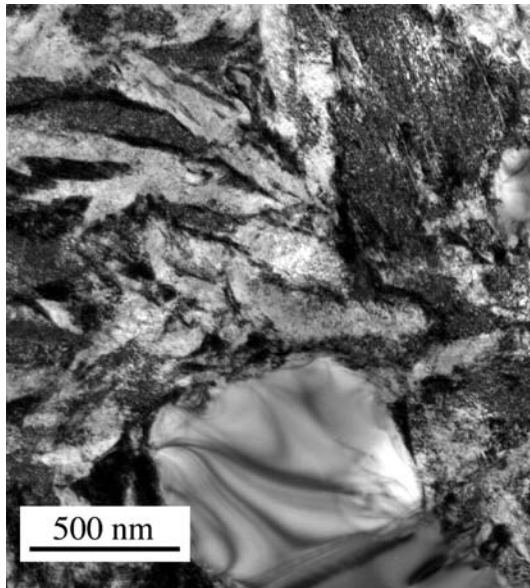


FIGURE 3.3. *Martensitic matrix with an embedded spherical $(Fe, Cr)_3C$ carbide at the bottom of the image.*

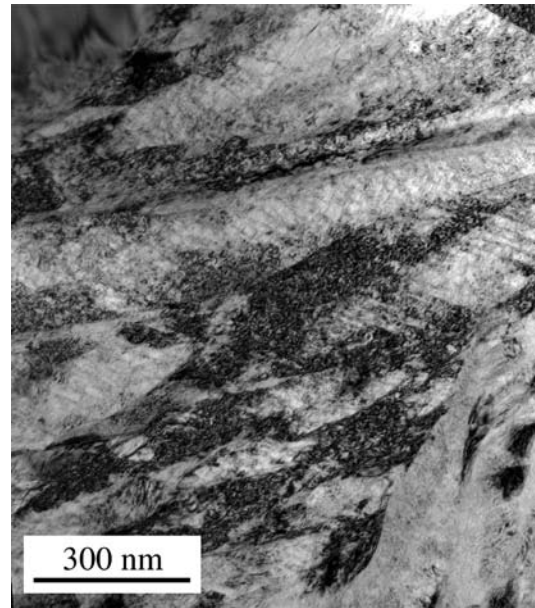


FIGURE 3.4. *Lath martensite with a high concentration of defects (dislocations and stacking faults) producing the dark contrast.*

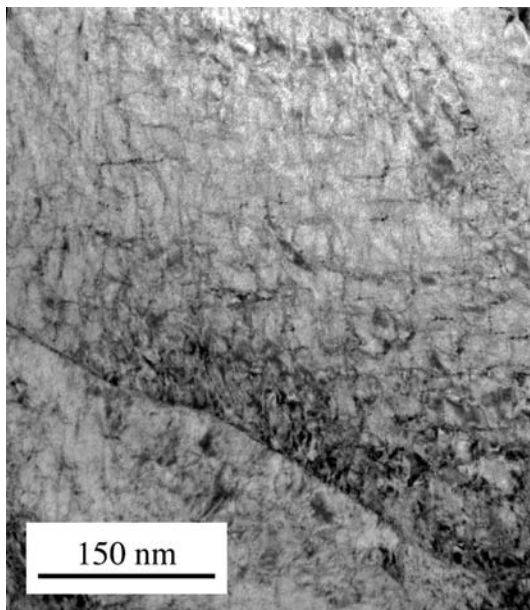


FIGURE 3.5. *Dislocations in lath martensite. Due to their high number, it is difficult to determine their density quantitatively.*

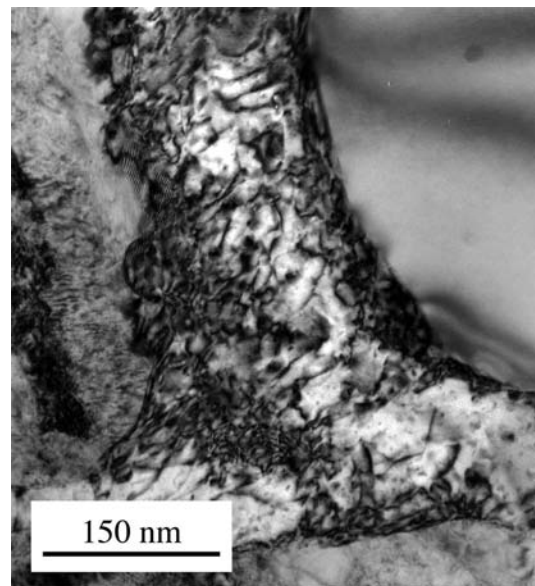


FIGURE 3.6. *Dislocations next to a cementite particle.*

The attempt was made to map the microstructure going from the teeth to the bulk of the file (fig. 3.11 and fig. 3.12 for BF, and fig. 3.13 and fig. 3.14 for CN treated file). However, no clear difference was observed between the microstructures created by the two different thermal treatments. Also, no particular variation of the microstructure depending on the distance from the surface was noticed.

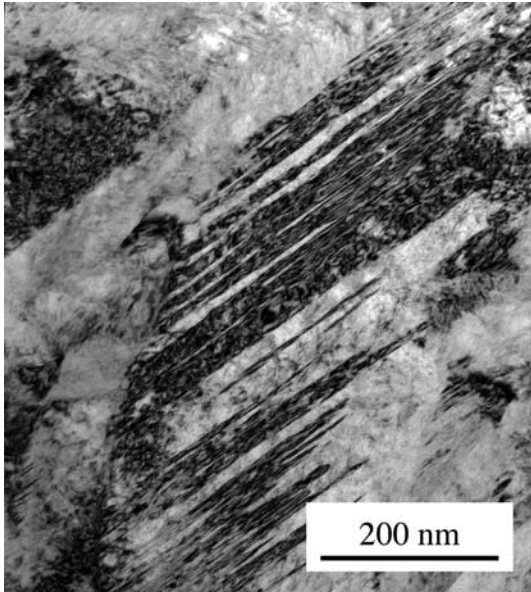


FIGURE 3.7. Plate martensite is characterized by its twinned structure.

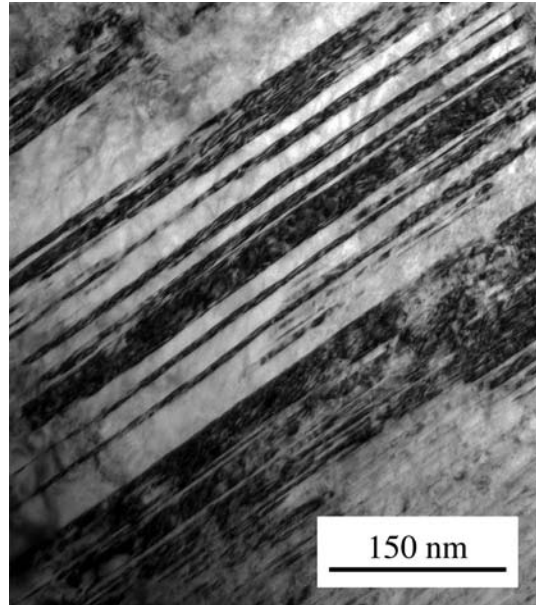


FIGURE 3.8. Twins in plate martensite. The contrast depends on the sample orientation.

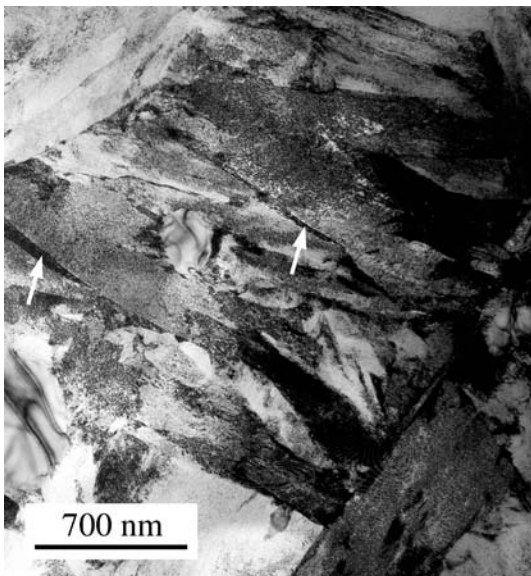


FIGURE 3.9. Residual austenite is present between certain laths and at the former austenite grain boundaries. It appears dark in the images (some examples are marked by arrows).

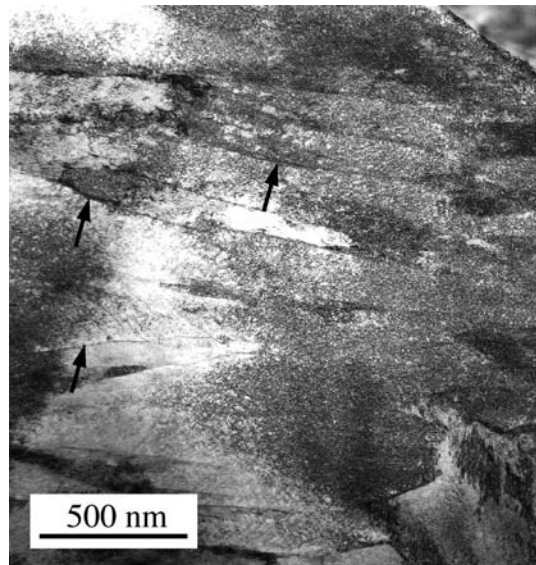


FIGURE 3.10. The quantity of residual austenite (some examples are marked by arrows) is small, of the order of 1 vol.%.

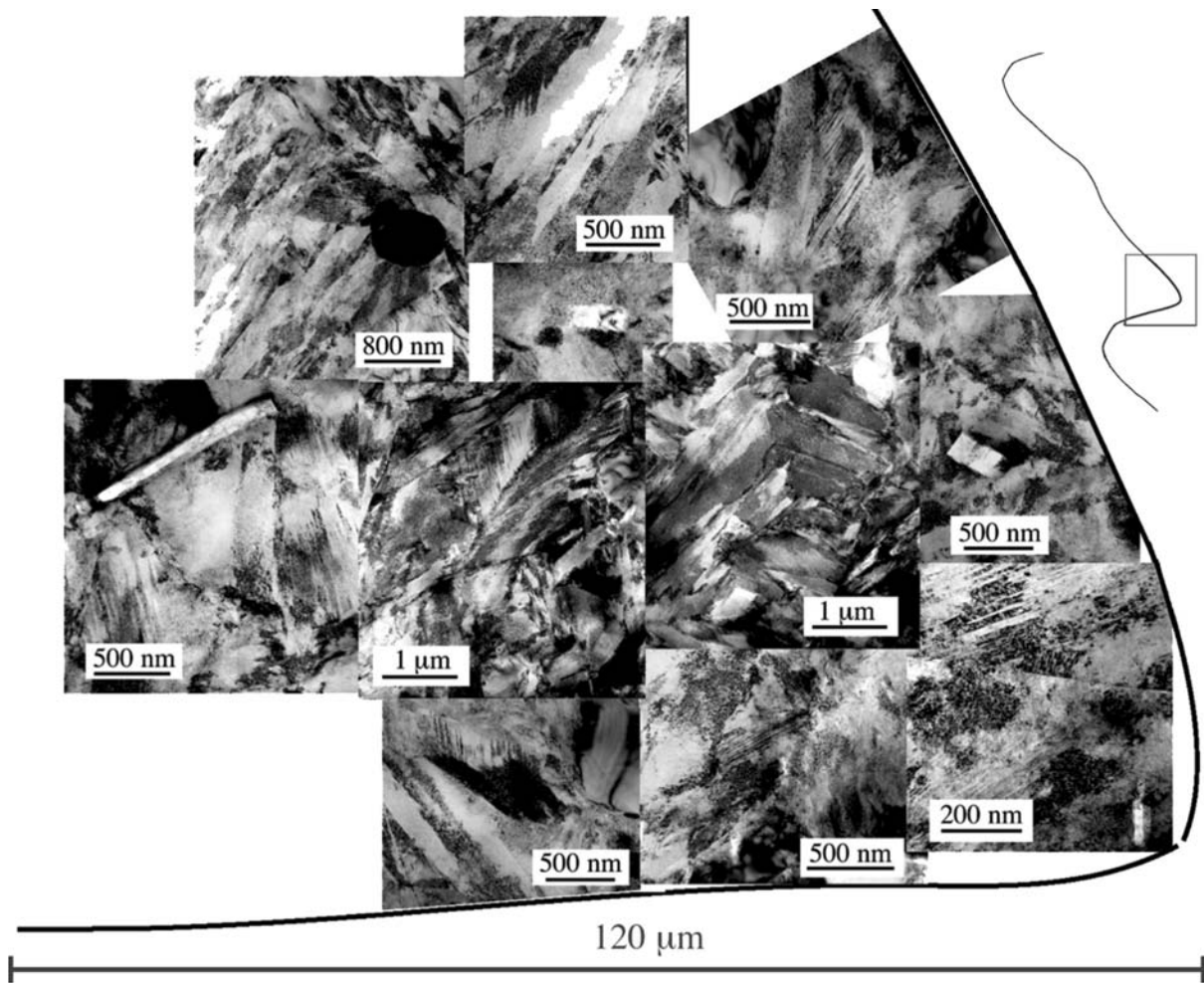


FIGURE 3.11. TEM observation of a tooth of a BF file. Individual images are placed at the corresponding distance from the tooth tip.

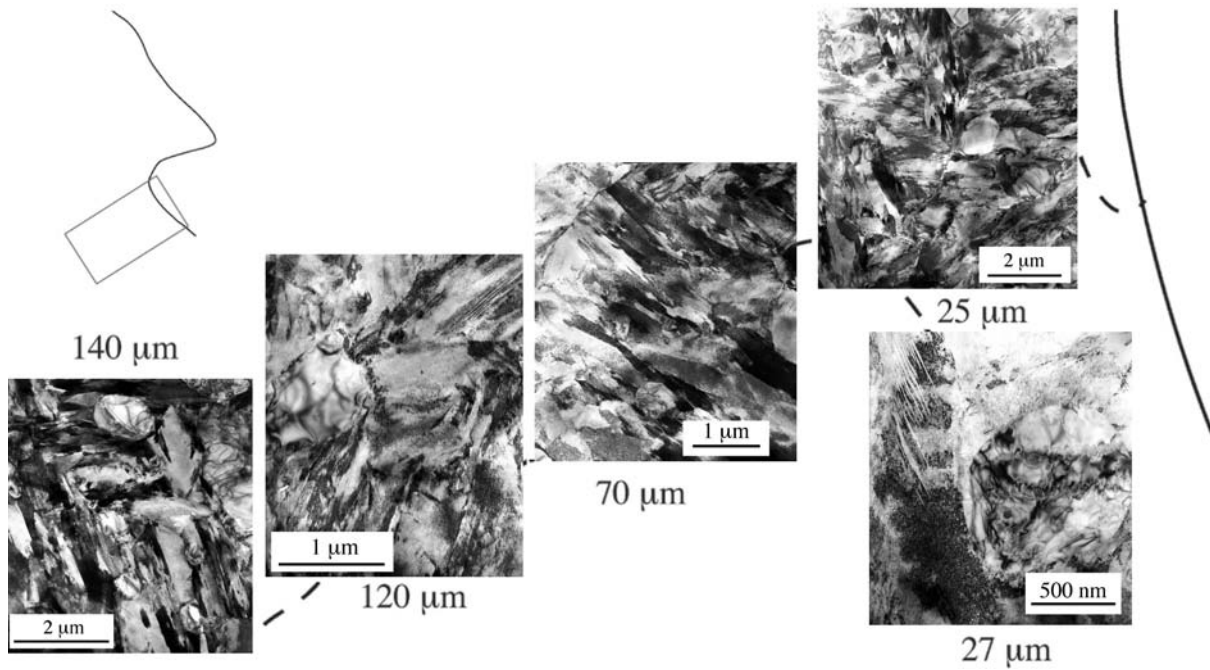


FIGURE 3.12. TEM observation of the bulk of a BF file. The distance from the surface is marked for each image.

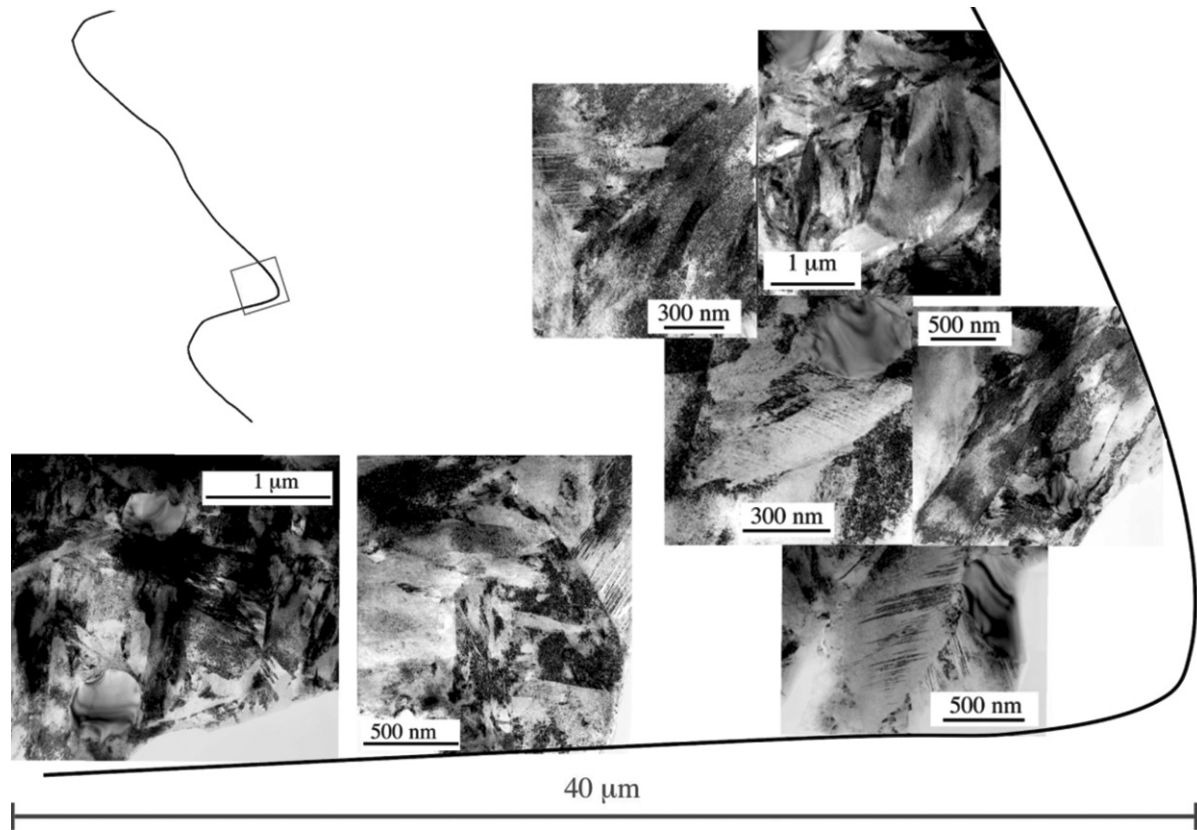


FIGURE 3.13. TEM observation of a tooth of a CN file. Individual images are placed at the corresponding distance from the tooth tip.

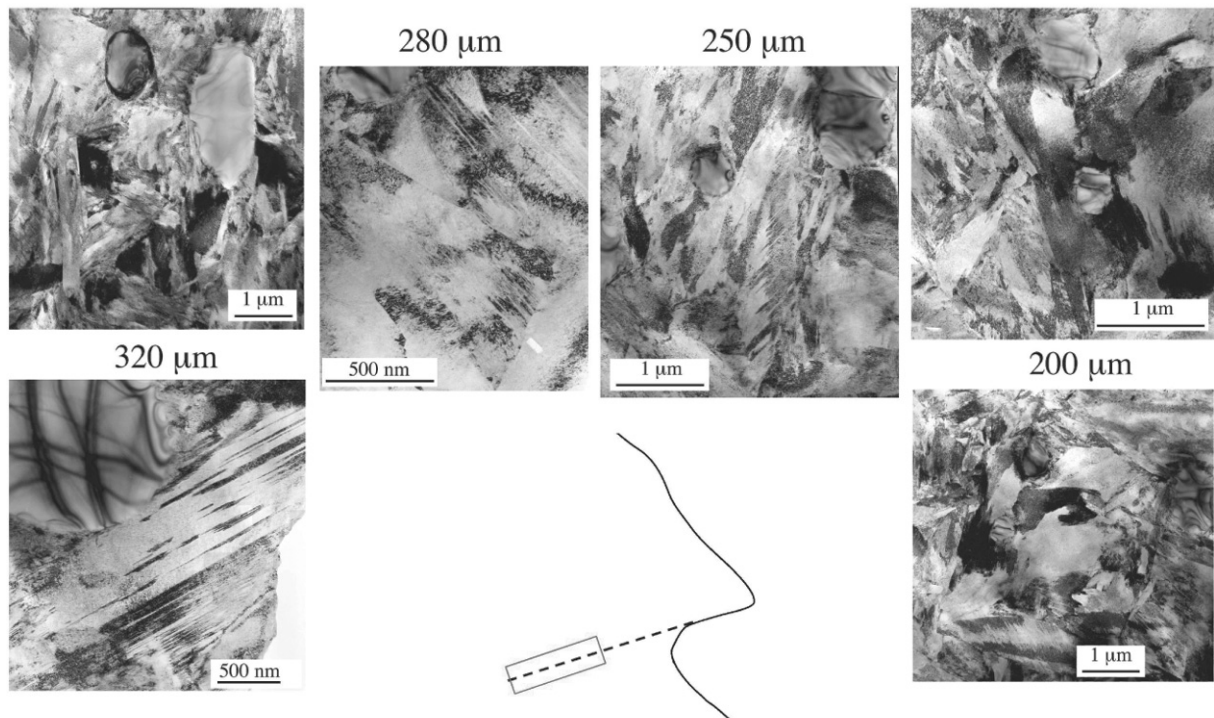


FIGURE 3.14. TEM observation of the bulk of a CN file. The distance from the surface is marked for each image.

3.2 Thermoelectric power

Thermoelectric power proves to be remarkably sensitive to the microstructural changes in the material. Figure 3.15 shows how thermopower, measured on whole files, varies from one stage of the file production to the next. Through the processes of the preparation of the file shape before the quench, which requires heavy machining, the TEP decreases ($\Delta S \approx 0.3 \mu\text{V/K}$). But an abrupt change in the TEP in a much larger scale happens after heat treating and quenching the files, which causes the change of their microstructure from ferritic to martensitic. This later process causes a drastic decrease in the TEP, ΔS being in average $4 \mu\text{V/K}$ for CN and $4.7 \mu\text{V/K}$ for BF treated files. Before going into analysis of what causes this decrease, it should be pointed out that fig. 3.15 evidences that the TEP allows the distinction between the two types of thermal treatment of the files in a simple and truly non-destructive manner: BF treated files have a lower TEP than those treated in CN.

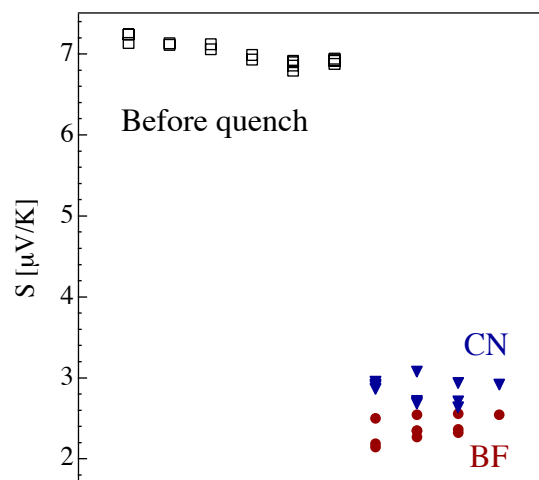


FIGURE 3.15. TEP changing with file production process. The abscissa presents consecutive production steps. Squares: stages before the quench, triangles: CN files, circles: BF files. Quenching causes a drastic decrease of the TEP. The TEP is higher for CN than for BF treated files.

However, no absolute value can be attributed to either type of the file treatment: after the quench, the TEP varies as a function of aging at room temperature. The TEP measurements presented in fig. 3.15 are performed after long aging at room temperature. The increase of the TEP for two batches of files, BF or CN treated, is shown as a function of aging time in fig. 3.16. Although the difference between CN and BF files persists even after long aging (as do the differences between the individual files within each batch), this difference is not constant. In fig. 3.17, the TEP variation with aging time is shown with the time axis on a logarithmic scale, and a curve is added presenting the difference of average values $S(\text{CN}) - S(\text{BF})$ on the right-hand scale. As seen from the figure, the average difference decreases with aging time.

The TEP of a material depends strongly on the material microstructure. In the case of steel, it was shown in Chapter 2 that the TEP varies inversely with the amount of carbon in solid solution and also with the amount of dislocations in the material. As shown in figures 3.16 and 3.17, the TEP increases with aging after quenching. As at room temperature no change of the dislocation density is expected, this increase of the TEP can be attributed to the decrease of the amount of interstitial carbon, the process widely studied in virgin martensite.

The effect of the dislocation density is studied by roll-milling a non-quenched, ferritic sample at room temperature (note that due to its hardness and brittleness it is not possible to roll-mill the martensite). The TEP was then measured as a function of deformation (fig. 3.18). The

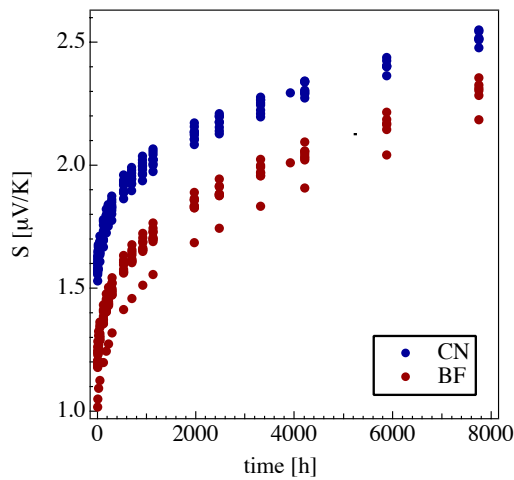


FIGURE 3.16. Effect of room temperature aging on file TEP.

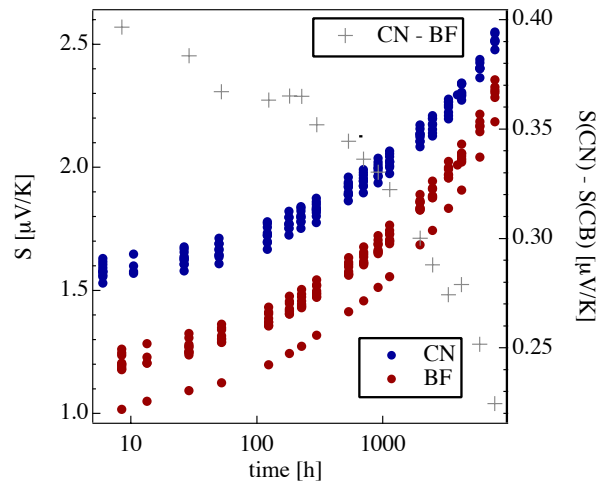


FIGURE 3.17. The average difference of TEP between BF and CN files decreases with aging time.

deformation was calculated from the thickness variation as $(h_0-h)/h_0$, h_0 being the initial thickness and h the thickness after the milling. The decrease of the TEP from its starting value of $6.99 \mu\text{V/K}$ is relatively steep at the beginning, but after a deformation of 35 % it becomes linear, with the slope of $-0.40 \pm 0.01 \mu\text{V/K}$. The same coefficient is found for pure iron with the decrease being linear from the beginning of the deformation process [Borrelly 1985]. Although the dislocation density created by milling remains unquantified, this experiment shows that the effect is relatively small compared to the one due to the interstitial carbon concentration. Furthermore, the TEP decrease upon roll-milling might not be only due to the increase of the dislocation density. Possibly some of the cementite dissolves due to the heavy deformation. Evidences for the dissolution of cementite and supersaturation of ferrite with carbon has been found in cold-drawn pearlitic steel [Languillaume 1997, Taniyama 2004].

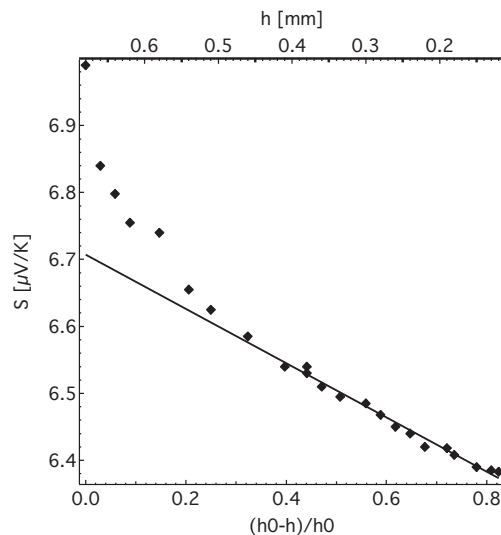


FIGURE 3.18. Effect of roll milling on the ferritic material. The decrease of the TEP becomes linear after a deformation of 35% with the slope of $-0.40 \pm 0.01 \mu\text{V/K}$ which is found in pure iron.

At this point, it is possible to relate the decrease of the TEP after heavy machining during file shape preparation to the increase of the dislocation density. The big decrease of the TEP after

the quenching procedures is caused both by the increase of the dislocation density and the amount of carbon dissolved in the iron matrix, the second being more important.

While performing the measurements of TEP on the whole files, another distinction between differently treated files was observed (fig. 3.19). After placing the file on the measuring apparatus (described in section 2.3) and tightening it, it takes a certain time for the TEP value to stabilize. This transition period is different for CN and BF treated files. The value measured for BF files increases very fast in the first 20 seconds, reaching a value even slightly higher (0.02 $\mu\text{V/K}$) than the final one, and then it stabilizes within the next minute. On the contrary, for CN files, the increase towards the final stable value is much longer (120 s), and the final value is never exceeded in the transition period.

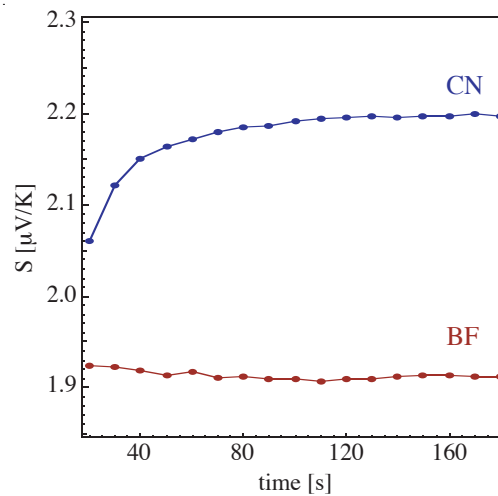


FIGURE 3.19. Transient effect of stabilization of the TEP value during a measurement. The slow increase characterizes CN files, and a rapid increase in the first few seconds (not measured) followed by a slight decrease is characteristic for BF files.

The measured TEP depends on the temperature gradient in the sample, and it takes a certain time for the gradient to be established across the file. At first instants, only the file teeth are in contact with the copper blocks at different temperature. Therefore, a possible explanation for the transition effect is that at different instants, a different region of the file is contributing to the measured value, starting from the file surface, and approaching the average value where the main contribution comes from the file core.

To confirm this hypothesis, samples extracted from different regions of the file were measured separately. The samples were obtained from three layers, two from the file surfaces, containing the teeth (in total 0.5 mm thick), and one from the core of the file (1 mm thick). Each layer was then cut into 3x3 samples, resulting in samples 40 mm or 50 mm long and 4 mm wide (fig. 3.20).



FIGURE 3.20. File cutting scheme.

Therefore, 27 samples per each file were individually measured. The samples were put lying flat on the TEP installation temperature blocks, and for each sample two measurements were made interchanging the side in contact with the blocks by simply turning the sample upside-down. The results are presented in fig. 3.21a for the samples extracted from a BF file and in fig. 3.21b for a CN file. The measured TEP for each sample (an average between the “up” and “down” value) is displayed as a filling of a wireframe presenting the sample, according to the scale indicated. The filling is in full color for bulk samples, and in striped pattern for samples with teeth. The gray samples in fig. 3.21b are those whose TEP was not measured because the samples were already used for other purposes.

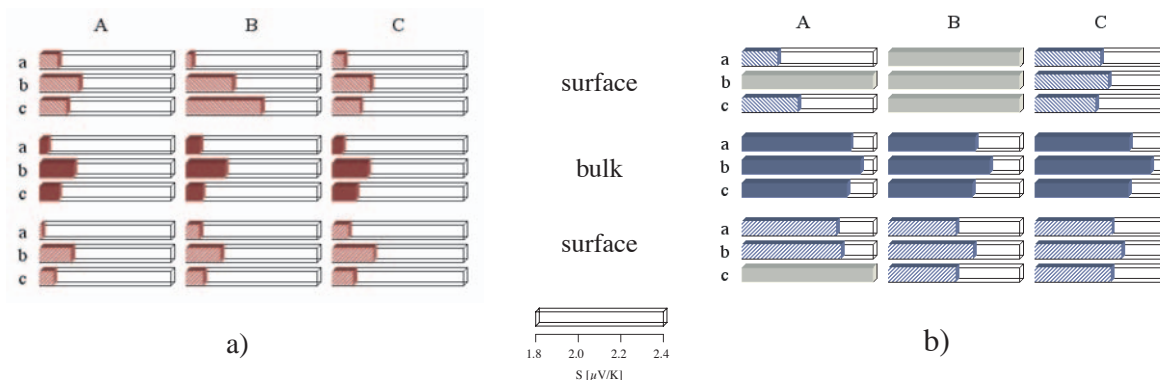


FIGURE 3.21. TEP displayed as a filling of a wireframe presenting a sample, according to the scale indicated, for samples extracted from different regions of the BF (a) and CN file (b) corresponding to the cutting scheme in fig. 3.20. The filling is in full color for bulk samples, and in striped pattern for samples with teeth. The gray samples in b) are those whose TEP was not measured.

The difference between CN and BF files seen on the whole files, that is CN files having higher TEP, is confirmed also on the extracted samples, especially those from the bulk of the files. This therefore casts away any doubt that the measured difference between the files treated in different manner comes from potential geometrical differences. The TEP of transversely central pieces (which are marked with letter b in fig. 3.21) in each layer is higher than that of the neighboring samples (marked a and c). This is probably due to the less drastic quench (being further from the surfaces) resulting in lower concentration of interstitial carbon. There is no striking variation of the TEP in the longitudinal direction (A, B, C in the figure). The results are summarized in fig. 3.22, but this time the averaging was made for each layer, taking into account the orientation of the sample. The abscissa presents a cross-section of the file. The points at the ends are the average TEP for the samples with teeth, measured with the teeth in contact with the temperature blocks. The points second to the outer ones are the average from the measurements with teeth facing up and with the flat side in contact with the blocks. The orientation of bulk samples was more difficult to determine, so the two central points present the average of lower and higher TEP values obtained by turning the sample (the difference is not very significant). This representation shows that there is a stronger variation of TEP within the CN than the BF file, with the TEP of the samples containing teeth being in average $0.15 \mu\text{V/K}$ lower than the value measured for the bulk samples. Conversely, in the BF file, the samples from the surface had an even slightly higher TEP than those from the core.

An additional proof of the variation of the TEP in the file profile is the experiment made by thinning the samples containing teeth. The sample thickness was reduced by mechanical polishing, removing the bulk material and leaving the teeth on less and less support. The TEP was measured in between consecutive polishing steps, starting from the initial sample thickness of 0.7 mm (the height of the teeth being 0.2 mm) to the point when samples broke. As seen from fig. 3.23, the TEP decreases for the CN sample, and increases for the sample extracted from the

BF treated file. Notice that the initial values of TEP are higher than in fig. 3.22 because the samples used were aged for longer time prior to the measurement.

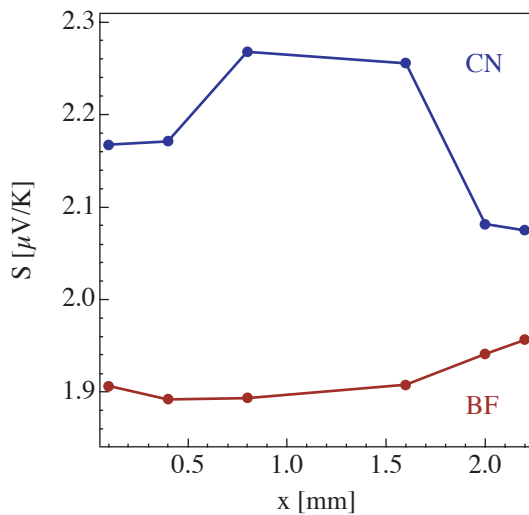


FIGURE 3.22. TEP variation across a file profile. The abscissa presents the cross-section of the file and the points are obtained by averaging the values for different layers and different orientation of the sample during TEP measurement.

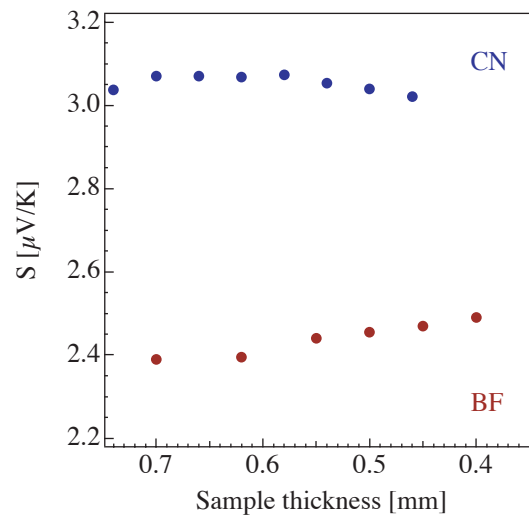


FIGURE 3.23. TEP of samples with teeth as a function of the sample thickness. Thickness is reduced by polishing away the bulk material leaving teeth on less and less support. The TEP increases for BF and decreases for CN sample. The starting values for TEP are higher than in fig. 3.22 because the samples used were aged prior to the measurement.

A comparison of these results with the transient effect (fig. 3.19) upholds the above stated hypothesis that the TEP measured after the first few seconds comes from the surface of the file, stabilizing after approximately two minutes to an average value where the contribution to the TEP comes more from the file core.

We performed some numerical simulation by finite element, using the software Calcosoft by Calcom, of the temperature distribution in the file as a function of time. They show that the characteristic time for which a vertical temperature gradient in the file teeth is observed is much shorter (order of seconds) than the time necessary to reach the stable TEP value. However, the time for temperature stabilization (taking into account a rather poor thermal contact between the copper blocks and the sharp file teeth) is comparable to the time necessary for the TEP stabilization observed for CN files. The time constant of 2 min was also found experimentally in a rather crude experiment when a thermocouple was put between the file and the teflon screw and temperature and TEP reading was performed in parallel.

The origin of this transient phenomenon remains thus still unclear and interesting for further analysis.

3.3 Mechanical tests

3.3.1 Compression

An example of stress-strain curves obtained in compression is presented in fig. 3.24. Although there are small differences in the plastic behavior within each batch, it is rather evident that the samples extracted from a BF treated file have a higher compressive strength. Averaging the results of four samples for each file gives the value for compression strength 3690 ± 90 MPa for the BF, and 3480 ± 80 MPa for the CN treated file. The yield stress at 0.2% deformation for BF samples is 2890 ± 70 MPa compared to 2760 ± 40 MPa for CN.

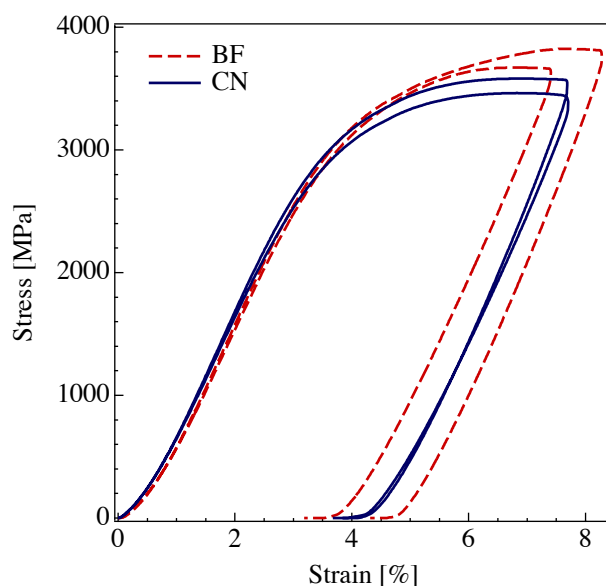


FIGURE 3.24. Example of compression test stress-strain curves showing that bulk samples from BF files have a higher compressive strength.

3.3.2 Nanoindentation

The hardness of the files was probed by nanoindentation. The indents were made on a polished file cross-section, going from one surface of the file to the other, in the attempt to measure a potential variation of the hardness along the file profile (fig. 3.25). The spacing of the indents in the file profile was $250 \mu\text{m}$, and the maximum indentation depth $4 \mu\text{m}$. On the tooth, the indents were made up to $1 \mu\text{m}$, with the distance between neighboring indents being $75 \mu\text{m}$ (fig. 3.26). Although the choice of the indent depth defines the tested hardness more as micro-hardness than nanohardness, this depth was chosen taking into consideration that the material microstructure is composed of carbides embedded into a matrix, with the aim of testing the average properties. In fig. 3.27, the indent size for a $4 \mu\text{m}$ deep indent can be compared with the size of cementite particles distinguishable as a relief at the surface. The length of the indent side is $28 \mu\text{m}$. The pile-up effect at the indent edges is also visible in the figure.

The load-displacement curves for the $4 \mu\text{m}$ indents along the profile for both BF and CN files are presented in the fig. 3.28. It is evident that a higher stress is required for the same depth of penetration of the probe in the BF files indicating a higher hardness. The difference in the necessary load becomes more and more evident as the displacement into the surface increases.

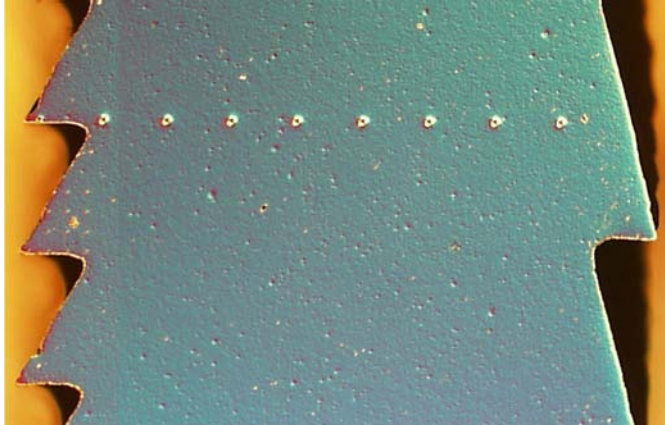


FIGURE 3.25. Optical microscope image of a series of indents made in the file profile (to the depth of $4\ \mu\text{m}$). The indents are $250\ \mu\text{m}$ apart.



FIGURE 3.26. Placing of the indents on the file tooth. The distance between the indents is $75\ \mu\text{m}$ and the indentation depth $1\ \mu\text{m}$.

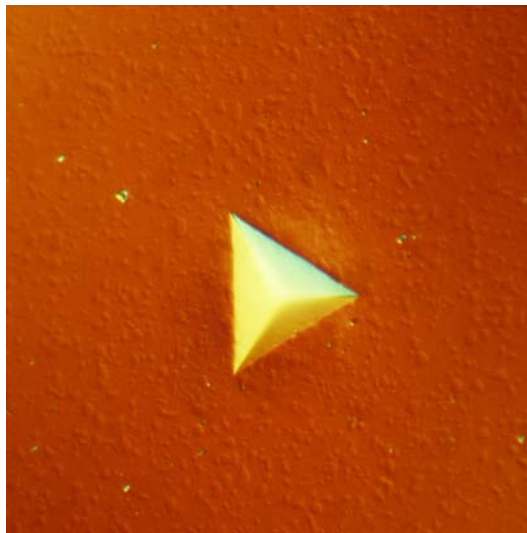


FIGURE 3.27. Optical microscope image of the indent made in the bulk of the file (CN). The length of the indent side of $28\ \mu\text{m}$ can be compared with the size of cementite particles that appear as a relief due to the light interference contrast. The pile-up effect at the indent edges is also visible.

The hardness measured by the continuous stiffness method during the loading is shown in fig. 3.29a as a function of the penetration depth. The measurements become meaningful only for a displacement into the surface higher than $500\ \text{nm}$, below this value the effects of structure inhomogeneity lead to a huge scatter. As seen from the graph, BF treated files have a higher hardness. The hardness, averaged for the indenter displacement into the surface between 1000 and $1200\ \text{nm}$ and then over all indents, is $11.3\pm 0.3\ \text{GPa}$ for the CN and $11.6\pm 0.2\ \text{GPa}$ for the BF treated file. However, no variation of the hardness is observed as a function of the distance from the file surface due to the large fluctuations in the measured value. The region closer than $50\ \mu\text{m}$ from the surface could not have been tested successfully with $4\ \mu\text{m}$ deep indents, due to tooth edge effects.

The elastic modulus measured by the continuous stiffness method is presented in fig. 3.29b. As for the hardness, the fluctuations of the measured values impede the determination of the possible variations along the file profile, but it is possible to say that in average we measure a higher modulus for the BF than for the CN treated file. The average, obtained in the same manner as

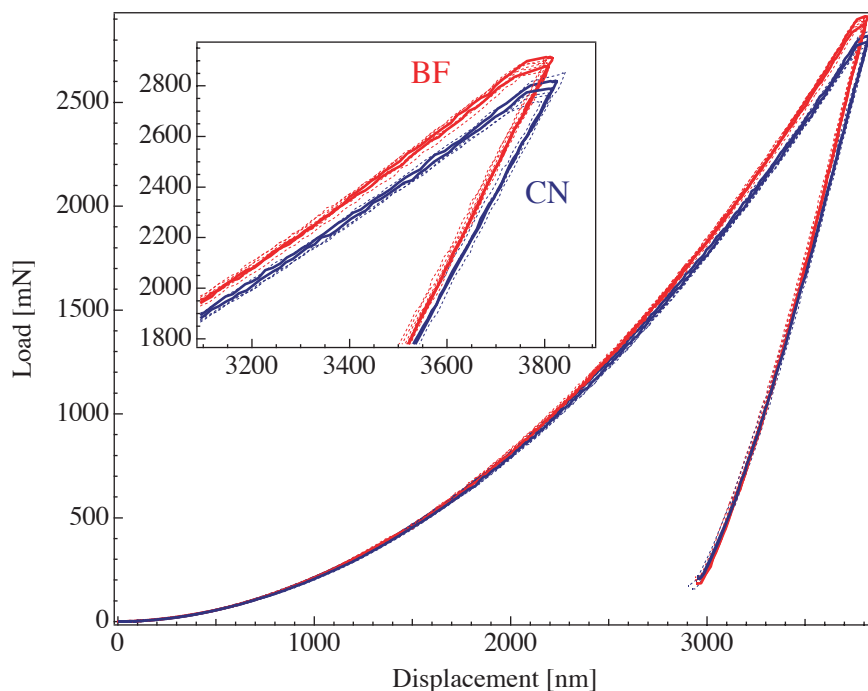


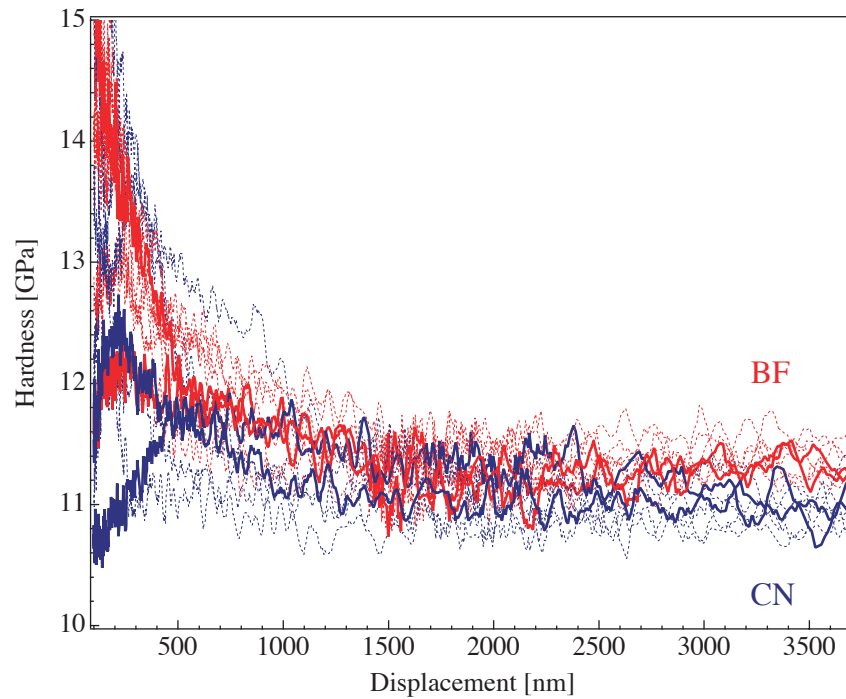
FIGURE 3.28. Load versus displacement into surface for indents made along the profile of the file. As the indent depth increases, a load higher for BF than for CN file is necessary for the same displacement, which indicates higher hardness.

for the hardness measurements, is 225 ± 5 GPa for the CN and 238 ± 6 GPa for BF treated file. These values depend on calibration and should be considered only as relative values.

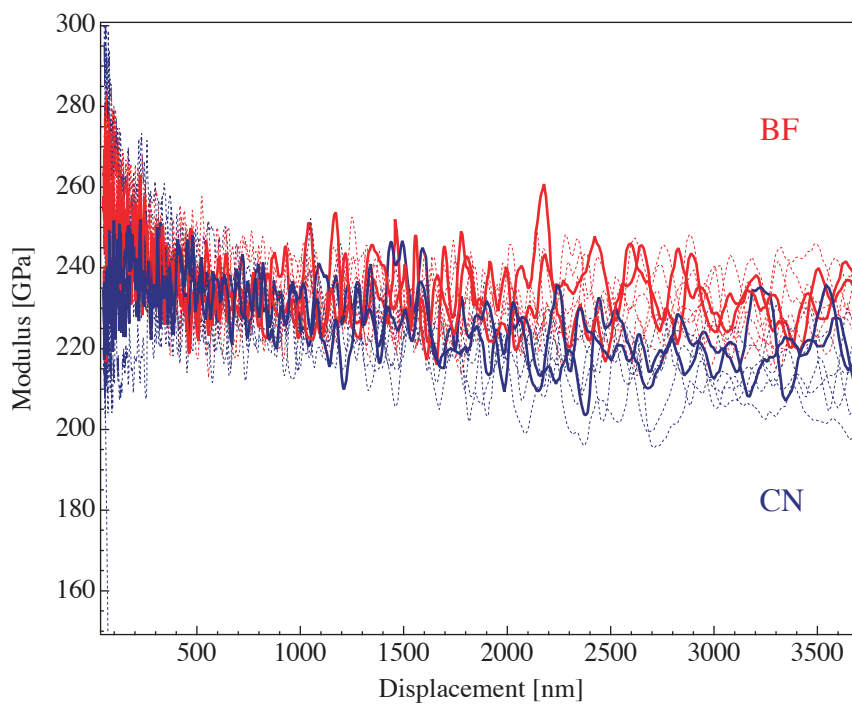
Measurements performed on teeth show a similar relation between BF and CN treated files as measured in the profile, the curves practically superimpose those presented for the profile measurements. Because of the smaller indentation depth, the relative scatter is bigger, and it is impossible to extract an ordering proving possible hardness variations.

3.4 Conclusions

The microstructure of the file material is complex and TEM or AFM analysis show no differences between the microstructures issued by BF or CN heat treatment. On the other hand, the TEP has proven to be sensitive enough to distinguish between the two. At this point, it can be concluded that BF treated files have in total more carbon in solid solution in the martensitic matrix. In addition, the existence of a carbon concentration variation in the file profile has been evidenced by the TEP experiments. The BF files have a lower interstitial carbon concentration in the teeth than in the bulk while the opposite situation is found in CN treated files. The results of the mechanical tests indicate that the resistance to deformation could be related to the amount of carbon in solid solution. The samples extracted from the bulk of BF treated files have higher yield stress and compression strength. Also, the hardness measured by nanoindentation is found to be higher for the BF compared to the CN treated files. However, due to the relatively large experimental uncertainty, no hardness variation along the profile of the file is evidenced.



a)



b)

FIGURE 3.29. Hardness (a) and elastic modulus (b) measured by the continuous stiffness method. To facilitate the reading of the graph, only the curves for the indents in the middle of the file cross-section are drawn with full line, and those for indents closer to the teeth are drawn with dotted line. BF treated files have higher hardness and modulus. The fluctuations of the measured values are too big to observe any variation of hardness or modulus along the profile.

The results presented in the previous chapter emphasize the importance of interstitial carbon for the mechanical properties of the material, namely its hardness and strength. Mechanical spectroscopy is known to be a very sensitive indicator of the interactions of soluted atoms with dislocations and of their mobility, and it is thus chosen as a technique to get a better insight into these mechanisms, which are also responsible for the macroscopic mechanical properties of the material.

4.1 Temperature spectra

4.1.1 High and low frequency spectra for martensite

The typical internal friction and frequency spectrum, measured in the vibrating reed installation during a first heating of a martensitic sample and then in cooling after 1 h of tempering at 800 K, is shown in the fig. 4.1. The differences in internal friction spectra for the samples extracted from files that underwent different thermal treatments are very small (not visible in this scale), and will be discussed separately. The IF spectrum obtained in heating can be decomposed into five broadened Debye shaped peaks and an exponential background [Mari 1999], as presented in fig. 4.2. The parameters of the peaks, i.e. peak amplitude, temperature, activation energy and broadening factor, as obtained by a peak fitting procedure, are listed in the same figure.

A typical internal friction and frequency measurement performed in the inverted torsion pendulum during heating, 1 h tempering at 700 K and the following cooling of the initially martensitic sample is presented in fig. 4.3. The equivalent decomposition into broadened Debye shaped peaks (without the peak P1 which is not distinguishable in the spectrum) and an exponential background is presented in fig. 4.4.

A comparison of the internal friction spectra obtained in both installations reveal that four of the peaks found in the spectrum are thermally activated: the temperatures of the peaks P1, P2, P4 and P5 depend strongly on the measurement frequency. The activation energy and the attempt frequency calculated for the thermally activated peaks according to eq. 2.27 are given in table 4.1. The relaxation parameters for the peaks P2 and P5 are calculated based on 10

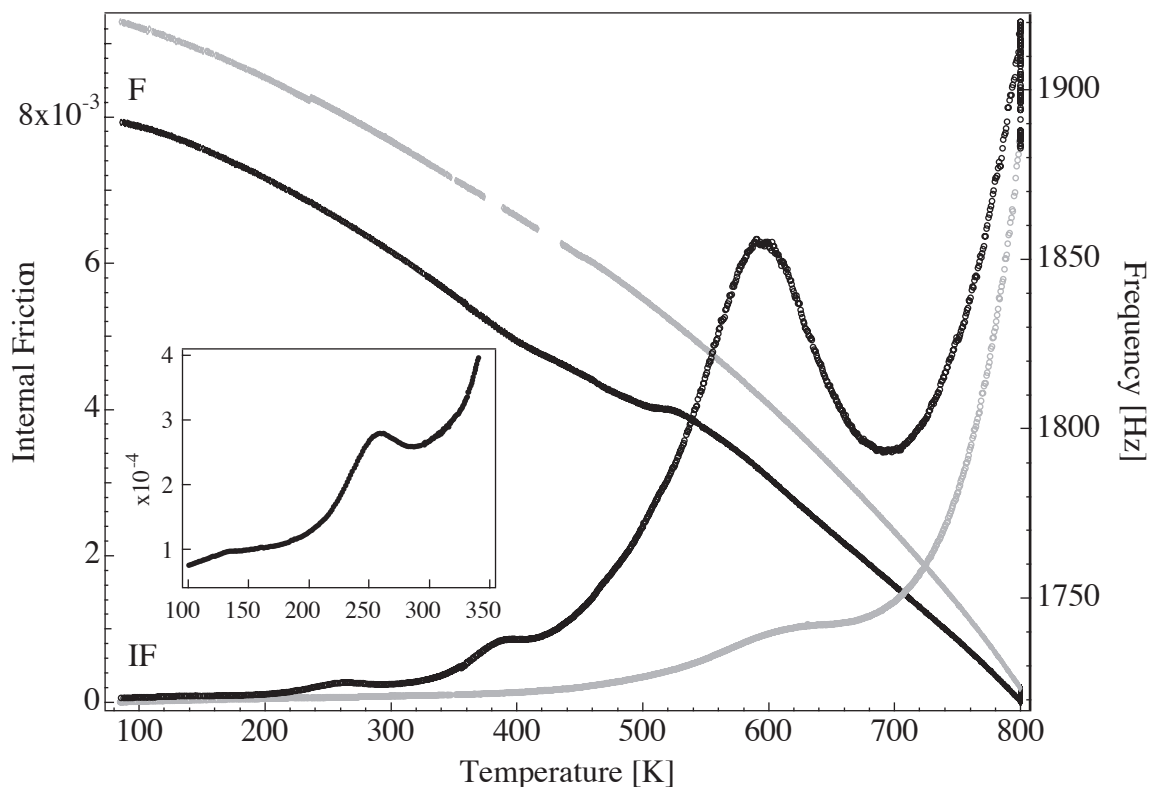


FIGURE 4.1. Internal friction and frequency measured in the vibrating reed setup during the first heating (black) of a martensitic sample and then during cooling after 1h of tempering at 800 K (gray). Lower temperature peaks are magnified in the inset.

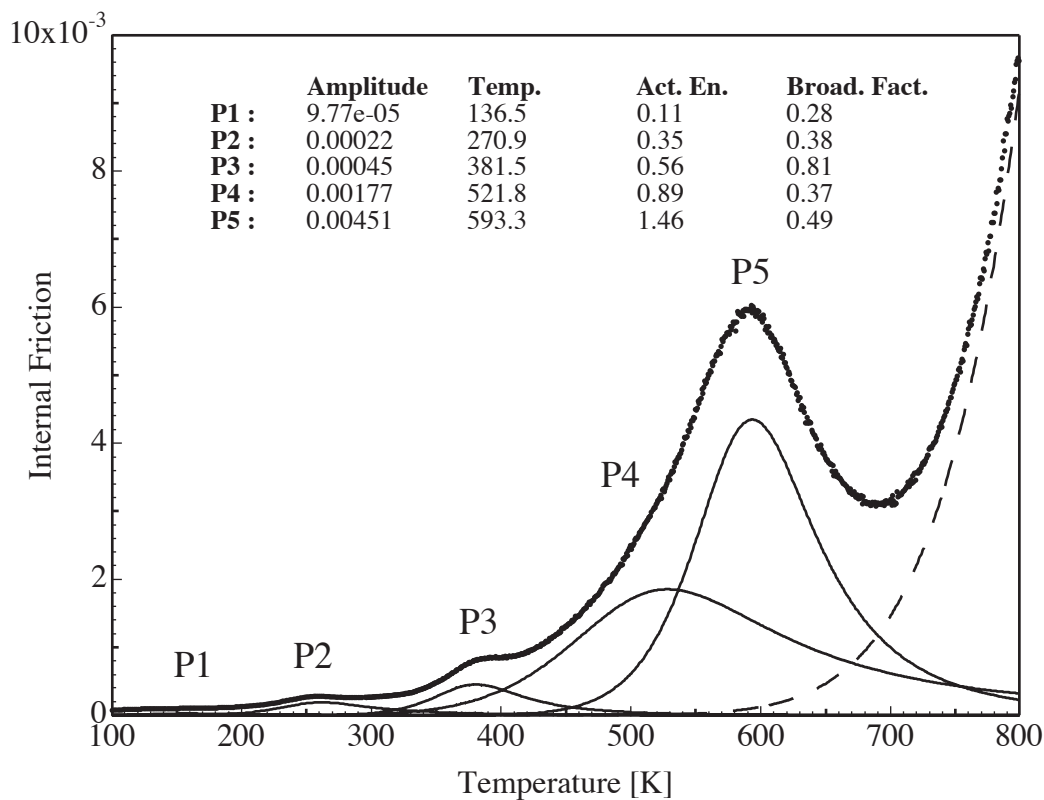


FIGURE 4.2. Internal friction spectrum obtained during heating of a martensitic sample, decomposed into five Debye peaks and an exponential background. The parameters of the peaks, as given by the fitting procedure [Mari 1999], are listed.

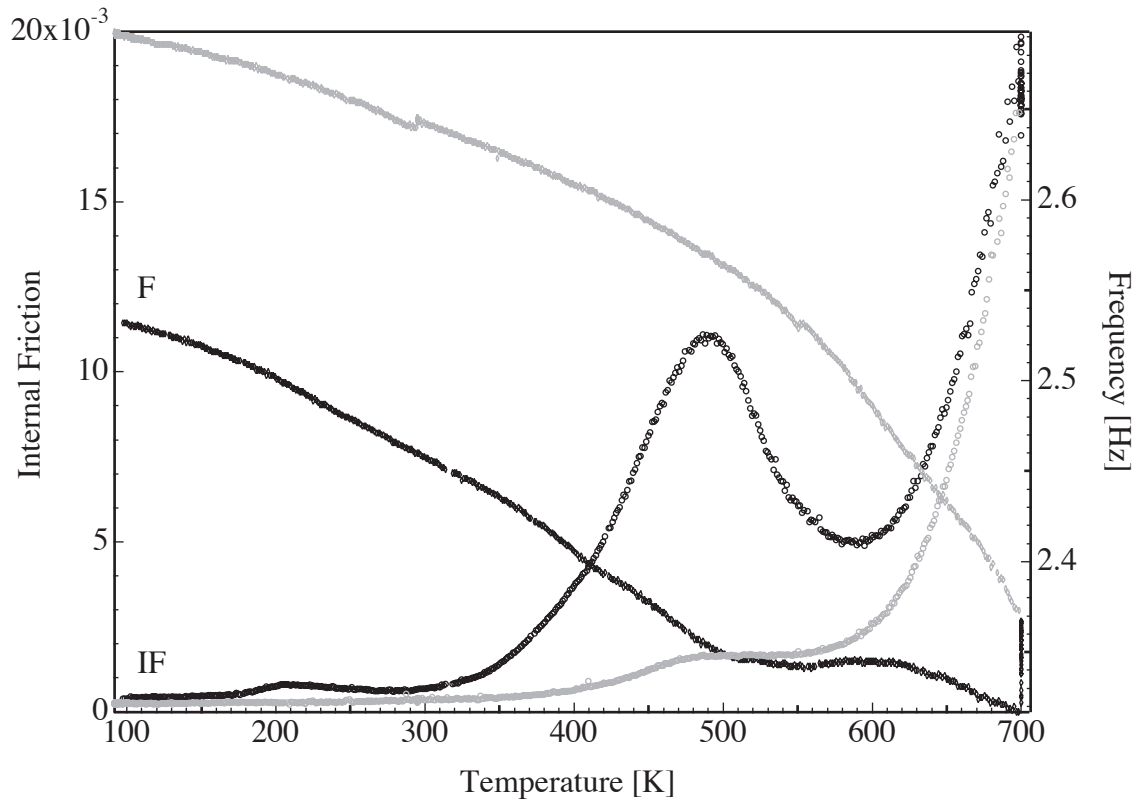


FIGURE 4.3. Internal friction and frequency measured in the inverted torsion pendulum during the first heating (black) of a martensitic sample and then during cooling after 1h of tempering at 700 K (gray).

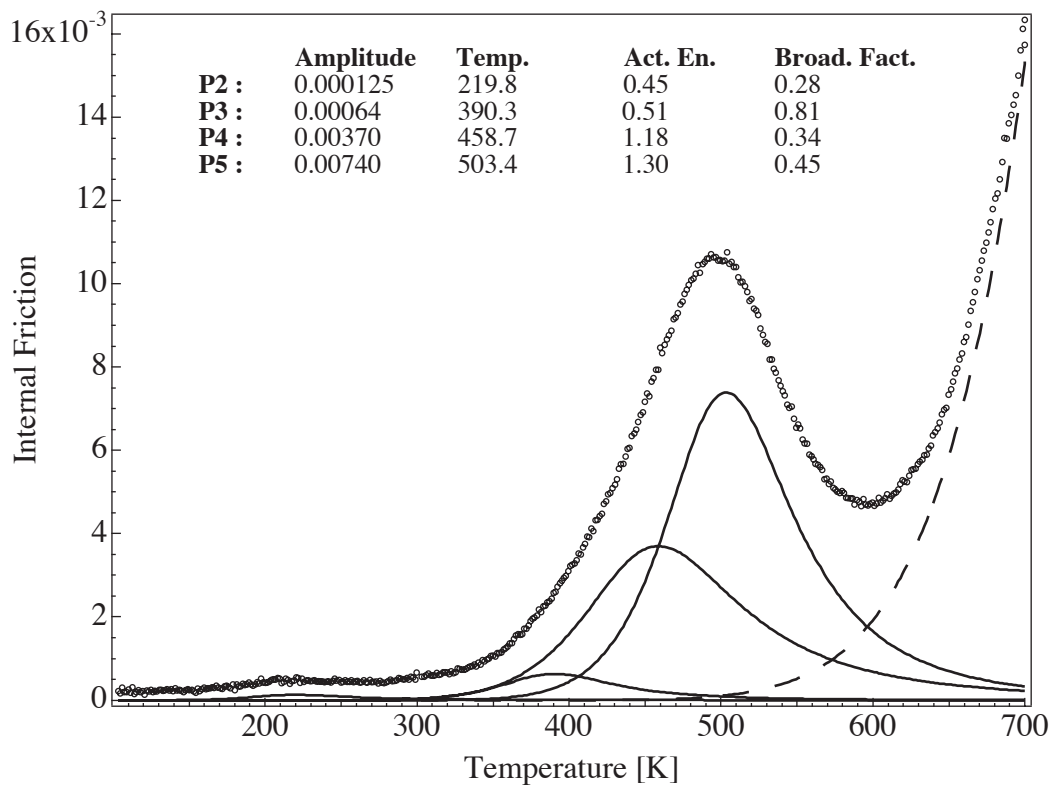


FIGURE 4.4. Internal friction spectrum obtained during heating of a martensitic sample in the inverted torsion pendulum, decomposed into five Debye peaks and an exponential background. The parameters of the peaks, as given by the fitting procedure [Mari 1999], are listed.

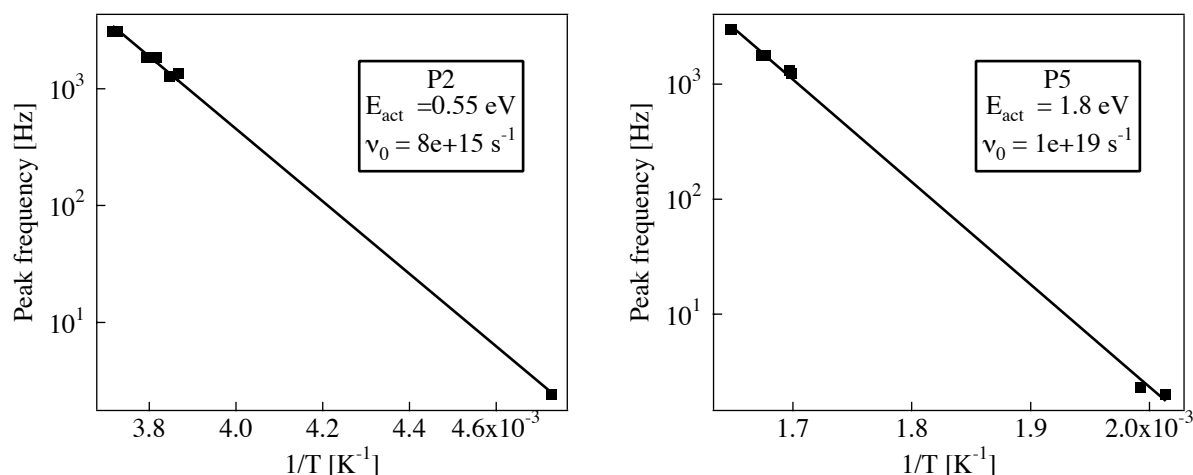


FIGURE 4.5. Arrhenius diagrams for the calculation of activation energy and attempt frequency for peaks P2 and P5 using peak positions in 10 spectra obtained in the vibrating reed (kHz region) installation and the torsion pendulum (Hz region) by varying the sample thickness.

Peak	Activation energy [eV]	Attempt frequency [s^{-1}]
P1 [Bagramov 2001]	0.27	10^{14}
P2	0.55 ± 0.05	10^{16}
P4	2.2	10^{25}
P5	1.8 ± 0.1	10^{19}

TABLE 4.1 Activation energy and attempt frequency for thermally activated peaks found in IF spectrum of martensite.

spectra measured in both installations with samples of different thickness (fig. 4.5). The calculation for the peak P4 is based only on the two fitted spectra presented in fig. 4.2 and 4.4. The obtained values for the relaxation parameters are discussed in paragraph 4.2.

The peak P3 does not seem to be thermally activated, it is found around the same temperature in both installations. The absence of a modulus decrease which is expected in coincidence with relaxation peaks is another indication that the peak P3 is not a relaxation peak. The peak P3 coincides with a change of the modulus in the opposite direction: the curvature of the frequency curve (obtained in the vibrating reed installation) changes at the peak position, reflecting an increase in the modulus (fig. 4.6). Another, stronger increase in the modulus is observed around 500 K where a plateau is formed in the frequency spectrum. A decrease of the modulus occurs in correspondence with the peaks P4 and P5. The effects of the low temperature peaks (P1 and P2) on the modulus are not visible because of the low amplitude of the peaks. The comparison of the frequency spectra obtained by both installations are presented in fig. 4.7. The frequencies are normalized to the room temperature value. The increase of the modulus observed coinciding with the peak P3 is not visible at low frequency because of the stronger decrease due to the peaks P4 and P5, which are in this case at lower temperature. Moreover, a longer plateau is observed at low frequency above 500 K due to the fact that in this case the peaks P4 and P5 precede this effect.

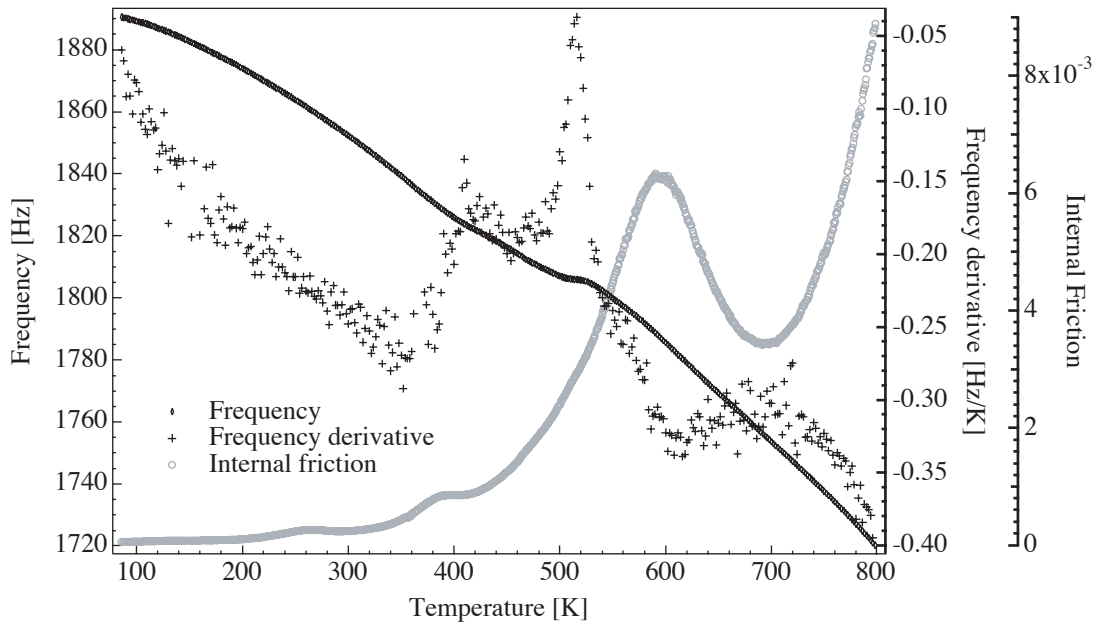


FIGURE 4.6. Frequency measured in the vibrating reed installation and frequency derivative showing the changes of the modulus, compared with the internal friction spectrum.

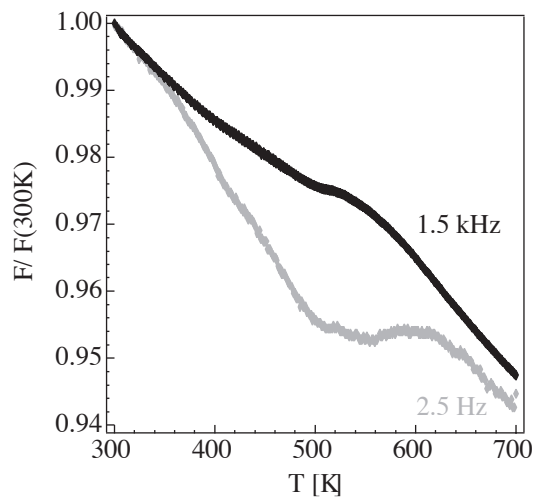


FIGURE 4.7. Comparison of frequency spectra obtained in the vibrating reed installation (~ 1.5 kHz) and torsion pendulum (~ 2.5 Hz). A plateau starting at 500 K is visible in both high and low frequency measurements.

4.1.2 Evolution of martensitic spectra with aging and tempering

The results presented above are obtained using martensitic samples extracted from files that have been aged at room temperature for at least one year. To verify if some of the observed relaxation phenomena are due to nitrogen, some samples for mechanical spectroscopy are heat treated for 30 min at 1100 K under argon or nitrogen atmosphere and then quenched in water at room temperature. No relative difference of the internal friction spectra measured just after the quenching of the samples treated under different atmosphere is observed. However, the spectra showed significant distinctions when compared to the aged material. All following results on freshly quenched material are obtained on samples heat treated under nitrogen atmosphere.

The measurements performed in the vibrating reed installation, at frequencies of about 1.5 kHz, on freshly quenched samples are presented in fig. 4.8. The unintentional aging at room temperature is less than 30 min, which is the time necessary for oxide removal, measurements of the thermoelectric power and mounting of the sample in the installation. The IF differs from the one for long aged material mostly in the temperature region of the peaks P2 and P3. In the as quenched measurement, the peak P2 is hardly visible because of the strong rise of the internal friction that starts at the same temperature as the beginning of the peak. This increase is stopped at around 300 K where the IF shows a plateau. At that temperature, the frequency curve changes the slope as well, indicating a modulus increase. At 370 K, close to the temperature of the peak P3 in the spectrum of aged martensite, the IF decreases. The behavior of the internal friction of the sample that is aged for 24 h at room temperature is qualitatively similar. The increase of the IF however seems to start and end some 25 K later than in the measurement performed immediately after quenching, revealing more clearly the peak P2. The decrease at 370 K is common for both “fresh” measurements, and so is the further evolution of the spectra.

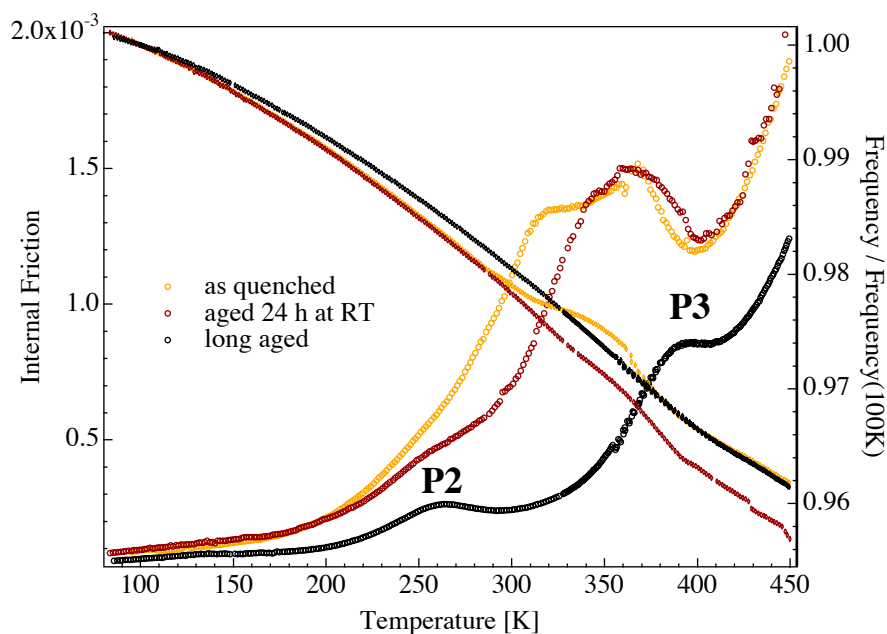


FIGURE 4.8. Internal friction and normalized frequency for an as quenched sample, a sample aged for 24 h at room temperature and a sample extracted from a file (aged for 1 year). Measurements are made in the vibrating reed setup at about 1.5 kHz.

The measurements of freshly quenched samples performed in the torsion pendulum, at about 2 Hz, are presented in fig. 4.9. The change of the IF spectra is practically the same as in the measurements at high frequency, with a strong rise of the IF at about 200 K followed by a plateau at 300 K. One should notice that the peak P2 should be positioned at 210 K at this frequency. Again, with longer aging, the IF rise is reduced and the two fresh martensite spectra meet at higher temperature (around 350 K).

The comparison of the spectra, obtained for the as quenched and for the long aged material is presented in fig. 4.10 for low and high frequency. The internal friction remains a little higher in the as quenched material up to the peak P5, which is also slightly broader. As the thermal treatment procedure is not identical in the two cases (spectra of long aged material are obtained on samples extracted from files, with probably less drastic quench), it is probable that these higher temperature differences do not arise from the effects of different aging times, but from a

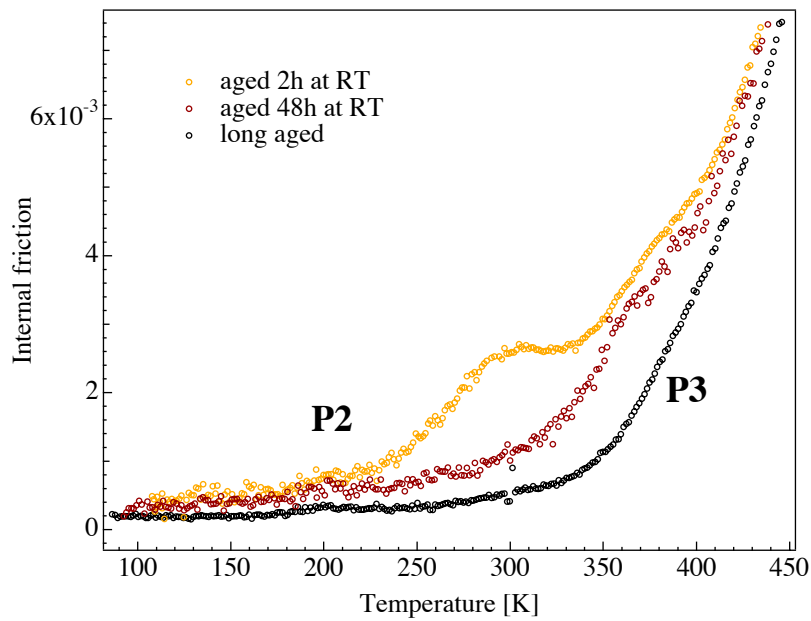


FIGURE 4.9. Internal friction for a sample aged for 2 h at room temperature, a sample aged for 48 h at room temperature and a sample extracted from a file (aged for 1 year). Measurements are made in the torsion pendulum at about 2 Hz.

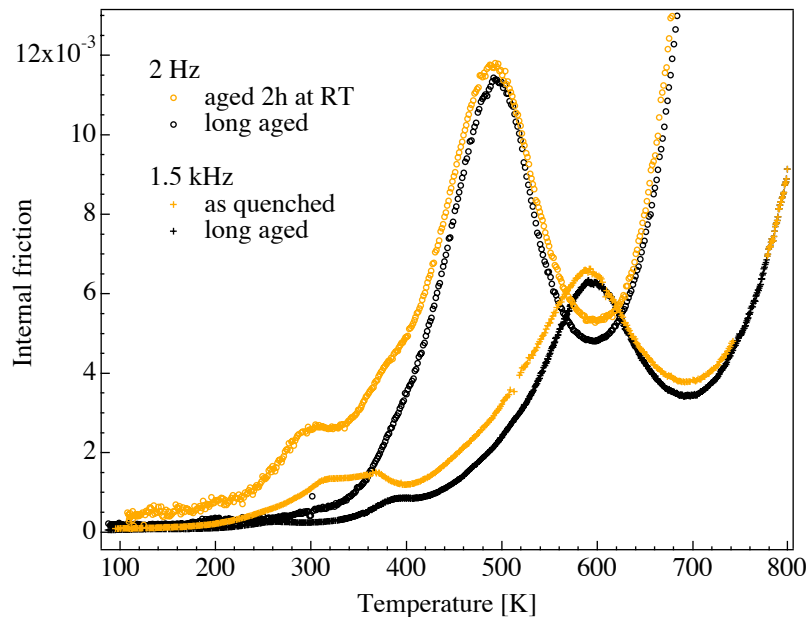


FIGURE 4.10. As quenched compared to long aged material internal friction spectra, as measured in the vibrating reed installation (about 1.5 kHz, crosses) and the torsion pendulum (about 2 Hz, circles).

slightly modified structure of the material (for example dislocation density, fraction of plate martensite etc.).

The differences at low temperature in IF spectra between long aged and freshly quenched samples are obviously due to the different aging time. One hour tempering at 375 K of a sample aged for 2 days at room temperature, which still shows a strong IF increase at 250 K, reduces the IF to the level of the long aged specimen (fig. 4.11).

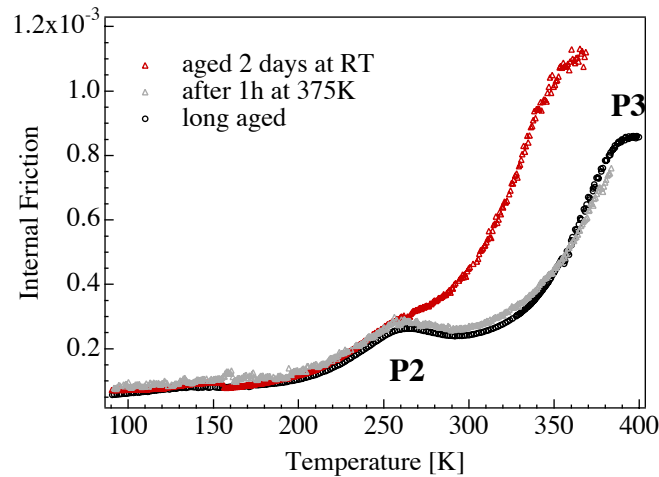


FIGURE 4.11. Internal friction increase characteristic for freshly quenched samples, which is still strong after 2 days of aging at room temperature, is no longer present after 1 h of tempering at 375 K. The IF is reduced to the level of the long aged specimen. Measurements are made in the vibrating reed setup at about 1.5 kHz.

Tempering at 800 K obviously has drastic effects on the internal friction spectrum of martensite (see fig. 4.1). It completely erases all peaks but the peak P5, the amplitude of which is however strongly decreased. The decrease of the internal friction is accompanied by an increase of the modulus. But what happens after tempering at lower temperatures? The effects of thermal cycling at subsequently higher temperatures on the frequency and on the peaks P1 and P2 in the internal friction are presented in fig. 4.12. The peak P2 is progressively decreased by heating and the frequency, i.e. the modulus, increases. The peak P1, however, is first increased by tempering at 400 K, and only decreased with further tempering at higher temperatures. Tempering at 500 K fully erases both peaks.

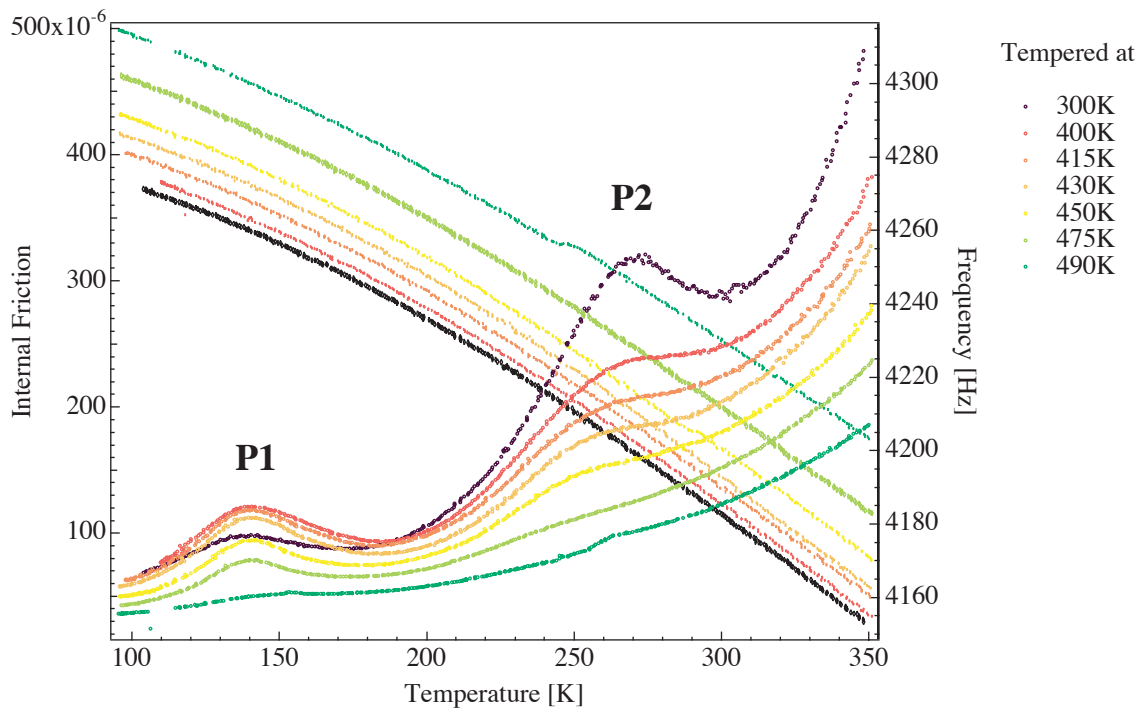


FIGURE 4.12. Internal friction and frequency spectra after successive tempering. The peak P1 shows an initial increase, while the peak P2 continuously decreases with tempering.

The evolution of the internal friction spectra above 350 K with thermal cycling is presented in fig. 4.13 for both low (a) and high (b) frequency measurements. The IF spectra presented are obtained in heating after 60 min of tempering, increasing temperature by steps of 50 K (vertical segments), starting from 450 K. They are compared with the spectrum obtained during continuous heating of the as received (long aged) file material. Tempering at 450 K completely erases the peak P3, moreover, it seems that the peak P4 is also disappearing. Yet, this tempering has very little effect on the curve at the temperature of the peak P5. To decrease the amplitude of the peak P5, it is necessary to temper at the peak temperature (500 K for measurements in the Hz and 600 K for the kHz range).

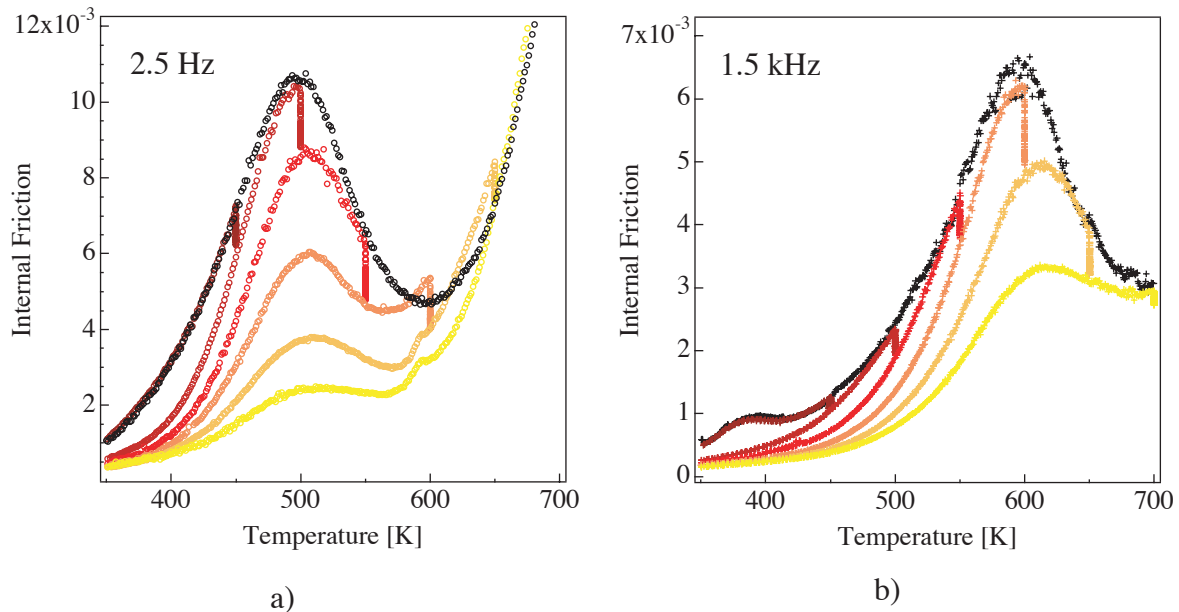


FIGURE 4.13. Effect of tempering on IF spectra measured at 2.5 Hz (a) and 1.5 kHz (b). The IF spectra are obtained in heating after 60 min of tempering at temperatures increasing by steps of 50 K. The IF spectra of the first heating of the as received material are in black.

The peak P5 is much higher when measured at low frequency. However, the comparison of the spectra after tempering, after the high temperature background (indicated with a dashed line in fig. 4.2 for high and fig. 4.4 for low frequency) is subtracted, reveals that the peak after tempering at the same temperature in both installations possibly has an even higher amplitude for high frequency measurements, at least after tempering at 550 K (fig. 4.14). It is possible however that the background as well is influenced by tempering, so the subtraction of one background has to be regarded with precaution.

It is clearly difficult to compare the peaks P5 obtained in different installations with frequencies differing by three orders of magnitude, because such a frequency difference causes the shift of the peak of about 100 K in temperature. As the spectrum, in this temperature region, is very sensitive to tempering, it is interesting to compare the peak shift with frequency using a forced pendulum that allows measurements at different frequencies on one sample. To eliminate the doubt that the peak shape changes with tempering, the structure was first stabilized by long tempering at a temperature higher than the one of the peak maximum (10 h at 525 and 4h at 600 K). The comparison of the peak P5 after annealing at 525 and 600 K is shown fig. 4.15 for five different frequencies ranging from 1 to 10 Hz. The frequencies were chosen to be equidistant in logarithmic scale.

Annealing at higher temperature leads to a decrease of the amplitude of the peak, and the peak position is shifted to higher temperature. From the peak position for the range of five different

frequencies, the activation energy and the attempt frequency of the relaxation process are determined using an Arrhenius plot (fig. 4.16). The activation energy of the peak does not change after annealing at 600 K, but the attempt frequency is found to be lower.

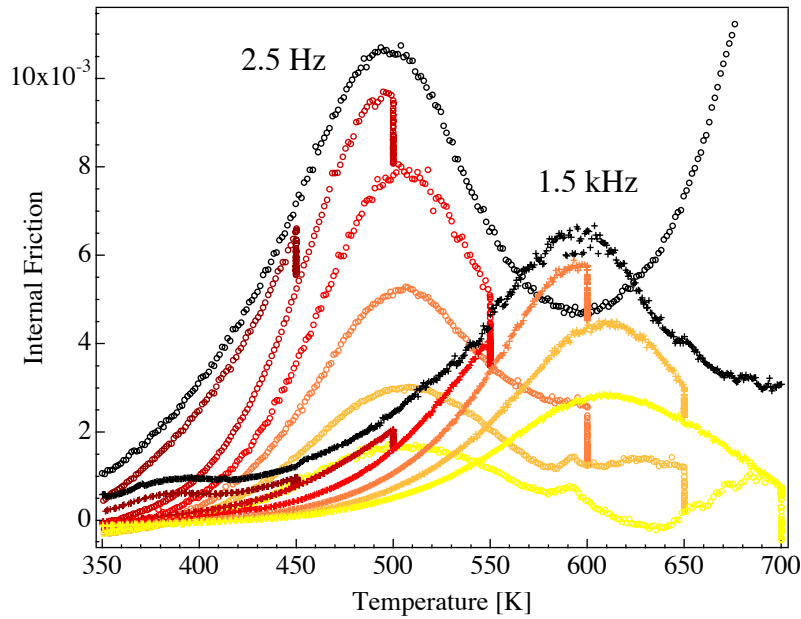


FIGURE 4.14. Comparison of IF spectra obtained in heating after successive 60 min tempering after background subtraction. The background is taken from reference spectra here shown in black (dashed line in fig. 4.2 for high and fig. 4.4 for low frequency).

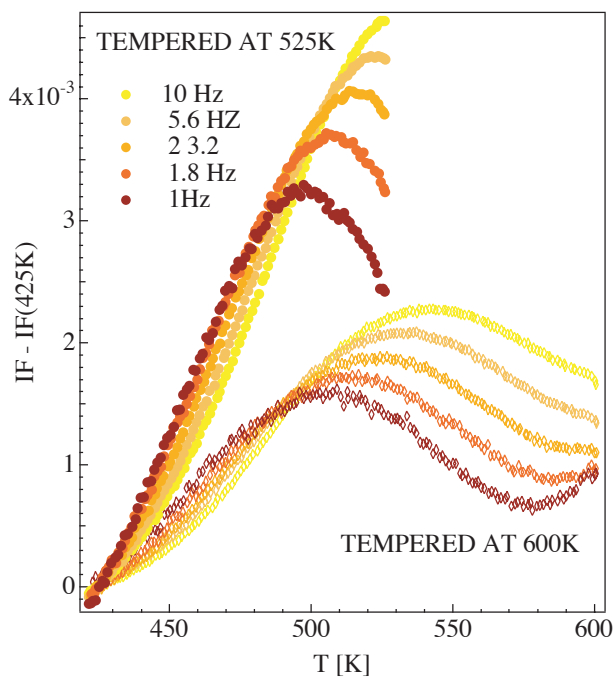


FIGURE 4.15. The peak P5 in temperature spectra obtained with a forced pendulum for different frequencies. Temperature sweeps are made after stabilizing the structure at a given temperature by a long tempering (10 h at 525 and 4h at 600 K).

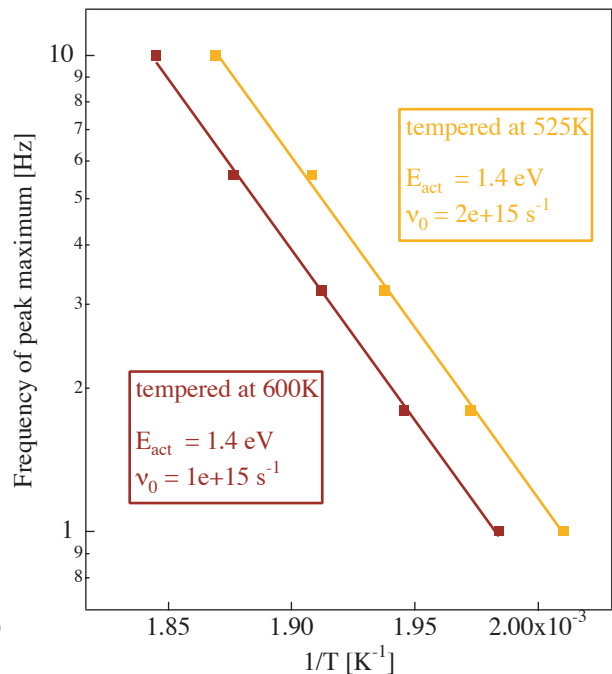


FIGURE 4.16. Arrhenius plot and activation parameters for the peak P5 after tempering at 525 and 600 K, as shown in fig. 4.15.

4.1.3 Internal friction for tempered martensitic, ferritic and bainitic structure

The rich internal friction spectrum presented above characterizes the martensitic structure. After heating of the sample up to 800 K (tempered martensite), the spectrum obtained in cooling displays only the peak P5, with the amplitude decreased by a factor 10. IF spectra for the martensitic, tempered martensitic, ferritic and bainitic structures are shown together in fig. 4.17. Ferritic samples are extracted from files that were not thermally treated. The bainitic structure is produced by quenching at intermediate temperature (720 K) after the austenitization and subsequent air cooling. The peak P5 is found in all structures, with an amplitude similarly low as in tempered martensite.

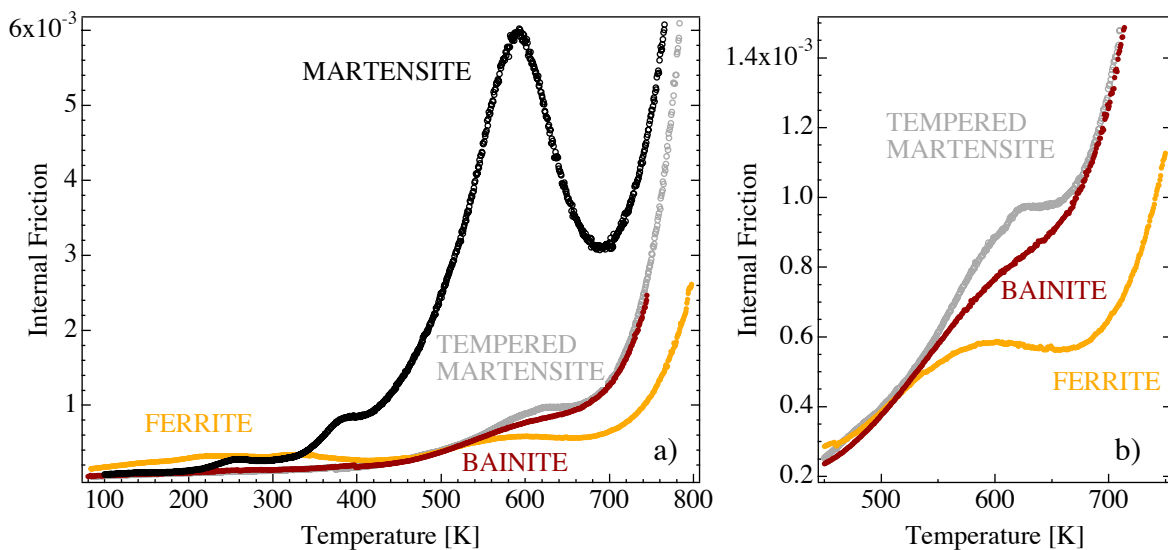


FIGURE 4.17. a) IF spectra for martensitic, ferritic and bainitic structure. The peak P5, common to all structures, is shown magnified in b). Measurements are made in the vibrating reed setup at about 1.5 kHz.

In the IF spectrum for ferritic sample, in addition to the peak P5, some peaks are visible in the low temperature region (100 - 400 K). Their origin is discussed in the following paragraph.

4.1.4 Effects of cold work on deeply tempered martensite and ferrite

Even strong cold work (40% reduction in thickness by roll milling) performed at room temperature on a sample tempered at 800 K cannot reproduce the peak P5 with the amplitude as seen in the martensite (fig. 4.18). An increase of the peak is still visible, but a much more evident effect of the cold work is a general increase of the internal friction in the whole studied temperature region.

Figure 4.19 shows the comparison of internal friction spectra up to 500 K for martensite, martensite after 1 h of tempering at 800 K, ferrite and the cold worked tempered martensite. Samples tempered at 800 K were cold worked at room temperature either by bending ($\epsilon = 0.2\%$) or roll milling ($\epsilon = 11\%$). Spectra recorded in the first heating after cooling down to 100 K show an increase of IF for cold worked samples over a broad temperature region, between 100 and 400 K. The same feature is seen in the ferritic sample, which can be considered as heavily cold worked during the file production process. The common feature in all three spectra, for cold worked martensite and ferrite, is a local minimum of IF at room temperature, separating the broad lower temperature part from a sharper peak above room temperature. Measurements per-

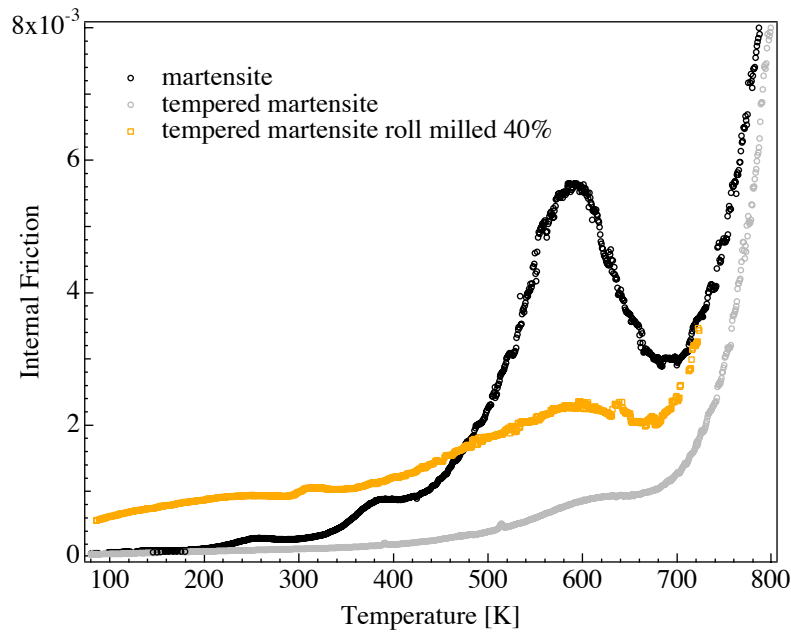


FIGURE 4.18. Effect of cold work by roll milling performed at room temperature on IF spectrum of a initially martensitic sample tempered at 800 K for 2h. The percentage of cold work is related to the thickness reduction.

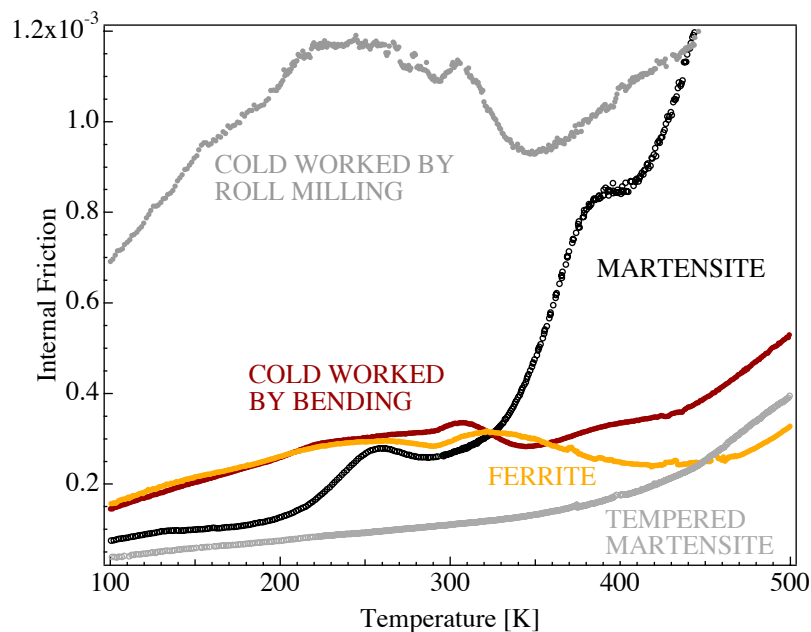


FIGURE 4.19. Effects of cold work on tempered martensite and ferrite. A broad IF peak distribution ranging from 100 K to 400 K is obtained.

formed at low frequency (1.5 Hz) in a torsion pendulum on a ferritic sample, even if scattered, show clearly that the position of the minimum does not depend on the oscillation frequency (fig. 4.20).

To clarify the origin of the local minimum appearing after cold work, experiments were performed changing the cold work temperature and the time of aging at that temperature (post-aging). The results are shown in fig. 4.21a. Without a sufficiently long post-aging after cold

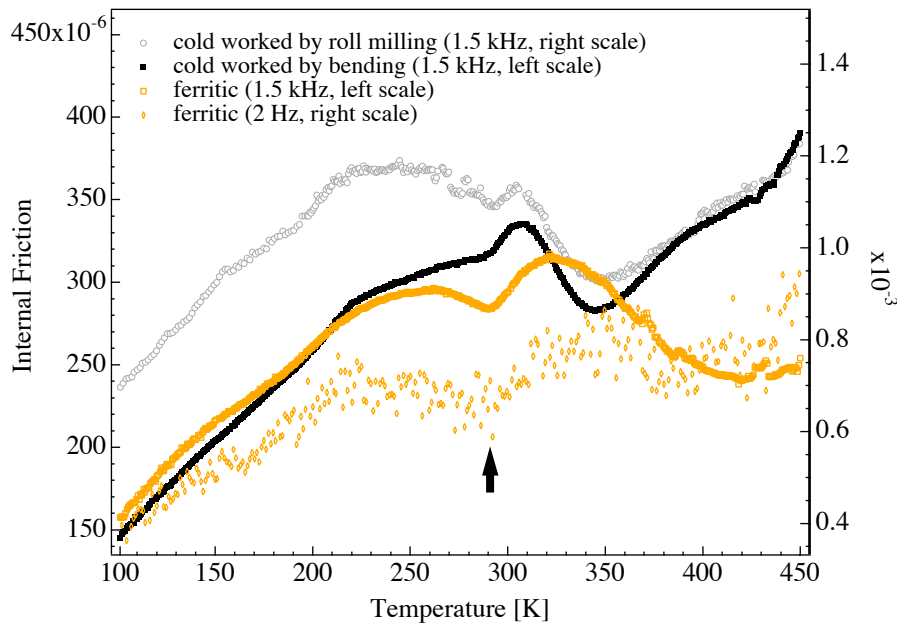


FIGURE 4.20. A dip with a minimum at room temperature (arrow) is observed at both high (1.5 kHz) and low frequency (2.5 Hz).

work (curves A and B in fig. 4.21), no minimum is observed. On the other hand, too long post-aging at 325 K leads to an important reduction of the IF and the double peak is no longer visible (curve F). A clear shift of the local minimum to the temperature of post-aging is observed for the sample cold worked and post-aged at 273 K (curve C). For the sample cold worked and post-aged for 20 h at 320 K (curve D), the minimum is shifted to 320 K, but it is much less pronounced. The curves A and D are obtained using cold worked ferritic samples. In this case, the IF does not have a steep decrease at 310 K, which is observed for cold worked tempered martensite. This enabled the observation of the IF minimum after aging the sample at 320 K that would otherwise be difficult.

The decrease of internal friction at 310 K for cold worked tempered martensite occurs together with a modulus increase (change of curvature in the frequency spectrum, fig. 4.21b). Another difference between cold worked tempered martensite and ferrite is an IF peak around 390 K that is visible only in the cold worked tempered martensite.

4.1.5 Difference between thermal treatments of files

It was shown in the previous chapter that the two types of thermal treatment, in cyanide bath (CN) and conveyor belt furnace (BF), produce a material with different mechanical properties. The difference seems linked to the concentration of carbon in solid solution as thermoelectric power measurements show a clear difference between the two types of files. This difference in TEP, that is higher values for CN files, is found to be the biggest in the bulk of the files. For that reason, the samples extracted from the bulk of the file were used for mechanical spectroscopy experiments. Some pre-tests conducted beforehand showed that the level of IF depends on the sample thickness and also on the pressure of the helium introduced as a contact gas for low temperature measurements. Therefore, some samples were planed to have the same thickness and the He pressure was strictly controlled.

The internal friction and oscillation frequency are first measured at room temperature under a vacuum better than 10^{-3} Pa. An attempt is made to determine whether there is a difference in

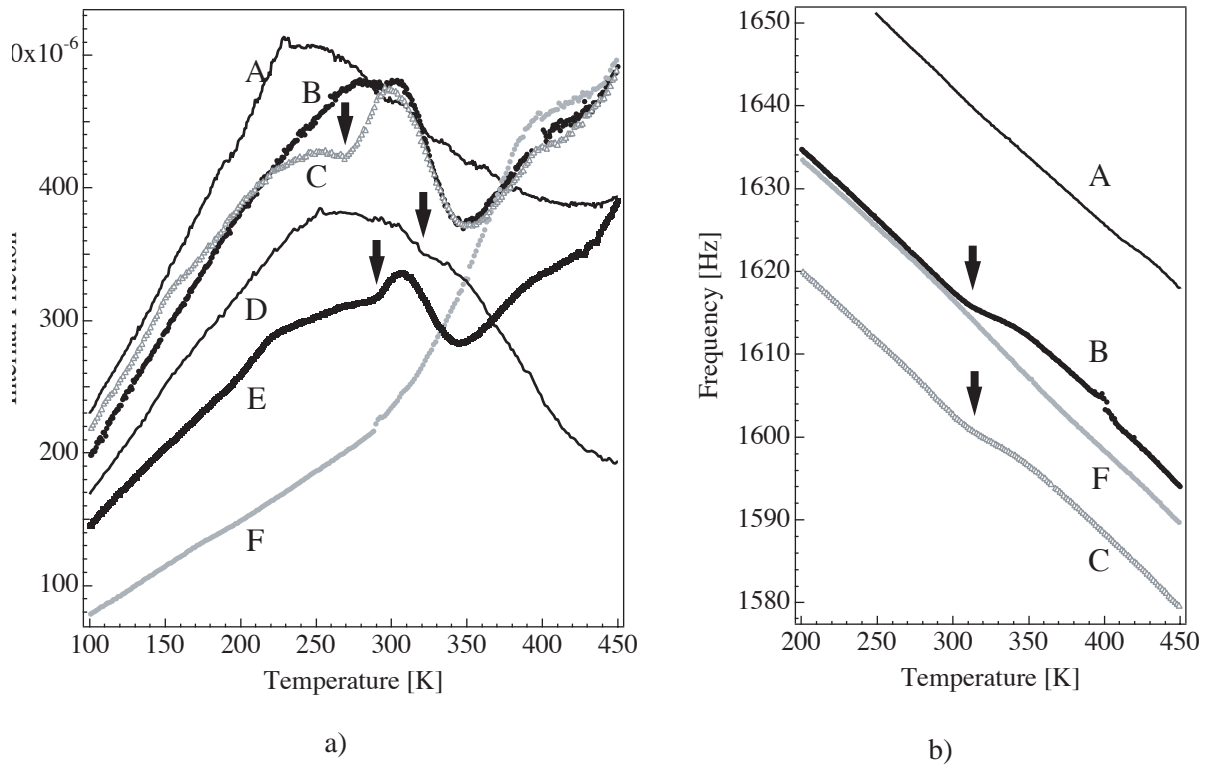


FIGURE 4.21. *a)* Time and temperature effects of cold work and post-aging on the IF minimum. Curve A and B: cold worked and post-aged for 30 min. at room temperature; C: cold worked and post-aged for 15 h at 273 K; D: cold worked and post-aged for 20 h at 320 K; E cold worked and post-aged for 8 h at room temperature; F: cold worked and post-aged for 3.5 days at 325 K. Arrows mark the positions of IF minima. Curves A and D are obtained after cold working ferritic samples, which do not show a steep decrease of IF at 310 K. *b)* Arrows mark the position of the modulus change corresponding to the steep decrease of IF at 310 K observed for curves B and C.

Young's modulus for samples extracted from CN and BF files using eq. 2.32, that can be rewritten in the form:

$$E = \left(\frac{16\sqrt{3}}{9\pi} \right)^2 \frac{f^2 \cdot m \cdot l^2}{h^3 \cdot b}. \quad (4.1)$$

The precision of the measured frequency is better than 0.05 Hz (relative error of $3 \cdot 10^{-3} \%$), but the uncertainty in dimension determination (because of the precision of the instrument as well as small variations in sample dimensions) produces an uncertainty of the calculated Young's modulus of the order of 4 GPa. This value is big enough to hide the potential difference in Young's modulus between CN and BF treated material: the average value for Young's modulus (averaged over 6 CN and 6 BF samples) is found to be 202 ± 4 GPa for both materials.

On the contrary, there is a small difference of the internal friction measured at room temperature under vacuum for different thermal treatments. The IF is higher for samples extracted from BF treated files. In addition, IF correlates with thermoelectric power (fig. 4.22).

Of course, to interpret this difference, the IF spectrum has to be examined. Two typical spectra for BF and CN samples are presented in fig. 4.23, and their difference is added on the lower scale. The difference becomes apparent only above 200 K, with the rise of the peak P2, where the BF sample starts to show a higher IF. The peak itself seems to be higher for BF samples, but the difference persists and even increases also at higher temperatures. For temperatures higher than 350 K, it is difficult to pinpoint the difference in the spectra because the measure-

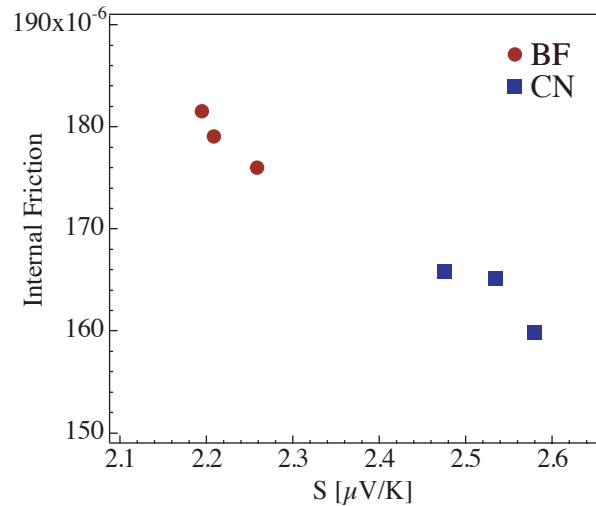


FIGURE 4.22. Internal friction vs. sample thermoelectric power, both measured at room temperature.

ment precision decreases with the increase of IF (inherent in the installation) and in addition the reproducibility of the results is not satisfactory.

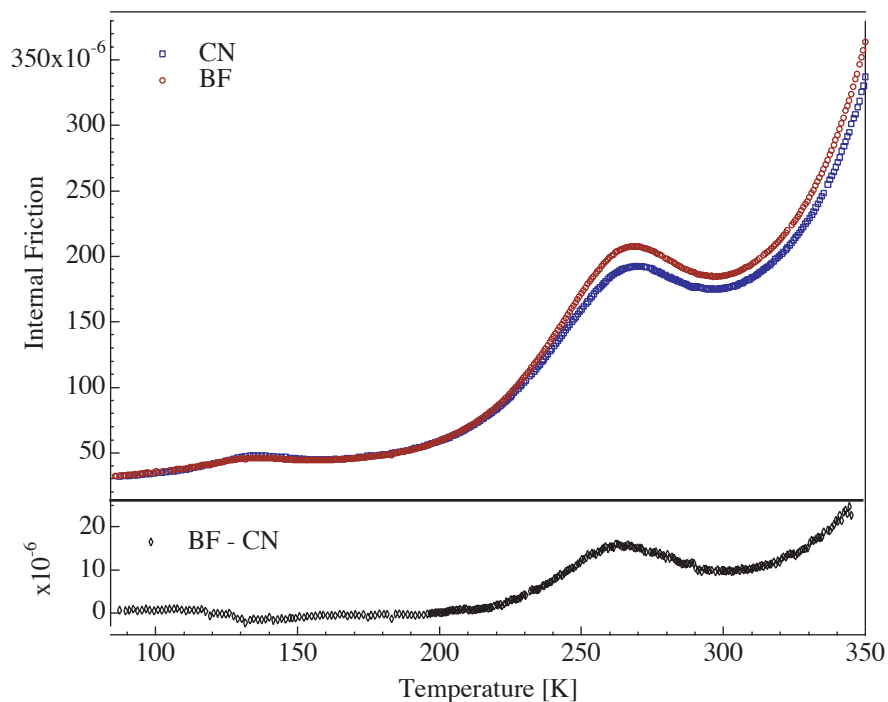


FIGURE 4.23. Internal friction spectra obtained in first heating of samples extracted from CN and BF files and their difference. Measurements are made in vibrating reed setup at about 3 kHz.

4.2 Discussion

Many overlapping phenomena seem to be responsible for the shape of the internal friction temperature spectra obtained upon heating of an initially martensitic structure. The deconvolution of the temperature spectra into Debye peaks should not in principle be used for spectra at temperatures higher than 375 K. After heating above this temperature, the IF spectrum is no longer

reproducible in cooling. One of the prerequisite conditions for the interpretation of internal friction relaxation peaks is that the material structure does not change irreversibly during the temperature sweep, and in our case it does. Thus, the peaks P3, P4, and P5 in temperature spectra should be regarded only qualitatively, keeping in mind that they are deeply influenced by the transient effects due to the kinetics of the tempering processes.

Similar arguments are valid for the calculation of relaxation parameters presented in table 4.1 for the peaks P4 and P5. The difference in frequency of three orders of magnitude between the installations should in principle lead to a rather good precision of the calculated relaxation parameters using the Arrhenius plot. There are however two influences that can significantly reduce the precision. One is experimental: the temperature reading in each installation might not be exactly the same (for example due to the distance of the thermocouple from the sample or the existence of a temperature gradient along the sample). But more importantly, the changes of the material due to tempering that starts at 375 K might influence the relaxation mechanisms. In that case, the precision of the relaxation parameters using the peak positions in such a wide temperature range might be questioned.

A more correct approach would be to study frequency spectra, after the structure has been stabilized at a certain temperature. There are, however, problems with this approach as well. Conceptually, there is no low frequency limit for a forced pendulum. In practice, the lowest frequency that can be used is 10^{-3} Hz, otherwise the measurements take a very long time and the precision is not satisfactory. Using the equation 2.27, with the relaxation parameters for P5 obtained in comparison of the temperature spectra, it is easy to calculate that at room temperature the peak P5 would have the maximum around $2 \cdot 10^{10}$ Hz which is obviously unattainable. The peak maximum at 10^{-3} Hz is at a temperature slightly higher than 400 K, but this is the temperature where tempering processes have already started, and the information about the material in the untempered state is lost. Additionally, the peak P5 is a very broad peak, and the peak fitting needs a reasonable portion at low frequency to produce a good fit. These considerations justify our analysis based on temperature spectra.

As seen from the general increase of the internal friction after cold work, the relaxation phenomena in martensite are clearly related to dislocations and to their mobility. In addition, the dislocations that move are bound to interact with point defects (namely carbon) present in the material in a large quantity.

The well known carbon diffusion peak, the Snoek peak, is not observed. It should be situated around 410 K in the kHz frequency range according to eq. 2.27 and activation energy of 0.87 eV (table 2.1). The peak P3 could be suspected to be a Snoek peak, but the comparison with low frequency spectra for which no peak is found around 320 K, where the peak is expected for 2 Hz, immediately eliminates this possibility.

The absence of the Snoek peak in martensitic samples has been documented in a review of internal friction effects in martensite by Ward [Ward 1963]. The explanation is offered considering the tetragonality of the martensite, which is maintained by the location of the carbon atoms in only one of the three available sets of octahedral interstitial sites, hence precluding the stress induced diffusion. The work of Johnson [Johnson 1965] supports this explanation showing by numerical simulation that the carbon migration energy increases with carbon content and that the strains used in the internal friction measurements are insufficient to produce the migration of the carbon atoms from their preferred interstitial sites in the bct lattice. On the other hand, the Snoek peak is found after martensite tempering at temperatures higher than 650 °C but with an amplitude much lower than in low carbon α -iron quenched from the same temperature [Stark 1956]. The lower amplitude was interpreted as due to carbon precipitation on existing carbides and grain boundaries during quenching after tempering [Stark 1958].

The absence of the Snoek peak is therefore not surprising for the martensite, but its absence in the tempered martensite or ferrite is more intriguing. It can be concluded that although some carbon is still present in solid solution (justified by the existence of the peak P5 in these structures, which is, as shown below, interpreted as Snoek-Köster carbon peak), the carbon atoms are not free to move from one type of octahedral site to the other under the applied cyclic stress. The residual tetragonality of tempered martensite could not explain the absence of the peak in ferrite. The reason why the Snoek peak is never observed could be that most of the carbon precipitates during cooling and the remaining carbon atoms are bound to dislocations or/and to other impurities.

The decrease of the Snoek peak in steels with addition of substitutionals, such as Co, Mn, Cr, Si, P and Al, has been evidenced for low impurity concentrations [Numakura 1996, Saitoh 2004, Massardier 2004]. The strain field generated by a substitutional atom due to the difference in atomic size is concluded to be the main reason for the reduction in Snoek peak height. As our steel contains 0.34 wt. % of Mn and 0.22 wt. % of Si as well as some other impurities, it is possible that they affect the carbon mobility.

If carbon atoms are bound to dislocations after tempering, they might be freed from them by cold work. It might be argued that the peak observed around 390 K in cold worked tempered martensite is a Snoek peak. However, this hypothesis is not confirmed by a modulus defect in frequency spectra nor by measurements at low frequency. Therefore it is more likely that the peak is due to a mechanism comparable to the one that causes the peak P3 in the IF spectrum of martensite.

P1

The peak P1 is observed around 130 K in the high frequency measurements and thus it may be interpreted as Snoek-Köster hydrogen peak according to literature. In previous measurements on this material [Bagramov 2001], the peak was detected also in the low frequency spectrum obtained in torsion (fig. 2.21b). From the temperature of the peak for low and high frequency (99.1 K at 1 Hz and 132.6 K at 3.1 Hz), the activation energy of the peak is calculated to be 0.27 eV, comparing reasonably well to the 0.22 ± 0.1 eV found by San Juan et al. in pure iron [San Juan 1985]. As the peak is also sensitive to cold work (fig. 2.21b), it is attributed to a relaxation of Snoek-Köster type involving non-screw dislocations and hydrogen atoms.

An interesting characteristic feature of the peak P1 is its evolution during tempering. Contrary to the behavior of other peaks, for which tempering leads to a reduction of the amplitude, the amplitude of the peak P1 is initially increased by tempering (fig. 4.12). For tempering at temperatures higher than 400 K, the amplitude of the peak decreases, and after tempering at temperatures higher than 500 K the peak disappears. The increase of the peak is also observed after aging the samples at room temperature. Moreover, the peak is hardly visible for as quenched material (fig. 4.8).

The increase of the amplitude of the peak P1 observed after tempering at 400 K could be justified by carbon precipitation. For a dragging mechanism (dislocation segments dragging point defects), the amplitude of a relaxation peak is proportional to \bar{L}^2 , the square of the average dislocation length between the strong pinning points (eq. 2.35). At the temperature of the peak P1, which is around 140 K, soluted carbon atoms can be considered as immobile and therefore playing the role of strong pinners. Precipitation of carbon in form of carbides during tempering may decrease the amount of the carbon segregated on the dislocations, therefore leading to an increase of \bar{L}^2 with a consequent increase of the peak amplitude. The position of the peak should also be influenced by \bar{L}^2 through the attempt frequency ν_0 (eq. 2.36). But, using the parameters of the peak listed in table 4.1, it can be calculated that an increase of \bar{L}^2 of 50 %

would cause a shift of the peak to higher temperature of only 3 K. The decrease of the peak by further tempering (for temperatures higher than 450 K) could be caused by a decrease of the dislocation mobility by pinning with precipitates, and for higher temperatures by a decrease of the dislocation density combined with the degassing of hydrogen from the material.

P5

The most striking feature of the IF spectrum of the martensite is the peak P5 due to its amplitude, which is notably higher than the amplitudes of the other peaks. It is also the only peak that can be found in bainitic and ferritic (tempered martensitic) structures, though having a much smaller amplitude. The peak temperature (for a given frequency) and amplitude corresponds to the Snoek-Köster peak regularly found in iron-carbon martensite and cold worked ferrite containing interstitial impurities (see for example [Ward 1963, Petarra 1967, Klems 1976]). The Snoek-Köster peak is related to the dragging of carbon atoms by kink pairs forming on screw dislocations [Seeger 1979] (see section 2.5).

The relaxation parameters of the peak can be determined by comparing the measurements in torsion and bending, which are three orders of magnitude apart in frequency. The Arrhenius plot presented in fig. 4.5 gives a value for the activation enthalpy $H = 1.8 \pm 0.1$ eV with the attempt frequency $\nu_0 = 10^{19} \text{ s}^{-1}$. The value for the activation energy fits in the range of energies measured by other authors for the Snoek-Köster relaxation peak in α -iron and carbon steel martensite of 1.4 to 1.9 eV [Klems 1976]. It can be interpreted (see page 30) as the sum of the energy for kink pair formation on screw dislocations, $2H^k = 0.94$ eV [Schultz 1991], and the energy for carbon diffusion, $H^S = 0.87$ eV (table 2.1). However, the attempt frequency is (as also found by other authors) too high to be physical. The attempt frequency for a relaxation due to point defects is expected to be of the order of the Debye frequency in a material [Nowick 1972a], i.e. of the order of 10^{13} s^{-1} , and it should be even lower for dislocation related mechanisms. The activation energy of 1.4 eV calculated from the measurements in the forced pendulum (fig. 4.16) might be considered as more precise, and the calculated attempt frequency is also closer to the Debye frequency. The measurements are performed in isothermal conditions and transitory effects are suppressed by long tempering prior to obtaining the frequency spectra. Yet, 1.4 eV is lower than expected from the theoretical model. The possible explanation is that the kink pair formation is facilitated by the presence of the strain field due to the interstitial carbon. In that case, $2H^k = 0.94$ eV obtained from the γ -peak in pure α -iron might be an overestimation.

The amplitude of the peak is much lower in the spectrum obtained with the flexural vibration technique (frequency in kHz range) than in the spectrum obtained in the inverted torsion pendulum (Hz range). The tempering experiments suggest that this is due to the position of the peak. As the peak is situated at higher temperature for higher frequency, the change of the microstructure due to tempering is more advanced, and therefore the peak is lower.

The comparison of the P5 after annealing at 525 and 600 K (fig. 4.15) reveals a shift of the peak to higher temperature and more clearly a decrease of the peak amplitude. The decrease of the amplitude of the peak is most probably related to the decrease of the dislocation density (eq. 2.35). The shift of the peak to higher temperatures has to be due to the increase of the average free length of the dislocations (\bar{L}) because an increase of the length between carbon atoms \bar{l} alone would lead to a shift of the peak to lower temperature (eq. 2.36).

P3

The peak P3 is not a relaxation peak. It is found at the same temperature in both low and high frequency spectra. This temperature corresponds to the temperature of the first stages of tempering as observed by [Van Genderen 1997] (see page 33) comprising the formation of carbon enrichments and their periodic arrangement, followed by the precipitation of carbides. The peak is created by a decrease of the IF, which is combined with an increase of the Young's modulus. In as quenched samples spectra, the decrease is even more visible (fig. 4.8). The decrease of the IF can be related to a reduced mobility of dislocations due to the pinning by precipitating carbides, and/or to a decrease of the concentration of carbon in solid solution (see "Athermal background", below).

P4

The peak P4 is the least discernible peak in the spectrum. It was necessary to introduce a peak at a temperature lower than that of P5 in fitting both high and low frequency spectra, because otherwise the fit using only four Debye peaks was not satisfactory. As the position of the peak is not well defined, the calculation of relaxation parameters is not reliable. The value of 2.2 eV for its activation energy (table 4.1) obtained from the two fits presented in figures 4.2 and 4.4 is clearly too high. The calculated activation energy of the peak P5, which is determined with more precision because the peak is well distinguished, is lower (1.8 eV), while the peak P5 appears at higher temperature in the spectrum. The value of the attempt frequency of 10^{25} s^{-1} is also non-physical.

The peak was initially [Tkalec 2002] interpreted as that observed by Klems [Klems 1976] in the same temperature region, who attributed the peak to twin boundary dragging of C atoms. Nevertheless, knowing that the IF spectrum continuously changes during heating for temperatures higher than 375 K, it is probable that the peak P4 is not a relaxation peak, as is the case with the peak P3. It is likely to be a part of the left flank of the peak P5, distorted by tempering.

P2

The peak P2 is a relaxation peak. Being sensitive to cold work [Bagramov 2001], it is clearly related to dislocation movement. Screw dislocations should become mobile at much higher temperatures, when the peak P5 is activated. Therefore, a possible interpretation of this peak is a relaxation involving non-screw dislocations or maybe kinks already existing on screw dislocations.

The formation of a local minimum in the cold worked spectra (upon aging) in the same temperature region as the peak suggests a mechanism of dislocations – point defects interaction. The fact that there was no difference in the internal friction spectra obtained after quenching succeeding austenitization under nitrogen or argon atmosphere, excludes the interstitial nitrogen as a point defect candidate. Hydrogen is supposed to be interacting with dislocations at lower temperature, and it could not be responsible for an activation energy of the order of 0.55 eV that was calculated for the peak P2. Therefore, the most probable candidate is carbon.

The dip found in the IF spectrum of cold worked tempered martensite and ferrite appears in the same temperature region as the peak P2, implying that P2 could be a pinning-depinning peak. The argument against this interpretation is the lack of dependence of the peak height on strain amplitude. Experiments performed in the forced pendulum, although with low resolution, showed no difference between the IF spectra for the strain amplitude of $5 \cdot 10^{-6}$ and $2.5 \cdot 10^{-5}$.

Also, the peak P2 cannot be a simple dragging peak involving edge dislocations and carbon. If dislocations could easily drag carbon atoms, no pinning effect could be caused by them.

We propose a model illustrated in fig. 4.24. A pipe-diffusion along the pre-existing kink (the jump of carbon atom just to the next atomic plane) would allow some motion of otherwise immobile screw dislocation. The thermal activation of the peak would be regulated by the diffusion of carbon along the edge dislocation (kink), which should be lower than 0.87 eV found for the Snoek peak, corresponding to free carbon diffusion. Therefore the measured 0.55 eV could be justified by such mechanism. The amplitude of the peak should be proportional to the dislocation density, therefore in agreement with the observed increase of the peak amplitude with cold work.

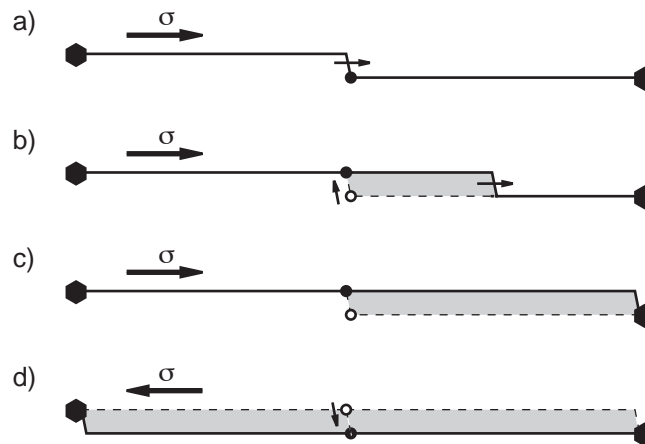


FIGURE 4.24. Proposed model for the relaxation mechanism for the peak P2, involving pre-existing kinks on screw dislocations interacting with carbon atoms. a) The movement of a kink on a screw dislocation due to the applied stress is hindered by a carbon atom (black circle). b) Under the condition that the carbon atom diffuses along the kink to the next atomic position, the kink can continue along the dislocation. c) The movement of the kink is stopped by a strong pinning point (black hexagon). d) When the stress is reversed, the same process takes place in the opposite direction.

Athermal background

The broad increase of IF between 100 and 400 K created by cold work performed on the ferritic samples, in which a dip is formed by aging (fig. 4.21), should be regarded along with the strong increase in IF, which is observed for as quenched samples following the peak P2 (fig. 4.8). They both occur in a close temperature vicinity and they probably have a related origin. The mentioned phenomena can be explained by an athermal, long distance interaction of dislocations and point defects [Bonjour 1979, Gremaud 1999].

It should be noted that the observed IF increase in as quenched samples cannot be described as a left flank of the very broadened and high peak P5, because it would require a non-physical peak broadening factor $\alpha \approx 0.1$, corresponding to the variation of the average dislocation length square over 4 orders of magnitude [Fuoss 1941]. In addition, the high soluted carbon content, which is expected after quenching, would lead to a shift of the peak P5 to even higher temperatures. At least qualitatively, the existence of an internal friction athermal background explains better the observed IF behavior.

The moving dislocations can interact with obstacles lying in their gliding plane, but there is also a weaker elastic interaction with defects situated in the bulk of the crystal at different distances from the gliding plane (fig. 4.25). The dislocations can overcome short-range obstacles under the combined action of applied stress and thermal energy, while relatively weak long-range obstacles are surmounted athermally. The first process produces the relaxation peaks, and the second one is responsible for an athermal background [Gremaud 1999].

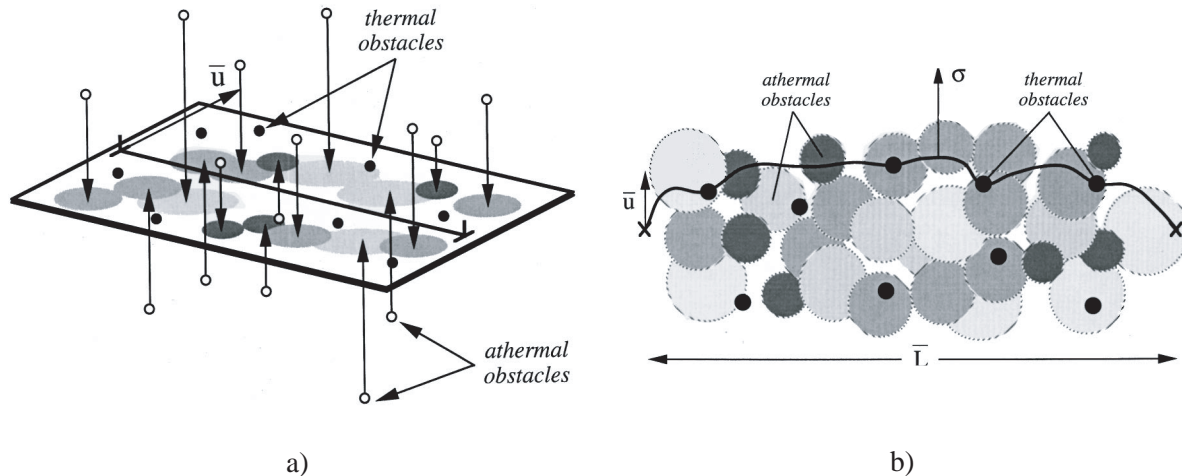


FIGURE 4.25. a) Schematic representation of a dislocation gliding in the stress fields of solute atoms. Small full circles represent solute atoms in or adjacent to the glide plane. Open circles show solute atoms, situated away from the dislocation glide plane. Large gray symbols on the glide plane represent long-range athermal stress fields due to these atoms. b) Model for the dislocation motion with an average displacement \bar{u} . Crosses represent strong pinning points defining the free length of the dislocation \bar{L} . Taken from [Gremaud 1999].

The magnitude of the IF background has a complex dependence on the concentration of defects and the average dislocation length \bar{L} (fig. 4.26), strain amplitude and temperature (fig. 4.27). Figure 4.27 shows that, for a given fixed strain amplitude (sufficiently high), the IF increases with increasing temperature. This is exactly the behavior that is observed for as quenched martensite in the temperature region below 300 K (fig. 4.8 and 4.9).

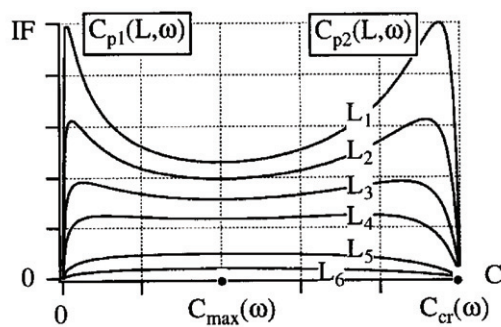


FIGURE 4.26. Numerical modeling of internal friction background for different values of \bar{L} ($\bar{L}_1 > \bar{L}_2 > \dots > \bar{L}_6$) and point defect concentration [Gremaud 2001].

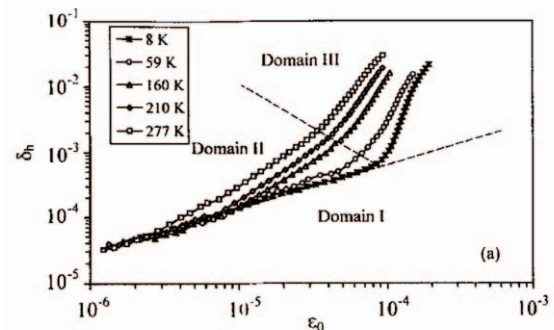


FIGURE 4.27. Strain amplitude dependence of IF in Cu-7.6 at.% Ni [Kustov 1999]. For a given fixed strain (sufficiently high), the IF increases with temperature.

The increase of the IF following the peak P2 is highest for the as quenched material (fig. 4.8 and 4.9). Shortly after quenching, the thermopower of the material is very low (fig. 3.16), implying a high concentration of soluted carbon. With aging, the TEP increases, due to pre-precipitation processes such as carbon segregation to dislocations and clustering. Correspondingly, the IF increase is reduced after aging.

The simulation of the IF dependence on the point defect concentration shown in fig. 4.26 for different dislocation lengths \bar{L} (between strong pinning points) is made with arbitrary values of the model parameters, but it describes well the behavior experimentally observed [Bonjour 1979]. Under appropriate conditions, for example high but not critical concentration of defects

and sufficiently long average free dislocation length, the background can be proportional to the defects concentration.

The proportionality of the athermal internal friction to the concentration of carbon can explain why the increase of IF is highest in as quenched martensite and why it is reduced upon aging at room temperature. The decrease of the IF, observed at 300 K in spectra for freshly quenched martensite, could be due to the beginning or to the resumption (for shortly aged samples) of the carbon pre-precipitation processes that reduce the concentration of carbon in solid solution.

The difference of internal friction spectra for samples extracted from BF and CN treated files can also be explained by the existence of the athermal background proportional to carbon concentration. The difference curve of the two spectra, $IF(BF) - IF(CN)$, presented in fig. 4.23 shows a peak at the same position as the peak P2. Therefore, the peak P2 seems slightly higher for the BF treated material. However, the difference curve increase following this peak can be related to the athermal background. The background is higher for BF than for CN samples, consistently with the results of the TEP measurements. Lower TEP measured for BF files implies a higher concentration of carbon in solid solution, producing a higher athermal background. The athermal background can be considered as a major contribution to the internal friction measured at room temperature. Therefore, the inverse proportionality between IF and thermoelectric power measured at room temperature presented in fig. 4.22 is related to the opposite sensitivity to carbon content.

Although the estimated concentration of 0.5 wt.% carbon in solid solution in the martensitic matrix may not seem to be too high, it gives an average distance between carbon atoms of 0.8 nm, corresponding to the distance of only 2.8 martensite unit cells. An interaction between dislocations and carbon atoms present around them is thus very likely.

Cold work effects are interpreted as follows. Upon cold work, dislocations break away from the pinning points issued from tempering and simultaneously new dislocations are created. Carbon atoms are released from dislocations and some dissolution of small carbides is also possible. The result is the formation of a very broad IF increase, due to the wide distribution of free dislocation lengths (related to the peaks P1 and P2), superimposed on a high athermal background.

For the formation of the local minimum upon aging, we suggest a mechanism of dislocations – point defects interaction. During aging after cold work, an atmosphere of point defects (probably carbon) is formed around the dislocations relaxing the elastic strains due to dislocations and also reducing their mobility. The dislocations can move away from the pinning atmosphere upon cooling, due to the internal stresses that change with temperature. As they pass back through their initial positions during heating, their mobility is first reduced by the carbon atmosphere creating a local minimum. On increasing the temperature, they can break away from carbon atoms and/or drag them causing the abrupt increase of the IF. A similar effect was observed by Vincent [Vincent 1973] in ultrasonic attenuation in aluminium submitted to an external stress after aging. The effect is smaller for the ferritic sample cold worked and post aged at 320 K. In this case, weaker pinning points like carbon interstitials or clusters are already very mobile at the temperature where the dip should appear and the effect is decreased.

The decrease of the internal friction around 310 K for cold worked tempered martensite (fig. 4.21) is most probably transient in nature, because it is accompanied by a modulus increase. Indeed, for the sample that was post aged for 3.5 days at 325 K (curve F in fig. 4.21), all features in the IF spectrum below that temperature, which are observed for samples aged at 273 K and RT, are missing. This effect is however related to a particular state of tempered martensite as it is not observed in ferrite.

High temperature background

At relatively high temperatures, the damping curve of most materials rises continuously to very large values of internal friction. This background is found to be higher in polycrystalline materials than in single crystals, and it is higher for finer grain size. Therefore it is apparently related to grain boundary mechanisms [Nowick 1972a].

The internal friction spectra were not studied in detail for temperatures higher than 800 K. The first reason is purely practical: 800 K is the upper temperature limit of the installations used. But a more important reason is that the martensitic structure, which is the main object of this work, undergoes major changes already at 500 K. Therefore the study of the high temperature behavior is out of the scope of this work. Some purely qualitative observations should be however mentioned.

The IF background that is observed following the peak P5 is much higher for low than for high frequency measurements (fig. 4.10), therefore implying a thermally activated relaxation mechanism. The background decreases after 1 h tempering at 800 K indicating that the structure is not stable. Finally, the background following the peak P5 for the ferritic structure is found to be significantly lower than the one for tempered martensite and bainite (fig. 4.17). The microstructure of ferrite is much coarser (confirmed by TEM imaging), which supports the hypothesis that the background is grain boundary related.

4.3 Conclusions

The martensitic structure is characterized and distinguished by a rich internal friction spectrum composed of several overlapping relaxation and transition phenomena. The relaxation mechanisms are related to the interaction of dislocations and point defects and their mobility.

The peak P1 is interpreted as Snoek-Köster hydrogen peak. A mechanism is proposed for the peak P2, involving pipe-diffusion along kinks on screw dislocations. The tempering processes (for aged material) start upon heating over 375 K, causing a decrease of the internal friction and an increase of the Young's modulus. Thus peaks P3 and most likely P4 are not relaxation peaks, but products of these tempering effects. The peak P5 is interpreted as a Snoek-Köster carbon peak. The increase of the IF observed for as quenched samples is attributed to an athermal background proportional to the amount of carbon in solid solution. This mechanism is also responsible for the difference in IF between CN and BF treated material.

The spectra obtained by mechanical spectroscopy show that the material continuously changes due to the tempering. Therefore, tempering effects will be studied in more details in the following chapter.

In the previous chapter, it was shown that for temperatures higher than 375 K the internal friction and the elastic modulus change both as a function of temperature and time. Those changes reflect the evolution of the material microstructure due to the tempering as observed by TEM. In this chapter, the effects of tempering are described combining mechanical spectroscopy, differential scanning calorimetry (DSC), nanoindentation and measurements of thermoelectric power (TEP).

5.1 Differential scanning calorimetry

The typical thermogram obtained by differential scanning calorimetry (with sample mass 0.116 g and heating rate 1 K/min) is presented in fig. 5.1. It shows two peaks, one starting at 365 ± 5 K with the maximum at 400 ± 5 K, and the other one starting at 455 ± 5 K with the maximum at 517 ± 2 K. The shift of the second peak in the DSC thermogram due to the different heating rates (fig. 5.2) gives an activation energy of 1 eV according to eq. 2.39.

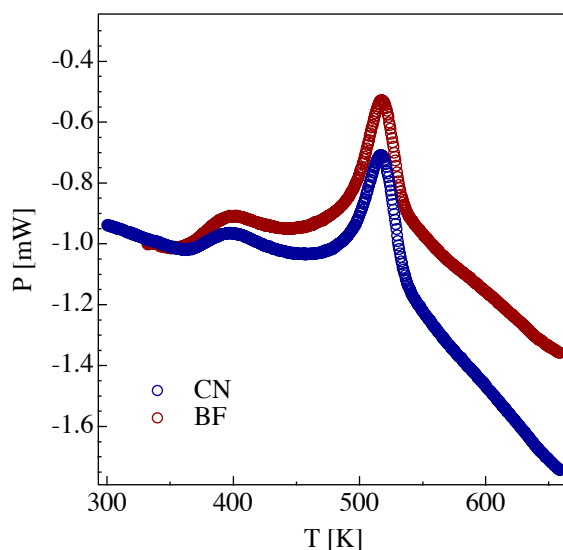


FIGURE 5.1. DSC thermogram obtained with a heating rate of 1 K/min.

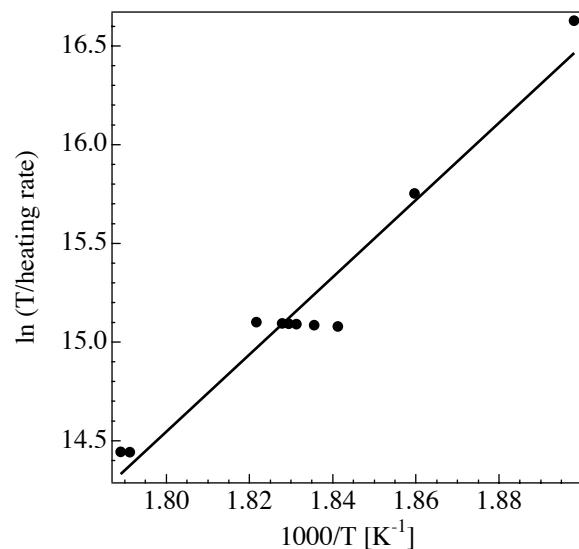


FIGURE 5.2. Shift of the second peak in the DSC thermogram due to the heating rate.

5.2 Transmission electron microscopy

Three temperatures are chosen for tempering before TEM observations, based on the features in the internal friction spectra. The first temperature is 450 K, which was chosen as intermediate stage between the peaks P3, which marks the beginning of the tempering process, and P5, where dislocations are highly mobile. The second is 600 K, after which the peak P5 diminishes. Finally, 800 K was chosen as the temperature after which all of the IF peaks disappear. Tempering is carried out for 60 h at 450 K, 9 h at 600 K and 10 h at 800 K under a vacuum better than 10^{-4} Pa.

Tempering at 450 K

Although tempering at 375 K has a major effect on internal friction and, as it will be shown in this chapter, all other measured quantities, even a long tempering at 450 K does not produce changes of the microstructure visible at first glance. The structure is still martensitic, and both plate (fig. 5.3) and lath martensite (fig. 5.4) are visible. However, higher magnification reveals the decoration of dislocations with nanosized carbides (fig. 5.5). From their diffraction pattern, they are identified as metastable orthorhombic η -carbides [Han 2001].

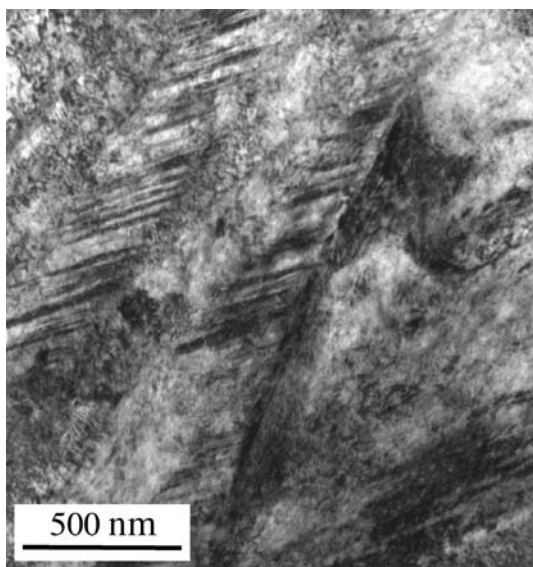


FIGURE 5.3. The twinned plate martensite structure is still visible in the matrix even after 60 h tempering at 450 K.

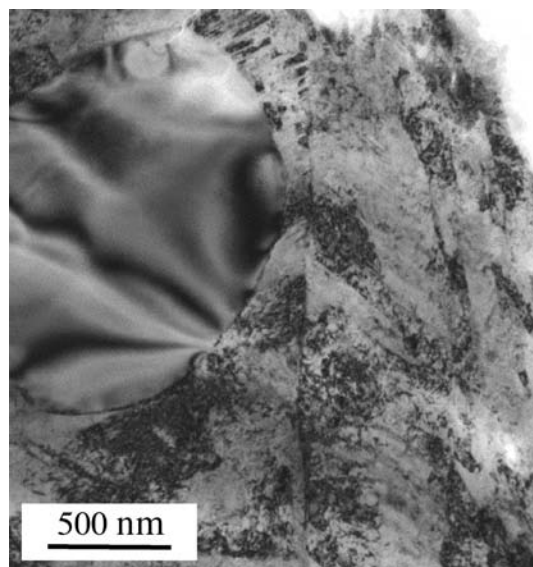


FIGURE 5.4. Lath martensite after 60 h tempering at 450 K. It shows no noticeable difference when compared to the non-tempered material.

Tempering at 600 K

Contrary to tempering at 450 K, after tempering at 600 K the microstructure is notably changed. The characteristic martensitic structure disappears: the matrix is transformed into ferrite (fig. 5.7) with cementite precipitates between certain laths (fig. 5.8). The dislocation density is decreased, and the dislocations are pinned by nanometer sized carbides (fig. 5.9).

Tempering at 800 K

A temperature of 800 K is sufficient for full recrystallization. The microstructure after tempering consists of equiaxed ferritic grains comparable in size with the carbides (fig. 5.10). Cementite precipitates, formed during tempering, are visible at grain boundaries, mostly triple points, and even within the grains (fig. 5.11). During the recrystallization, the dislocation

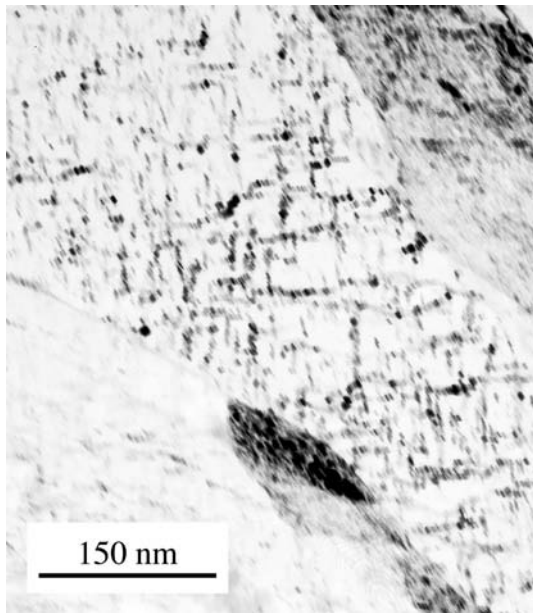


FIGURE 5.5. Decoration of dislocations with nanosized η -carbides after tempering at 459 K.

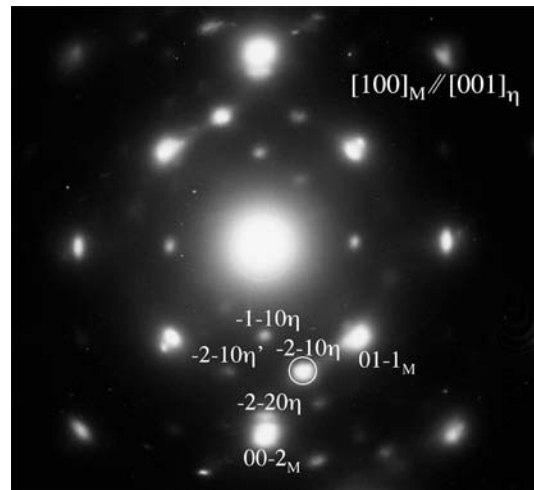


FIGURE 5.6. Diffraction pattern of η -carbides.

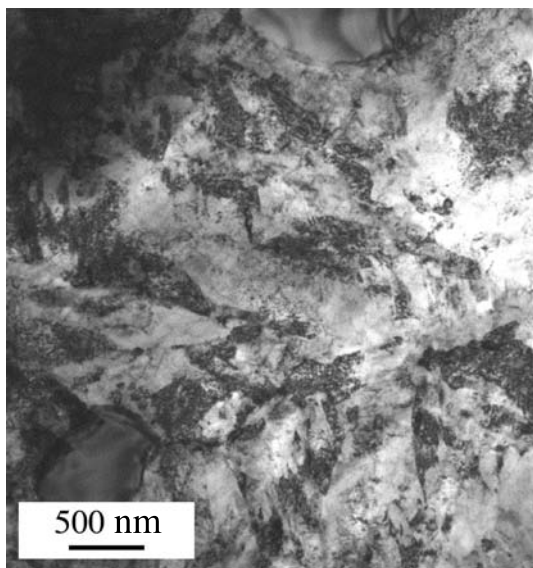


FIGURE 5.7. After 9h at 600 K, the microstructure is visibly changed, the martensite is transformed into ferrite.

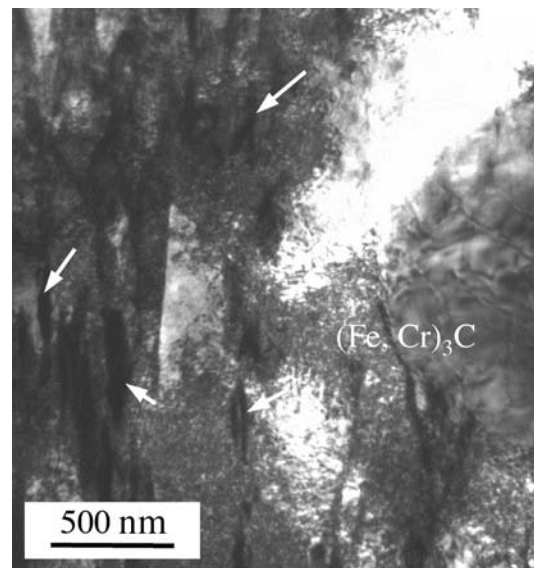


FIGURE 5.8. Cementite precipitation after 9h at 600 K is visible between prior martensite laths (arrows).

density is substantially reduced. Mixed dislocations that remain are long (50 - 200 nm) and pinned by carbides (fig. 5.12).

5.3 Thermoelectric power

To be able to relate the thermoelectric power evolution with the measurements of internal friction performed at a constant heating rate of 1 K/min, the measurements of TEP were performed at room temperature after 25 min of successive tempering in steps of 25 K. The room

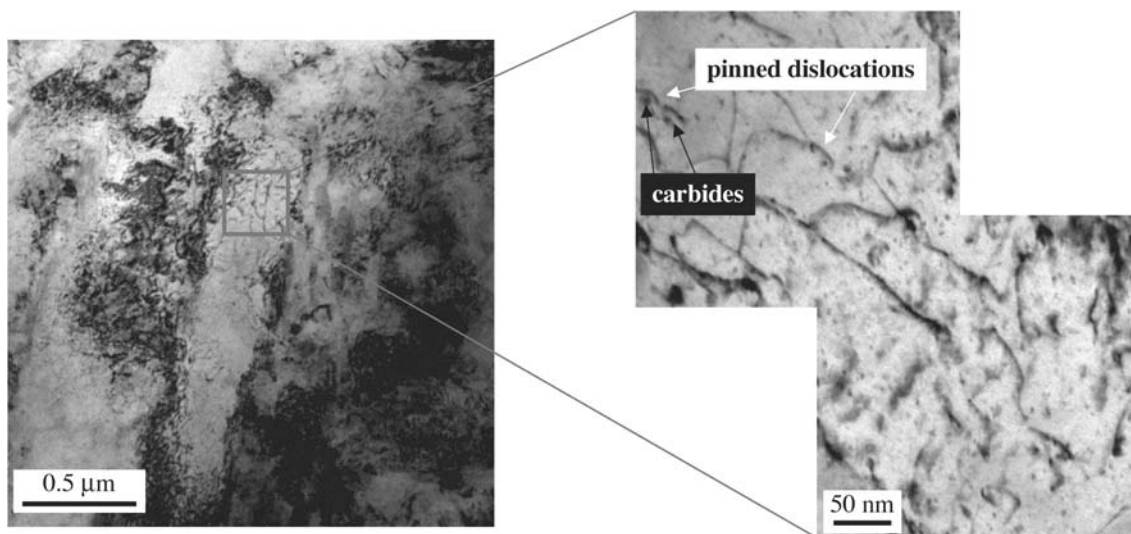


FIGURE 5.9. The dislocation density is decreased by 9h tempering at 600 K, and dislocations are pinned by nanometer size carbides.

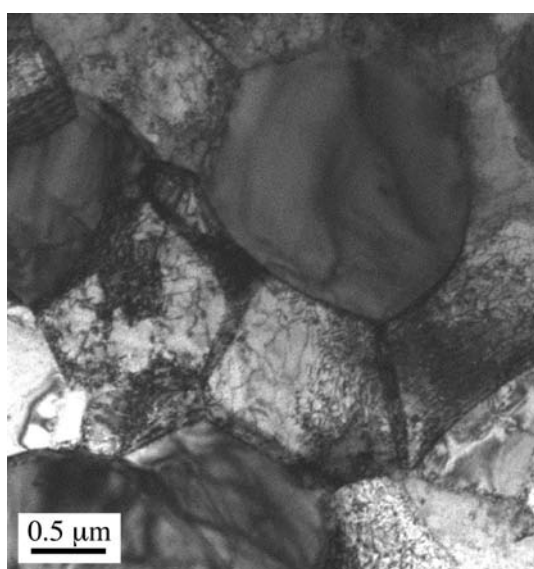


FIGURE 5.10. Recrystallization of the material after 10h at 800 K. The ferrite grains are spheroidal and comparable in size with cementite.

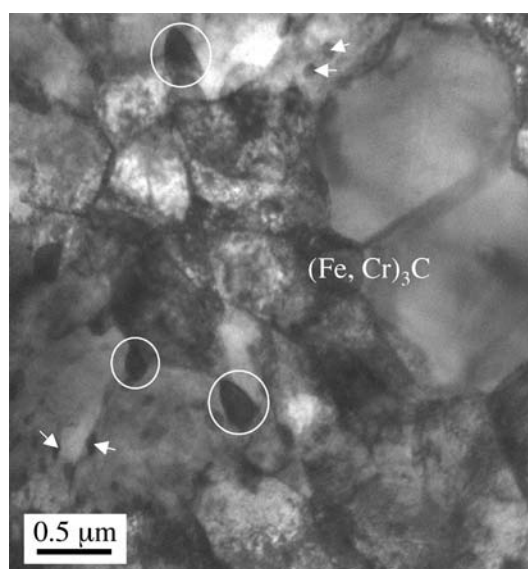


FIGURE 5.11. Cementite precipitates formed during tempering are visible at grain triple points (circles) and sometimes even within the grains (arrows).

temperature TEP is presented in fig. 5.13a as a function of the tempering temperature. No change of the TEP is observed after tempering at 325 and 350 K and the first increase is seen upon tempering at 375 K. The TEP continues to increase with further tempering. The starting difference between the samples that are extracted from files that underwent different thermal treatment becomes visibly smaller after tempering at 400 K and can be considered as within experimental error after tempering at 525 K.

The increase of TEP after tempering is not monotonic. The triangles in fig. 5.13b show the change in TEP between successive tempering steps, which corresponds to its first derivative. It exhibits two distinctive maxima, one around 390 K and the other around 510 K. The two maxima occur at temperatures close to those observed in the DSC thermogram, marking two stages of tempering.

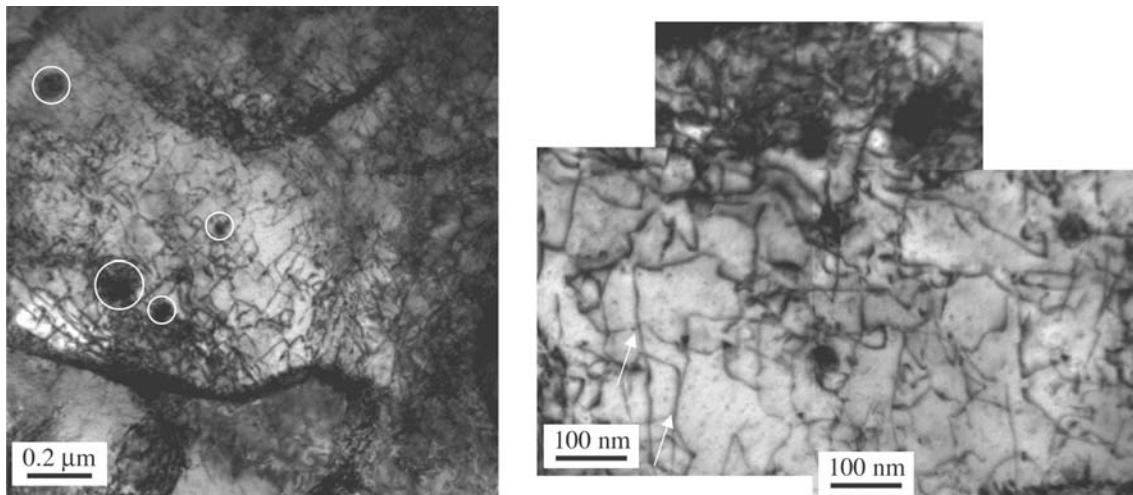


FIGURE 5.12. During the recrystallization, the dislocation density is substantially reduced. Mixed dislocations that remain are long (50 - 200 nm) and pinned by carbides (circles and arrows).

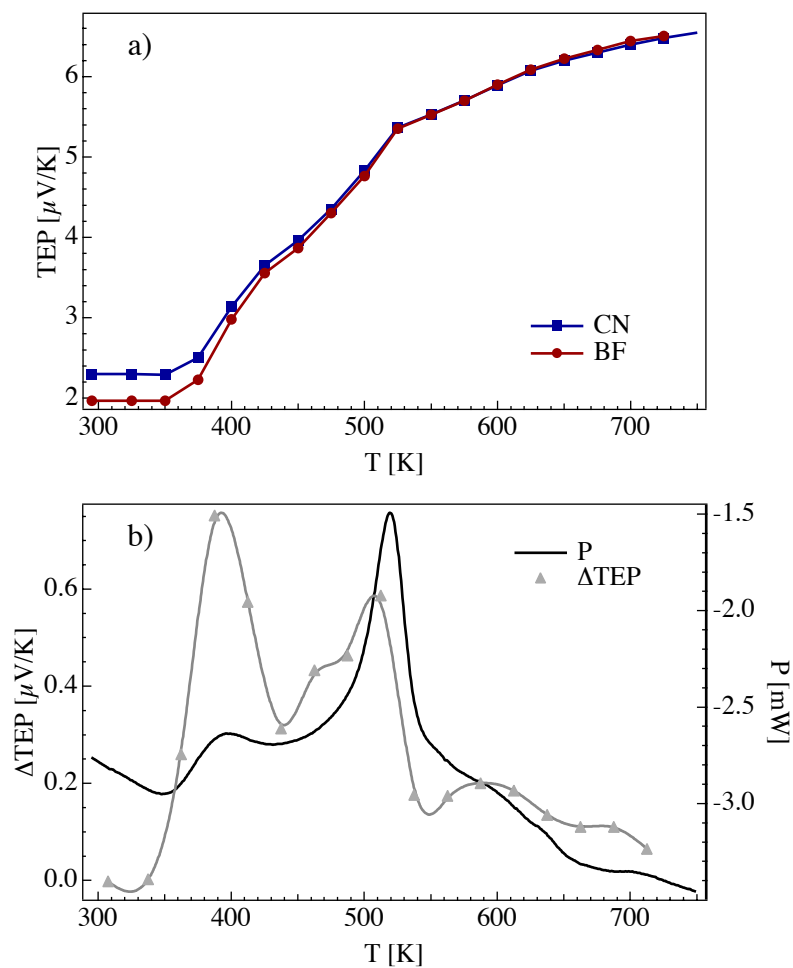


FIGURE 5.13. a) Room temperature TEP measured after 25 min of successive tempering as a function of tempering temperature. b) Relative change of room temperature TEP between two consecutive tempering steps (triangles) compared with a characteristic calorimetry spectrum measured at a heating rate of 1 K/min (line).

5.4 Internal friction

As presented in the previous chapter, the internal friction spectrum of the as received material, obtained in heating to temperatures higher than 375 K, is not reproducible in cooling. The peak P3 and most probably P4 reflect a decrease of the IF due to tempering processes. The decrease of the peak P5 is also observed after tempering at temperatures higher than the temperature of the peak.

The interest of studying the internal friction at room temperature, as a function of tempering at higher temperatures, lies in the possibility to compare the IF with TEP measurements. Moreover, it is at room temperature that IF spectra differ for samples extracted from differently heat treated files.

The internal friction of a BF sample measured at room temperature after successive 25 min tempering in steps of 25 K (exactly as in TEP measurements, section 5.3) is presented in fig. 5.14. The IF starts to decrease after tempering at 375 K showing a similar trend as the increase of the TEP (fig. 5.13): the change is very strong after tempering at 400 K, and the value tends to saturate after tempering at higher temperatures. However, the second tempering stage around 510 K is not especially reflected in the IF evolution.

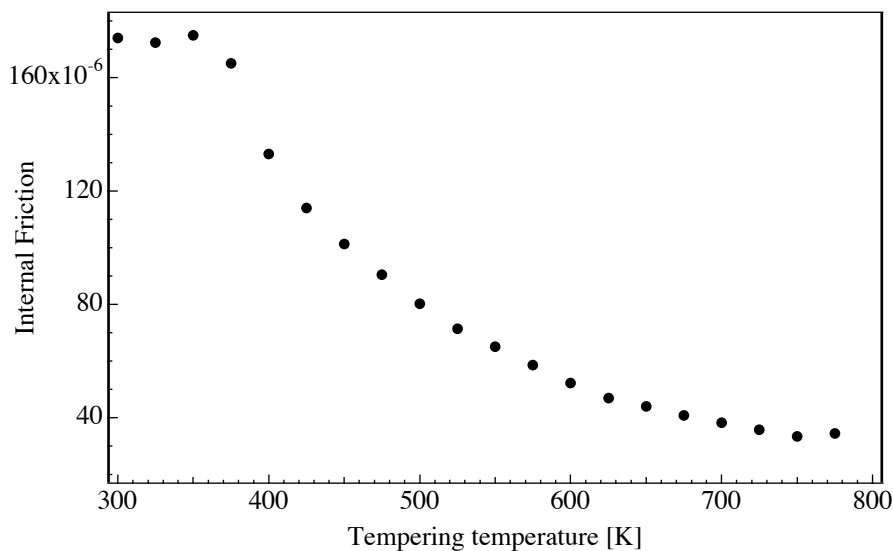


FIGURE 5.14. Internal friction measured at room temperature after successive 25 min tempering steps as a function of tempering temperature

5.5 Young's modulus

The Young's modulus is calculated from the frequency measured at 300 K in the vibrating reed installation, using eq. 4.1. The evolution of Young's modulus, as a function of tempering temperature is shown in fig. 5.15. The first increase is observed after tempering at 400 K. From this point on, it increases almost linearly until the tempering at 525 K. For tempering at higher temperatures the increase is still linear but with a less steep slope. No saturation comparable to the one observed in TEP and IF is observed up to the temperature of 800 K.

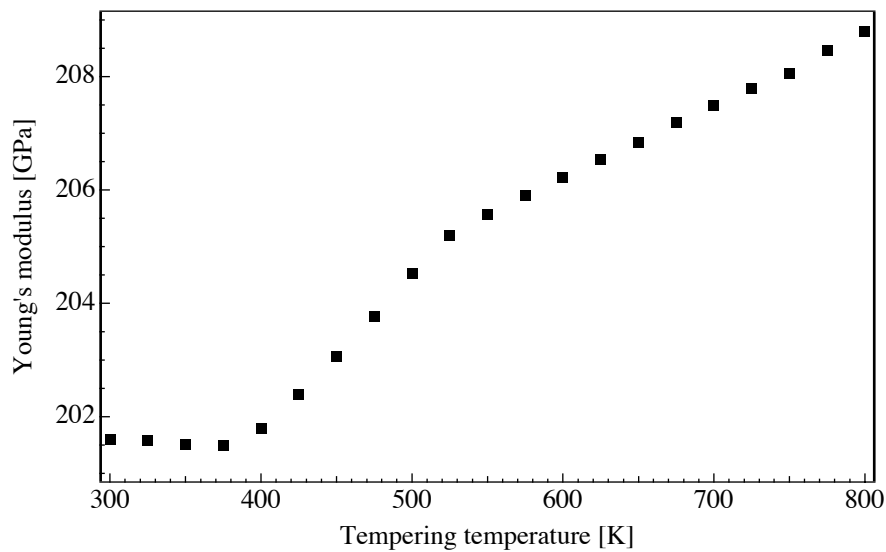


FIGURE 5.15. Young's modulus measured at room temperature after successive 25 min tempering steps as a function of tempering temperature.

5.6 Nanoindentation

Figure 5.16 shows the nanoindentation hardness, measured for a BF sample aged at room temperature for 8.5 months, as a function of tempering temperature. The measurements are performed at room temperature, following the same tempering procedure as already described. Each point is obtained by averaging the hardness at the indent depth between 1000 – 1200 nm and then from four indents for each tempering temperature for statistical purposes.

Within the precision of the measurements, the hardness does not change substantially for tempering below 400 K and then decreases almost linearly for tempering at higher temperatures.

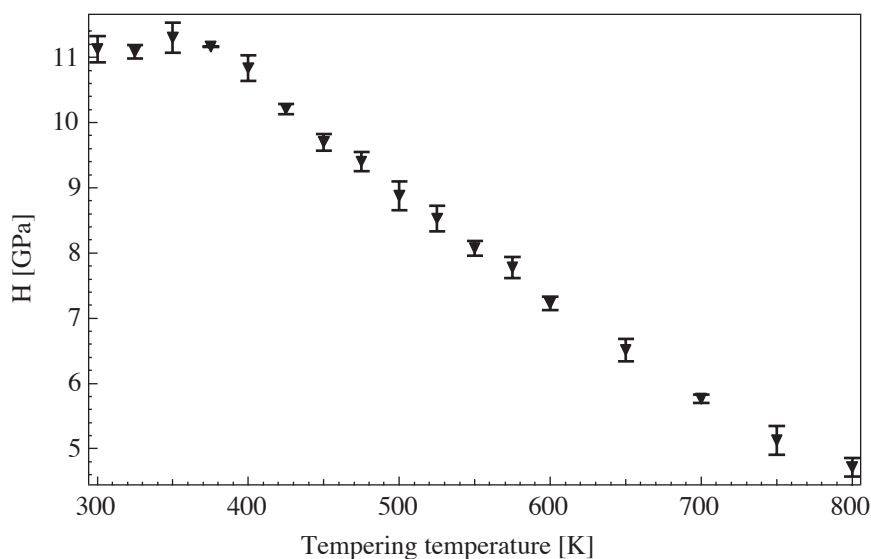


FIGURE 5.16. Room temperature hardness measured after 25 min of successive tempering steps as a function of tempering temperature.

5.7 Discussion

Two transformation stages seem to be indicated by DSC measurements. Qualitatively, the DSC thermogram resembles very much the ones obtained in Fe-C martensites by other authors [Mittemeijer 1991, Van Genderen 1997, Han 2001]. The differences come from the fact that they measured as-quenched martensite, while the material studied here has been considerably aged at room temperature. For that reason, no special pre-precipitation stage is observed prior to the appearance of the first peak starting at 365 ± 5 K. According to [Van Genderen 1997], this peak is related to a periodic arrangement of carbon enrichments followed by ϵ/η -carbide precipitation.

The formation of η -transition carbides is confirmed by our TEM observations (figures 5.5 and 5.6). The carbides are found on the dislocations, which confirms the interpretation of the peak P3 in the internal friction spectra as an IF decrease due to dislocation pinning.

The second peak in the DSC thermogram is attributed in literature to the decomposition of residual austenite, but several reasons indicate that it could be attributed to a precipitation process (formation of cementite) in addition to a transformation from γ to α -iron. First, residual austenite is present in our structure in a very small quantity (1%) according to TEM observations, and second, no peak is observed in that temperature region in the internal friction spectra, even though internal friction is especially sensitive to phase transformations. Another argument is that a shift of the DSC peak is observed when changing the heating rate (fig. 5.2), which gives an activation energy of 1 eV according to eq. 2.39 [Mittemeijer 1992]. This activation energy corresponds well to that of carbon diffusion.

As discussed in Chapter 3, the thermoelectric power is very sensitive to the state of the microstructure of the material. It is shown to vary inversely with the amount of carbon in solid solution, and also to a smaller extent with the density of dislocations. The two peaks observed in the change of TEP that match in temperature those in the DSC spectrum could be interpreted as two stages of carbon precipitation from the matrix.

The first stage of tempering is clearly observed also as the beginning of the decrease of internal friction and hardness measured by nanoindentation, and as an increase of Young's modulus, between 375 and 400 K. This tempering stage is related to carbon precipitation in the form of transition carbides. Therefore, it can be concluded that all measured quantities depend to some extent on the concentration of carbon in solid solution. However, further evolution of the measured quantities with tempering follows different trends. This implies that, in addition to the sensitivity to interstitial carbon, the TEP, IF, hardness and Young's modulus have a different sensitivity to other mechanisms.

The calculation of the Young's modulus from the measured frequency is burdened mostly by the lack of precision in sample dimensions, because the precision of the frequency measurements is of the order of $2 \cdot 10^{-2}$ %, mostly due to the temperature stabilization. Moreover, interstitial carbon causing the tetragonality of the martensitic matrix precipitates with tempering, and this leads to the change of structure from martensitic to ferritic, resulting in a volume decrease. As the sample dimensions change, so does the oscillation frequency, additionally to the change due to the variation of the modulus.

The dilatometry measurements [Mittemeijer 1991] of a steel containing 1.1 wt.% C reveal a sequence of structural changes that occur with tempering (fig. 5.17). A detailed quantitative discussion of tempering phenomena is presented in [Cheng 1988]. A correspondence was found between the DSC thermogram and the derivative of the sample relative length, similar to

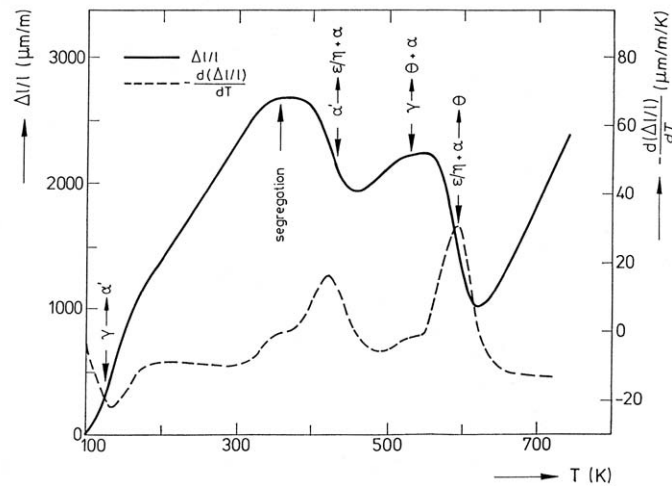


FIGURE 5.17. Relative length $\Delta l/l$ and its derivative $d(\Delta l/l)/dT$ [Mittemeijer 1991]. The derivative shows two peaks corresponding in temperature to those observed in DSC spectra.

the correspondence between the derivative of TEP and the DSC thermogram presented in (fig. 5.13).

A small length increase is associated with the transformation of residual austenite, but this effect is small compared to the length decrease due to the precipitation of carbon in a form of transition carbides during the first tempering stage, and in form of cementite during the second tempering stage. These two processes form peaks in the derivative.

For our steel, the relative sample length decrease after tempering at 800 K, as compared to room temperature length, is smaller than 0.2 %. Presuming that the change of volume is isotropic, i.e. that:

$$\frac{\Delta l}{l} = \frac{\Delta h}{h} = \frac{\Delta b}{b} = \frac{\Delta V}{3V}, \quad (5.1)$$

the calculated correction for the Young's modulus with respect to the one calculated with the initial dimensions (results presented in fig. 5.15) for the extreme case, 800 K, is only 0.4 GPa. When compared to the total change of Young's modulus between 300 and 800 K, which is more than 7 GPa, it is clear that the correction due to the change of the sample dimensions cannot influence the general behavior of the curve nor the interpretation.

Young's modulus is, similarly to TEP, inversely proportional to the amount of carbon in solid solution ([Schmidtman 1965, Speich 1972b, Speich 1973]) and dislocation density [Ghosh 2002]. A precise quantitative analysis of the influence of the amount of carbon in solid solution in the evolution of the Young's modulus is not possible because of the unquantifiable influence of the dislocation density and the lack of precise knowledge about the influence of embedded carbides. We offer an approximative numerical analysis based on Eshelby's method [Eshelby 1957, Clyne 1993] for calculating the Young's modulus of the composite using an isotropic approximation for the calculation of the elastic tensors, in order to estimate the Young's modulus of the martensitic matrix.

The initial $(\text{Fe, Cr})_3\text{C}$ carbides contain 0.22 ± 0.03 % Cr with respect to Fe [Bagramov 2001]. A Young's modulus of 245 GPa can be estimated for the chemical composition of these carbides according to a recent study by [Umamoto 2001]. The measured Young's modulus of 202 GPa for the untempered material includes the contribution of the cementite carbides as well as the contribution of the matrix. We consider, according to Eshelby, the cementite inclusions inside a

martensitic matrix. Taking the Young's moduli of the spherical inclusion and of the composite, 245 GPa and 202 GPa respectively, and the Poisson ratios $\nu = 0.28$ [Speich 1972a] for both the carbides and the matrix, we obtain 197 GPa as a result for the Young's modulus of the martensitic matrix.

The saturation of the TEP indicates that the carbon in solid solution tends to the limit of carbon solubility in α -iron after tempering at temperatures higher than 800 K. Thus, most of the total 1.23 wt.% carbon present in the material forms cementite. On the other hand, the cementite formed upon tempering (7 % of volume) does not contain chromium, as all the chromium in the material is precipitated in primary carbides [Bagramov 2001], so its Young's modulus can be estimated at a value of 196 GPa according to [Umemoto 2001]. Taking the Young's modulus of the material after tempering at 800 K, 209 GPa, with a Poisson's ratio of 0.28, the resulting Young's modulus of the now ferritic matrix is calculated to be 205 GPa.

The resulting values for Young's modulus of the matrix before (197 GPa) and after (205 GPa) tempering are consistent with the decrease of Young's modulus of martensite with an addition of carbon reported in literature. According to [Schmidtmann 1965] and [Speich 1973], an addition of 0.5 wt.% (which is the concentration of carbon in solid solution estimated for our steel in the non-tempered state, see section 3.1.3) decreases the Young's modulus by 5 %. The value for the ferritic matrix after tempering at 800 K is somewhat lower than the value for pure iron (reported in literature in the range from 209 to 216 GPa), possibly due to the influence of dislocations and substitutional impurities [Ghosh 2002].

The plateau in the resonant frequency starting around 500 K for both vibrating reed and torsion pendulum measurements (fig. 4.7) corresponds to a strong modulus increase. Yet, no special increase of the modulus measured at room temperature is observed after tempering at 500 or 525 K. On the contrary, the rate of increase of the modulus appears to be lower starting from this point. It has to be emphasized that what we measure using mechanical spectroscopy as a technique is a dynamic modulus. It reflects the anelastic effects in the material. At 500 K, the modulus is reflecting the mobility of screw dislocations, which are not mobile at room temperature where only non-screw dislocations can contribute to internal friction. Therefore, at room temperature there is no modulus defect (decrease) due to the movement of screw dislocations. The plateau at 500 K could be related to a reduced mobility of screw dislocations or even to dislocation recovery; these effects being related to the decrease of the peak P5. The dynamic modulus measured at room temperature could reflect more the precipitation of pure Fe₃C cementite that forms during the second stage of tempering. As the Young's modulus of cementite (196 GPa) is found to be lower than that of the matrix and that of previously formed carbides containing chromium (245 GPa), its formation with tempering may lead to the change of the slope in the evolution of Young's modulus of the complete material (fig. 5.15).

The continuous decrease of the hardness can be explained first by the depletion of the matrix of interstitial carbon, which hardens the material through tetragonal distortion [Cohen 1962, Owen 1992]. A small hardening following the tempering in the temperature range between 200 and 330 K was observed for virgin Fe-Ni-C martensite with a M_S temperature sufficiently low to avoid quench-tempering (autotempering) [Speich 1972a]. The hardness measurements presented in fig. 5.16 are performed after long aging (8.5 months) at room temperature. After such long aging, pre-precipitation processes are expected to be well advanced. Although the room temperature thermopower measured as a function of aging time (fig. 3.16) indicates that the microstructure still evolves with aging, the TEP increase rate is much lower than just after quenching. The internal friction rise observed for as quenched material (fig. 4.8) at room temperature is also no longer present. Therefore, the first change of microstructure as a consequence of the tempering is expected to be the formation of transition carbides during the first

tempering stage, starting at 375 K. Within the experimental precision no hardening due to this precipitation is observed, therefore excluding the hardening by dislocation pinning by carbides, and supporting the hypothesis of solid-solution hardening.

The decrease of the hardness at higher temperatures should be attributed to the formation of coarse cementite and to recrystallization [Speich 1972a], the processes that are observed by TEM (figures 5.7 to 5.12) for samples tempered at 600 and 800 K.

The decrease of the dislocation density and the increase of the dislocation length observed by TEM after tempering at 600 and especially after 800 K confirm the explanation given for the decrease of the peak P5 amplitude, given in the previous chapter. However, the similarity between evolution trends (or in better words reciprocity) of TEP and IF measured at room temperature points to a strong dependence of the room temperature IF on the carbon concentration.

5.8 Conclusions

The first stage of tempering in our material starts around 375 K as manifested by a peak in the calorimetry thermogram. It is related to the precipitation of carbon in the martensite in form of transition η -carbides. This tempering stage is reflected by a first increase of the TEP and Young's modulus and by a decrease of the internal friction and hardness. It implies that all these quantities are sensitive to the concentration of carbon in solid solution in the martensitic matrix. It is thus of great interest to determine the carbon concentration and its evolution with tempering quantitatively. For this purpose, experiments with X-ray diffraction are performed. The results and further interpretation of both material evolution during tempering and of the differences in mechanical properties resulting from the two types of thermal treatment of the files are presented in the following chapter.

Both the room temperature mechanical properties of the material and its changes with aging and tempering appear to be strongly related to the concentration of carbon in solid solution. Therefore, it is of great interest to determine this concentration quantitatively. It should be underlined that only the concentration of carbon in solid solution in the martensitic matrix is of concern, and not the total amount in the sample. Moreover, as carbon is a light chemical element, EDS is not sufficiently sensitive to determine the small concentration variations. The traditional precise determination of the concentration of interstitial carbon in iron, by measuring the height of the Snoek peak in the internal friction spectrum, can neither be used in this case. In fact, we have seen that the Snoek peak is not present in the spectrum of martensite. However, the tetragonality itself may offer a measure of soluted carbon, as the parameters of the martensitic crystal lattice depend linearly on this quantity (eq. 1.2 and 1.3). Therefore, if the lattice of the body centered tetragonal martensitic unit cell can be determined precisely enough, the carbon concentration in the matrix can be assessed. In this chapter, we show that this was accomplished with X-ray diffraction performed at the ESRF synchrotron.

The carbon concentration evolution with tempering is studied in order to further interpret the results observed by other techniques described in Chapter 5. Also, as the measurements of thermoelectric power presented in Chapter 3 indicate that the carbon concentration varies in the file profile, X-ray diffraction is performed separately on the file bulk and on the teeth.

6.1 Tempering effects on carbon concentration

The experiment reported below aims at describing quantitatively the evolution of carbon concentration with tempering. Samples of the dimensions $5 \times 0.9 \times 0.2 \text{ mm}^3$ are extracted from the bulk of the BF treated file aged at room temperature for 16.5 months. The samples are obtained by spark-cutting, and then cleaned from oxide by sand-blasting at the temperature of liquid nitrogen. After this treatment, the thermopower of the samples was $S = 2.3 \text{ } \mu\text{V/K}$ indicating that the sample preparation did not lead to a significant heating (and therefore a microstructure change). Leaving one part of the samples as a room temperature reference to verify the local carbon variation, the rest was submitted to subsequent tempering of 25 min in temperature steps of 25 K, as in the experiments described in the previous chapter. After each tempering step, two samples were removed from the oven and kept for the X-ray diffraction

experiment. The X-ray diffraction spectra are obtained in transmission, using the wavelength $\lambda = 0.35037 \text{ \AA}$.

The diffraction spectra in the 2θ range (see section 2.2.3 and eq. 2.1 and 2.2) of the peak $\{110\}/\{011\}$ of the martensite are presented in fig. 6.1. No significant difference among reference (non-tempered) samples spectra is observed, so only one spectrum is displayed.

In fig. 6.1a, the spectra are plotted with the measured intensity normalized to the incident beam intensity. The peak $\{110\}/\{011\}$ of the martensite strongly sharpens with tempering, so that the reduction in peak width is followed by an increase of the peak height. Furthermore, a sharpening and later on an increase of the cementite peaks is observed (for example at $2\theta = 9.99^\circ$). The amplitude of the $\{110\}/\{011\}$ peak is also influenced by the sample dimensions (the amount of matter producing the diffraction spectrum). The small variation of the sample width (ranging from 0.85 to 1 mm) is the cause of the small irregularity in steps of the peak sharpening.

In fig. 6.1b, the spectra are plotted with the intensity normalized to the height of the $\{110\}/\{011\}$ martensite peak. In this scale, it is visible that the peak remains unchanged by tempering up to 350 K, and the first small change is observed after tempering at 375 K, followed by a strong sharpening of the peak after tempering at 400 K. As it is the peak $\{011\}$ that best combines a high sensitivity to tetragonalization (see paragraph 2.2.3) together with a high intensity (for an ideal tetragonal structure the intensity of the peak $\{011\}$ is twice the intensity of the peak $\{110\}$), the change between tempering steps is more evident on the left flank of the composed $\{110\}/\{011\}$ peak.

The strongest residual austenite peak, $\{111\}_a$, that should be positioned in the spectrum at $2\theta=9.66^\circ$, is hidden below the strongest martensite peak, $\{110\}/\{011\}$. Nevertheless, three residual austenite peaks are clearly visible in the spectrum between 10.8 and 20.6° of 2θ (fig. 6.2) up to the tempering at 500 K, when the peaks amplitudes decrease. After tempering at 525 K, the peaks are completely erased indicating the complete transformation of residual austenite to ferrite and cementite. The volume fraction of residual austenite cannot be determined from the spectrum with sufficient precision. The relative intensities of the peaks are not in agreement with theoretical and measured values possibly due to the preferred orientation. The rough estimation of the amount of residual austenite however gives a value between 4 and 10 vol.%. This is more than estimated from the TEM images (1 %).

No transition carbide peaks [Van Genderen 1993] are found in the spectrum, regardless of the tempering temperature. The probable reason is their nanometer size.

6.1.1 Carbon content fitting

The concentration of carbon in solid solution in the martensitic matrix is calculated by fitting the martensite double peaks ($\{110\}/\{011\}$, $\{200\}/\{002\}$, $\{211\}/\{112\}$ and $\{220\}/\{022\}$) using an iterative procedure. The peak positions are fitted using the Igor Pro (Wavemetrics) software. A gaussian peak shape is found to give the best fit. The peak positions are then compared with those calculated for the bct lattice (space group I4/mmm) using Checkcell. The calculation of the peak positions was based on eq. 1.2 and 1.3 that describe the change of the lattice parameters depending on the carbon concentration. The expected peak positions are then reintroduced as a new guess for the Igor fitting procedure. The procedure is repeated until a satisfactory correspondence of all peak positions with the tetragonal structure is found in Checkcell. The cementite peaks are fitted but not refined with the structure. The residual austenite (when present) is fitted using $\{200\}_a$ peak at $2\theta = 11.16^\circ$. Then, the related intensity of $\{111\}_a$ at $2\theta = 9.66^\circ$ is fixed for the fit of the martensite $\{110\}/\{011\}$ peak that overlays it.

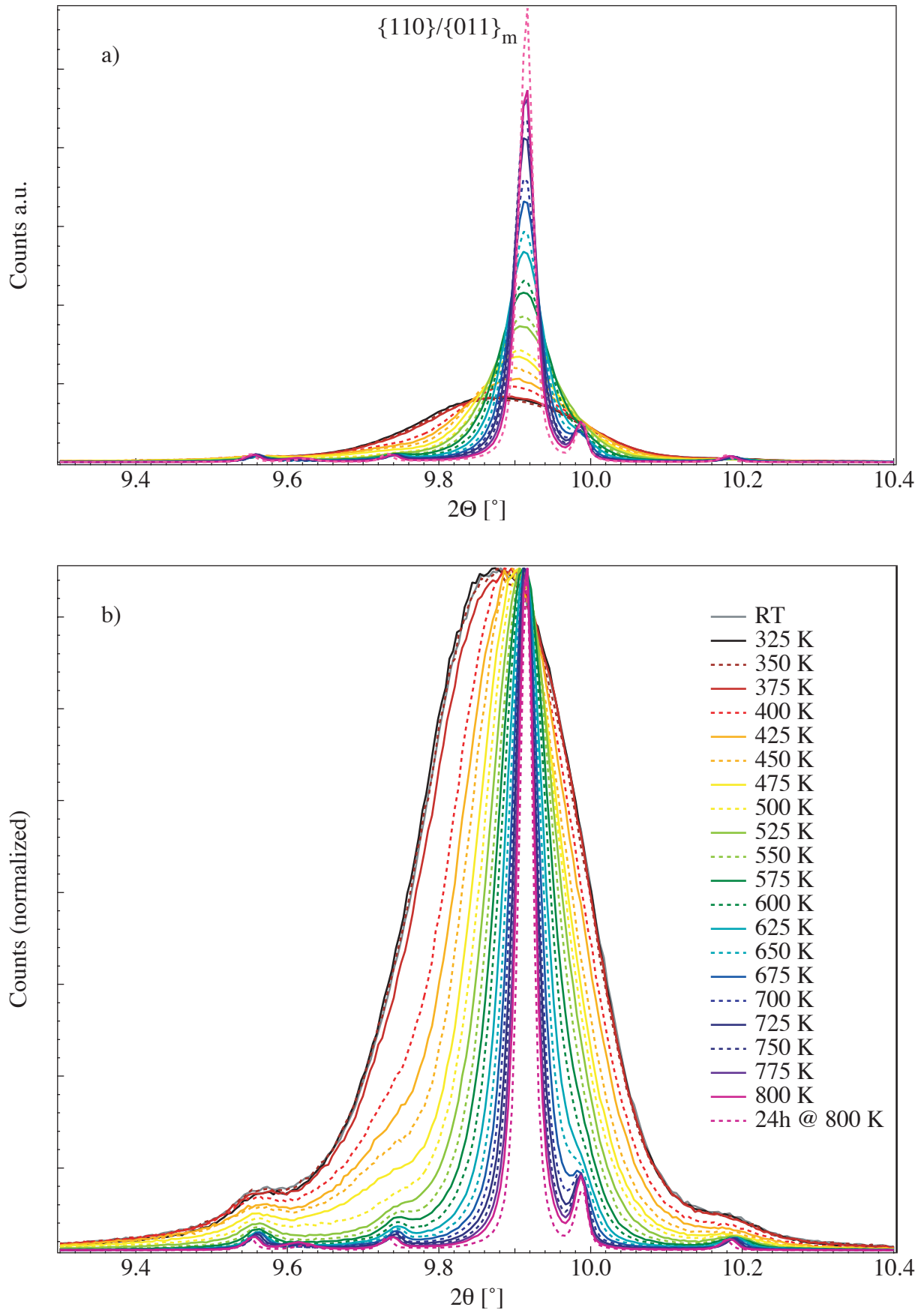


FIGURE 6.1. Effect of tempering on peak $\{110\}/\{011\}$ of martensite. a) Spectra normalized to the intensity of incident beam. b) Spectra normalized to the height of the $\{110\}/\{011\}$ peak.

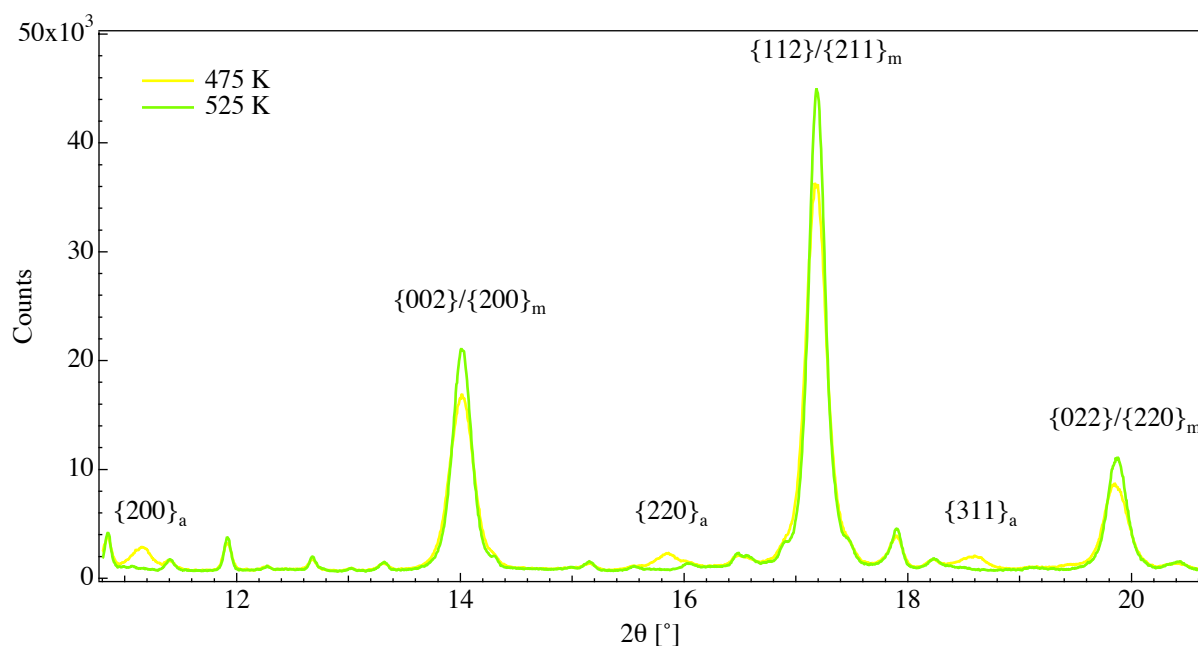


FIGURE 6.2. Disappearance of the residual austenite peaks ($\{200\}_a$, $\{220\}_a$ and $\{112\}_a$) after tempering at 525 K (green). The peaks are still present in the diffraction spectrum after tempering at 475 K (yellow).

The precision of the so determined carbon concentration is better for higher levels of tetragonality (i.e. for lower tempering temperatures). When the lattice becomes less asymmetric, the fitting of the two constituent peaks (for example $\{110\}$ and $\{011\}$) into a double peak profile becomes more ambiguous. For this reason, the determination of the carbon content by fitting the peak positions is made for tempering temperatures up to 575 K.

The interstitial carbon concentration as obtained from the fitting procedure is shown in fig. 6.3. Looking at the $\{110\}/\{011\}$ peak shape and position, it is reasonable to assume that after tempering at 800 K the carbon concentration approaches the solubility limit, which is very low for ferrite at room temperature (0.008 wt.%, see iron - iron carbide phase diagram in fig. 1.2). As mentioned above, the left flank of the $\{110\}/\{011\}$ peak shifts much more than the right flank as a function of carbon content. It is interesting to notice that the flank shift correlates very well with the carbon content obtained from the fitting procedure, as shown in fig. 6.3.

6.1.2 Correlation with TEP and internal friction

The trend of the decrease of the carbon content and the position of the left flank of the $\{110\}/\{011\}$ peak plotted in fig. 6.3 shows a similar trend as the decrease of internal friction measured at room temperature after tempering. Indeed, when internal friction is shown on the same graph (fig. 6.4), it displays a striking correlation with the position of the peak $\{110\}/\{011\}$ left flank, and therefore with the concentration of soluted carbon. The internal friction measured at room temperature after tempering is possibly a linear function of the concentration of carbon in solid solution.

The thermoelectric power is considered to be inversely proportional to the amount of carbon in solid solution. Here we take a very simplified model to relate the thermoelectric power to the concentration of interstitial carbon. It neglects the effects of dislocation density on TEP, as well as contributions to TEP other than electron diffusion. However, we'll see that, even if approximated, the model relates quite well with the experimental data.

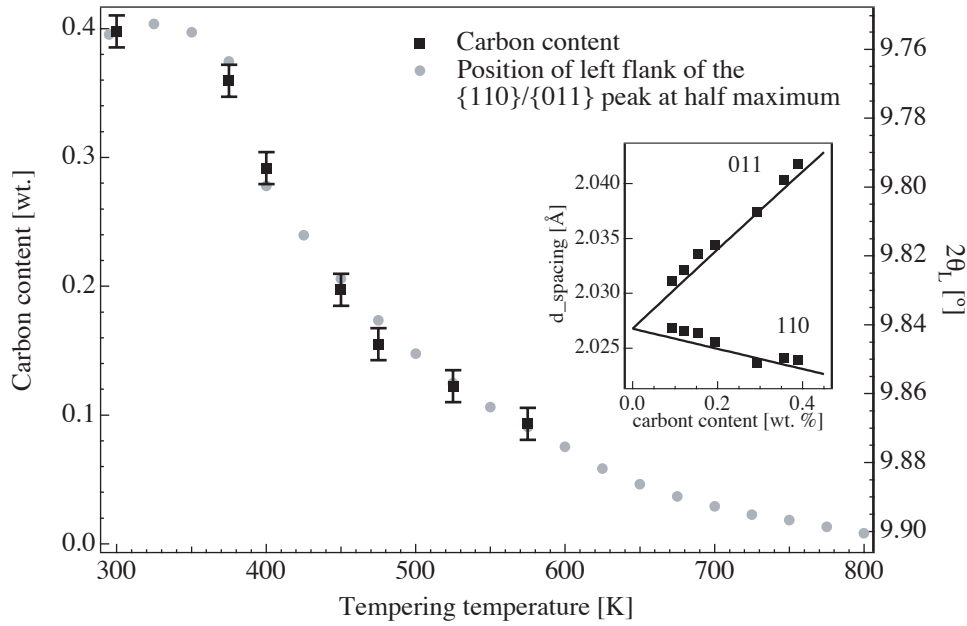


FIGURE 6.3. Interstitial carbon content obtained from fitting X-ray diffraction spectra compared to the position of the left flank of the $\{110\}/\{011\}$ peak measured at peak half maximum. The inset shows the comparison of fitted d -spacings for $\{110\}$ and $\{011\}$ peaks with those calculated as a function of carbon concentration.

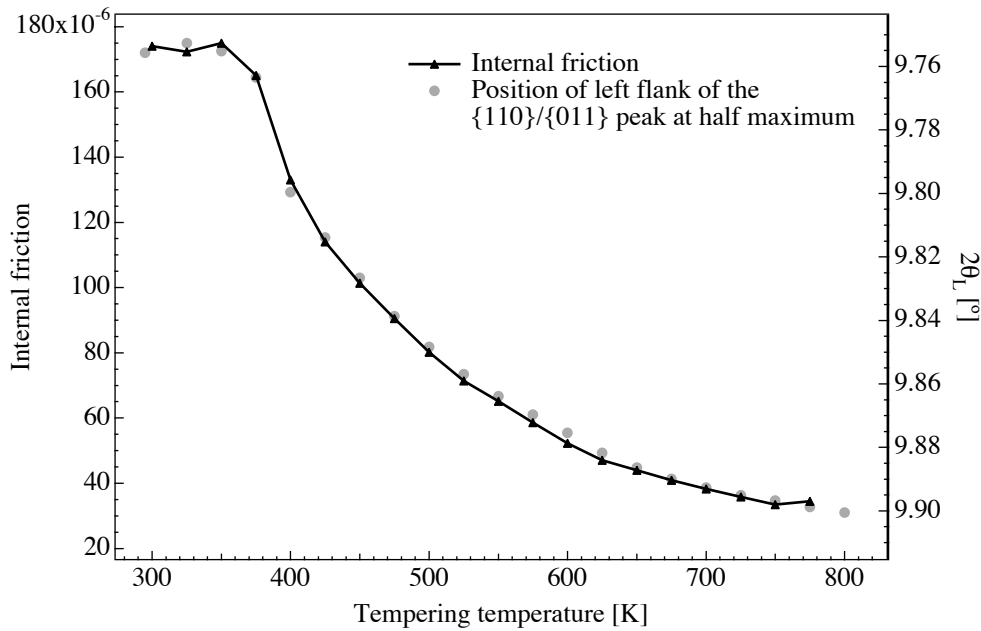


FIGURE 6.4. Correlation of internal friction measured at room temperature after tempering (left scale) with the position of the left flank of the $\{110\}/\{011\}$ peak measured at peak half maximum (right scale).

When the conduction electrons in a metallic material are scattered by phonons and impurity atoms of one kind, the electron-diffusion thermopower S^d is given by the following expression [Blatt 1976], derived from the Mott formula (eq. 2.4):

$$S^d = S_i^d + (S_0^d - S_i^d) \frac{\rho_0}{(\rho_0 + \Delta\rho)}, \quad (6.1)$$

where S_0^d and ρ_0 are respectively the thermopower and the electric resistivity of a perfect crystal of the pure metal and S_i^d is the thermopower characteristic to the impurity that causes an increase $\Delta\rho$ in the resistivity. Equation 6.1 shows that the plot of the thermopower S^d vs. the conductivity $1/(\rho_0 + \Delta\rho)$ at constant temperature should lie on a straight line. This relationship is called the Nordheim-Gorter rule.

The thermoelectric power in iron at room temperature is due to electron diffusion, magnon drag [Blatt 1976] and possibly phonon drag. However, in a dilute solid solution, the effect of carbon on contributions other than electron-diffusion thermopower might be sufficiently low. In the following, we assume that both magnon and phonon drag do not vary with carbon content. We also assume that the increase of resistivity is directly proportional to the impurity concentration C [Wenzl 1974], and can be expressed as

$$\Delta\rho = K_1 C \quad (6.2)$$

using a constant K_1 . As already mentioned above, it can be presumed that after tempering at 800 K, there is almost no carbon dissolved in the matrix.

Following the hypotheses above, and using eq. 6.1, the difference denoted ΔS , between TEP measured after tempering at a given temperature and TEP measured after tempering at 800 K, can be expressed as:

$$\Delta S = S(T) - S(800\text{K}) = -K_2 + \frac{K_2 \rho_0}{\rho_0 + K_1 C}, \quad (6.3)$$

where $K_2 = S_0^d - S_i^d$ is a constant.

Equation 6.3 can then be rewritten in the form:

$$C = K_3 \left(\frac{K_2}{\Delta S + K_2} - 1 \right), \quad (6.4)$$

where another constant is introduced: $K_3 = \rho_0 / K_1$.

The concentration of carbon calculated from the X-ray diffraction and presented in fig. 6.3 is regarded as a function of tempering temperature T , $C = C(T)$. On the other hand, the quantity ΔS as defined in eq. 6.3 is also a function of the tempering temperature and it can be easily determined for all tempering steps between 300 and 800 K using $S(T)$ and $S(800\text{K})$ presented in fig. 5.13a. If these two measurements are combined, it is possible to replace the tempering temperature with ΔS , and regard $C = C(\Delta S)$. From the experimental values of C and ΔS , it is then possible to use the eq. 6.4, and fit the parameters K_2 and K_3 .

The values of constants obtained from the fit are $K_2 = 24 \pm 14 \mu\text{V/K}$ and $K_3 = 1.6 \pm 1.1 \text{ wt.}\%$. When ΔS is substituted back with the tempering temperature in eq. 6.4, one obtains the values for the carbon concentration as a function of tempering temperature. The carbon concentration as calculated from eq. 6.4 and from X-ray diffraction data is compared to the room temperature internal friction in fig. 6.5. Again, the correlation is very good.

Internal friction and the left flank of the $\{110\}/\{011\}$ peak change smoothly with tempering indicating a continuous carbon depletion from the martensitic matrix, while the second stage of tempering at 525 K is marked in the TEP measurements by a step that slightly departs the related curve from the others (fig. 6.4). The possible explanation for this effect is that TEP is more sensitive to the transformation of residual austenite. The magnon peak in pure iron is situated at 200 K, but it is very large and therefore still contributing much to the room temperature TEP [Blatt 1976]. The fcc austenite is nonmagnetic, and for that reason it could lead to a

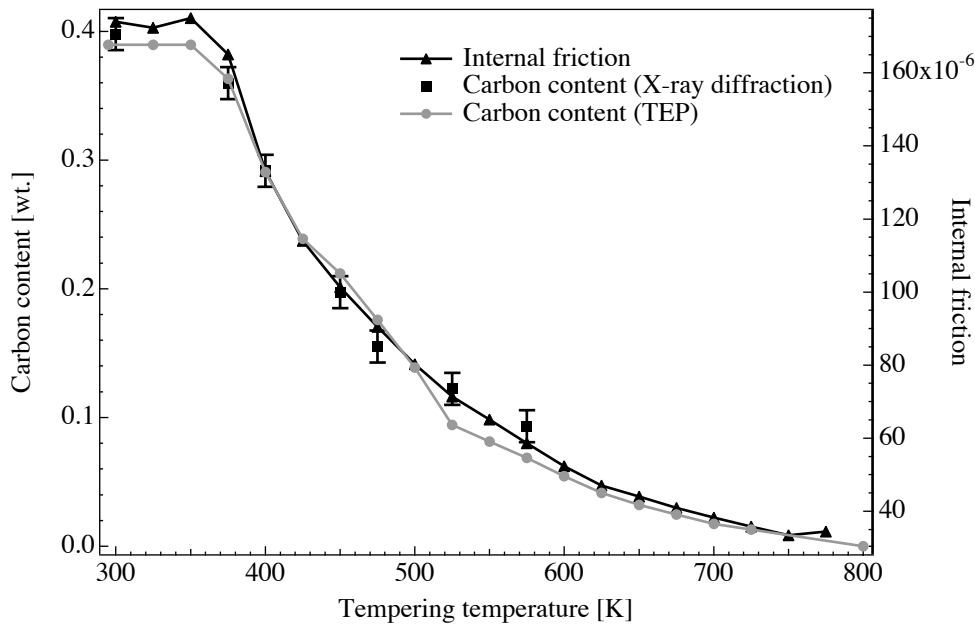


FIGURE 6.5. Correlation between internal friction measured at room temperature after tempering and carbon content derived from room temperature TEP measurements.

decrease of the magnon contribution in the thermopower of the material. After the transformation of residual austenite to ferrite and cementite, the TEP may increase due to a stronger magnon contribution. This effect is neglected in the carbon concentration fit using eq. 6.4 as described above. Still, the correlation between room temperature internal friction, thermoelectric power and concentration of interstitial carbon is clearly demonstrated.

6.2 Variation of the amount of carbon in solid solution within a file

The measurements of thermoelectric power described in the Chapter 3 indicate that there is a variation of carbon concentration in the file profile, specific for each type of thermal treatment (fig. 3.22). To confirm this hypothesis, X-ray diffraction spectra are obtained from different regions of a file: file bulk and teeth.

6.2.1 Experiments on the bulk and whole teeth of files

The first X-ray diffraction experiments designed to test the variation of the amount of carbon in solid solution within a file were performed in transmission, selecting with a slit the contribution from the bulk and from the teeth of a 0.2 mm thick file cross-section. Figure 6.6 shows the scanned zone, teeth appear gray in transmission. The wavelength used is 0.32727 \AA .

The diffraction patterns were obtained for both CN and BF files, with two scans made for each sample type. With the given resolution, the differences in the X-ray diffraction spectra are most easily seen on the peak $\{110\}/\{011\}$ of the martensite (fig. 6.7 and fig. 6.8). Although no direct splitting of the peak is observed, it is visible that the width of the peak varies from one sample type to the other, increasing from CN_bulk with the narrowest peak, through CN_teeth and BF_teeth, to BF_bulk for which the peak is the largest. Different width of the peak indicates the different level of tetragonalization (i.e. carbon content) increasing in the same order.



FIGURE 6.6. The CCD camera image obtained using X-rays in transmission of a 0.2 mm thick sample, showing the zone of the sample used to produce the diffraction spectrum from the teeth. Teeth appear gray in transmission.

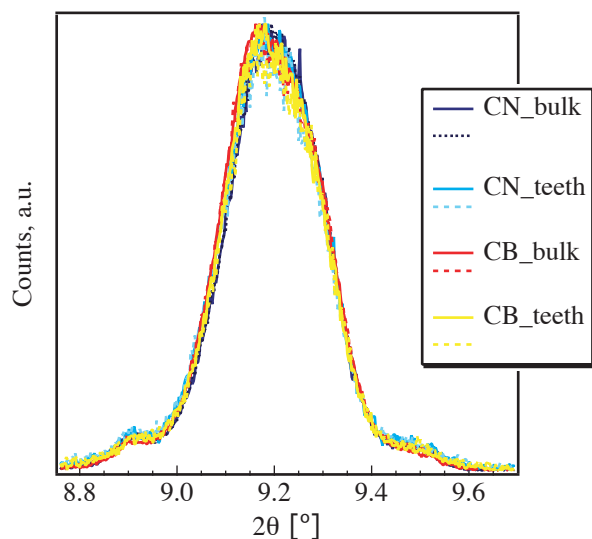


FIGURE 6.7. Peak $\{110\}/\{011\}$ of the martensite in the diffraction pattern of different samples. The diffracted intensity is normalized for each curve to obtain the same height of the peak for all samples.

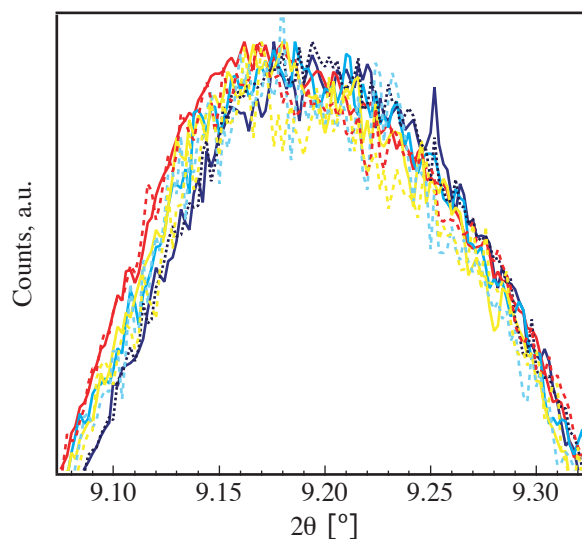


FIGURE 6.8. The differences in the peak width are visible: the peak broadens starting from CN_bulk with the narrowest peak, through CN_teeth and BF_teeth, to BF_bulk for which the peak is largest.

To quantify this difference and relate it to the interstitial carbon content, two Voigt-shape peaks were fitted in the $\{110\}/\{011\}$ profile (fig. 6.9). So obtained d-spacings of the $\{110\}$ and $\{011\}$ peaks are compared in fig. 6.10 to those calculated using eq. 1.2 and 1.3. Through the comparison of the difference in d-spacing between the two fitted peaks, the carbon content scale is added as the top axis.

The increase of the carbon content from one sample type to the next goes in the same order as the decrease of the TEP value (see fig. 3.22).

The values obtained for the carbon content are higher than those for a non-tempered sample in the experiment where tempering effects are studied (section 6.1.1). The likely explanation lies in the fact that the experiments on different file types are actually performed almost one year earlier than the experiments with tempering. Therefore, the files studied were aged at room temperature for only 7 instead of 16.5 months. During this time, some additional carbon redistribution surely occurred. The measurements of TEP as a function of aging time at room temperature described in Chapter 3 (fig. 3.16 and 3.17) confirm that the structure is still changing within this time delay. The average increase of the TEP for BF files between the two experiments was $0.26 \mu\text{V/K}$. The peak profile appears also to be less asymmetric after additional aging. In addition to the inevitable evolution of the material upon aging, the fitting of only one peak should be considered as less precise than the fitting of four peaks as in the experiment performed for studying tempering effects.

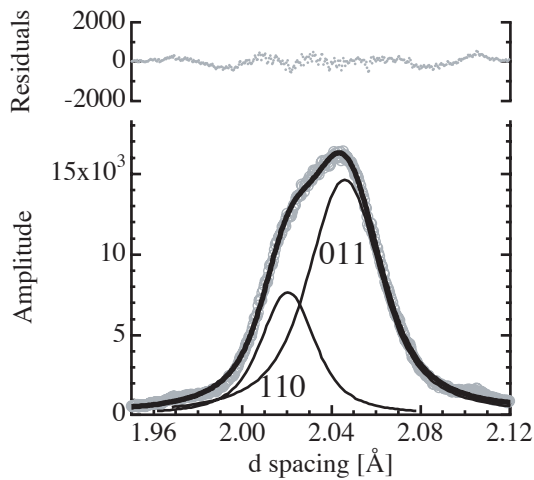


FIGURE 6.9. Example of fitting of two Voigt-shape peaks in the $\{110\}/\{011\}$ profile.

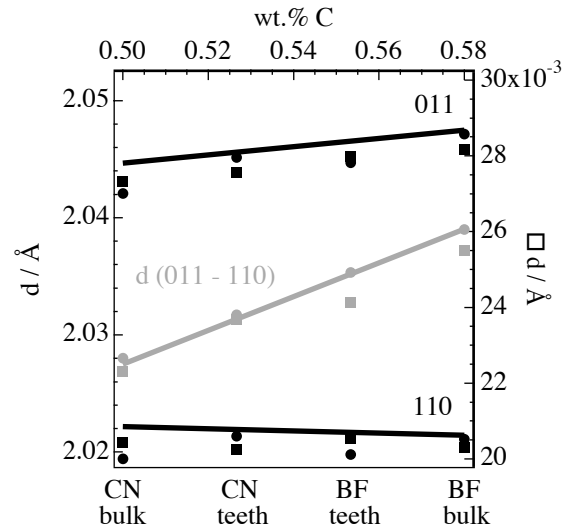


FIGURE 6.10. Fitted peak positions (left scale) and their difference (right scale) compared to theoretical ones (lines) for different samples (abscissa).

Nevertheless, the uncertainty of the absolute value for the carbon concentration cannot influence the relative ordering of the files according to the increase of the carbon content.

6.2.2 Experiments on the surface of file teeth

The experiments described in the former paragraph provide a scan over the whole height of the teeth. In order to test only the very surface of the teeth, some X-ray spectra were obtained at grazing incidence as shown in fig. 6.11. The diffracted rays are detected only if coming from a well defined space region thanks to the analyzer crystals. This comprises a zone of approximately 3 millimeters. As the teeth are 0.5 mm apart, the contribution to the diffraction spectrum comes from maximally six teeth. With an incidence angle of 0.573° , which gives $5\ \mu\text{m}$ at the end of the first scanned tooth (see fig. 6.11), and knowing that the intensity of the beam decreases down to 50% of the starting value by passing through a $200\ \mu\text{m}$ thick layer of the material, it is easy to show by a simple calculation that the scanned region comprises maximally $30\ \mu\text{m}$ of the teeth tips, with the main contribution to the diffraction pattern coming from even closer to the cusp.

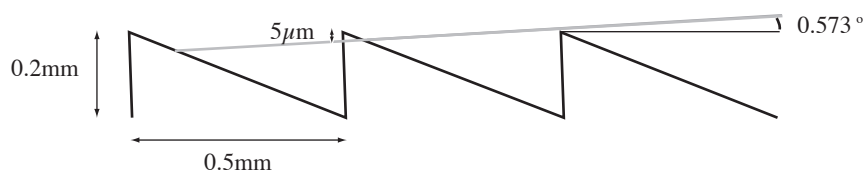


FIGURE 6.11. Design of the grazing incidence experiment on file teeth. The incident angle and corresponding penetration into the tooth are not in proportion with teeth dimensions; they are magnified for clarity.

The described experimental setup is used to scan the teeth of the following files: a BF file of good quality, 2 BF files of lower quality and a BF file of lower quality, which was treated a second time in the CN bath and whose quality matched the normally treated CN files. The quality of the files was tested manually as a part of the standard quality control procedure at UMV Valloirbe. The wavelength used in these experiments is $\lambda = 0.35037\ \text{\AA}$.

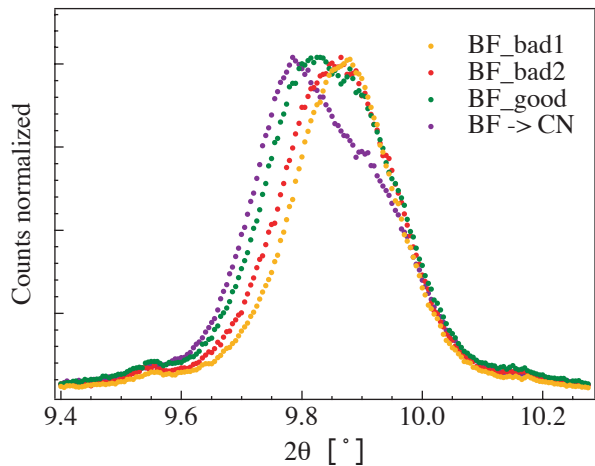


FIGURE 6.12. Peak $\{110\}/\{011\}$ of the martensite from the tips of the file teeth for 2 bad BF files, one good BF file and one bad BF file additionally treated in CN bath.

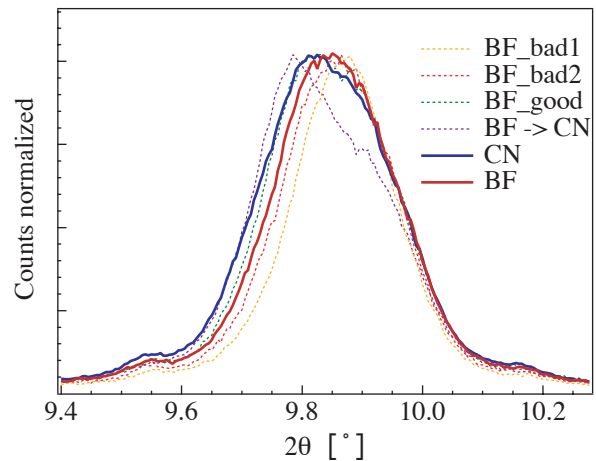


FIGURE 6.13. Peak $\{110\}/\{011\}$ of the martensite from the tips of the file teeth for files aged at room temperature for more than one year.

As seen from fig. 6.12, the resulting $\{110\}/\{011\}$ martensite peaks differ in width. The two unsatisfactory BF files show the narrowest peaks, the peak for the good BF file is wider, and for the additionally CN treated file the peak is widest and more asymmetric. The ordering of the files, going from the narrowest to the widest peak, corresponds to the ordering according to increasing quality. As the peak width reflects the tetragonality, i.e. the amount of soluted carbon, even remaining purely qualitative in the interpretation, it is possible to conclude that the quality of the files is related with the amount of carbon in solid solution at the very tips of the file teeth.

The same relation in peak width is found for a pair of BF and CN treated files, which have been aged at room temperature for 16.5 months (fig. 6.13). The measurements of TEP as a function of aging time (figures 3.16 and 3.17) have already shown that although the difference in average TEP between CN and BF treated files decreases with aging, the two groups of files are still clearly distinguishable by TEP measurements. Therefore, it can be concluded that in the very surface of the teeth tips, BF files have a lower concentration of soluted carbon than CN files.

The comparison of the $\{110\}/\{011\}$ peak for the very surface of BF and CN treated files is of great importance. It shows that the relation between BF and CN regarding carbon content is exactly the opposite at the very surface of the teeth than in the bulk. This is illustrated in fig. 6.14. The X-ray diffraction spectra obtained from the file bulk (previously presented in fig. 6.7 and 6.8) are transposed to the 2θ position for the wavelength $\lambda = 0.35037 \text{ \AA}$ according to eq. 2.1, and compared with the spectra obtained from the teeth surface. It has to be noted that the experiments on the bulk are made on different files, which were aged for almost a year less. Figure 6.14 clearly illustrates that the peak broadening at the surface is smaller for BF files. The situation is the opposite in the bulk. The variation of the carbon concentration in the file is indicated by the TEP measurement. Regarding X-ray diffraction results summarized in fig. 6.14, it is possible to make a qualitative extension of TEP variation in the file profile presented in fig. 3.22 to the teeth surface (fig. 6.15). The concentration of carbon decreases as the TEP increases: in the bulk of the files it is higher for the BF than for the CN treated files, and in the teeth surface it is higher for the CN than for the BF treated files.

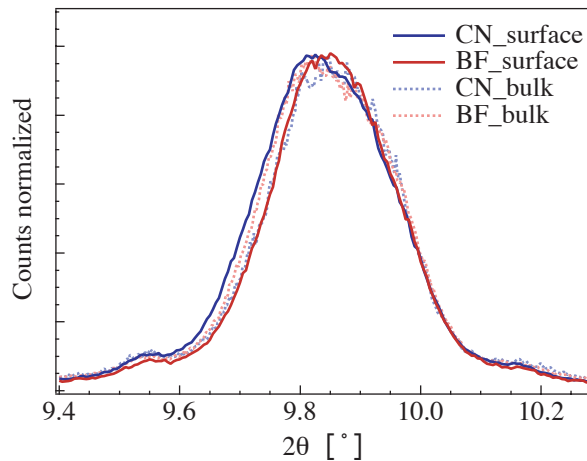


FIGURE 6.14. Comparison of the martensite $\{110\}/\{011\}$ peak for teeth and the bulk of CN and BF treated files. The measurements from the bulk are transposed to the wavelength $\lambda = 0.35037 \text{ \AA}$ according to eq. 2.1.

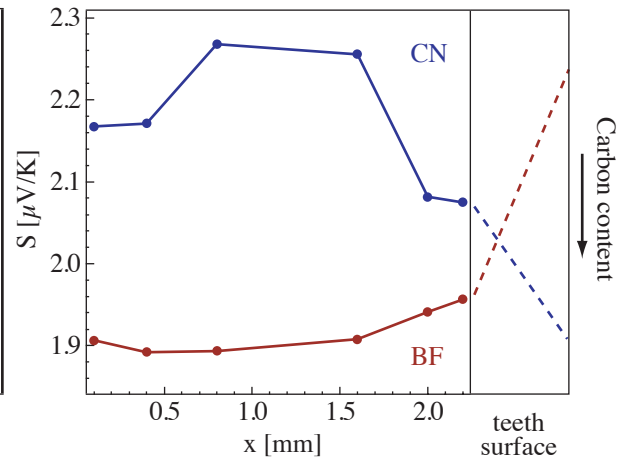


FIGURE 6.15. Qualitative extension of the variation of TEP in the file profile to the teeth surface (arbitrary scale) based on comparison of fig. 6.14 and 3.22.

6.3 Conclusions

The results presented in this chapter demonstrate how X-ray diffraction can be used for a quantitative evaluation of the concentration of carbon soluted in the martensitic matrix. The carbon concentration is calculated from fitted positions of martensite diffraction peaks. Compared to bcc ferrite, the peaks of martensite are split due to the lattice tetragonalization, which is proportional to the content of soluted carbon. The comparison of the martensite peak positions with those predicted for a certain carbon concentration allows the quantitative assessment. The concentration of carbon in non-tempered martensite of 0.4 wt.% starts to decrease with tempering at 375 K. The further decrease with tempering is smooth, and the carbon concentration recedes to the solubility limit (very close to zero) after tempering at 800 K.

The concentration of carbon evaluated for different levels of tempering is compared with the room temperature internal friction measured as a function of tempering temperature. The room temperature IF seems to be a linear function of the soluted carbon concentration. A simple model is used to relate the room temperature thermoelectric power to the carbon concentration assuming that only the electron diffusion component of TEP is influenced by soluted carbon atoms. The model is fitted to the values for the carbon concentration obtained from X-ray diffraction data, and compared with internal friction. The correlation found is very good. Thermoelectric power and internal friction measured at room temperature could be independently used to assess the carbon concentration in martensite after an appropriate calibration by X-ray diffraction.

X-ray diffraction is also used to verify the variation of carbon concentration in the file profile. The variation of carbon concentration indicated by thermoelectric power (for CN files higher carbon concentration in the teeth than in the bulk, and the opposite for BF files) is confirmed. Moreover, the experiments with grazing incidence allow to assess the concentration of carbon very close to the teeth tips. The carbon concentration in the surface layer is found to be higher for CN than for BF treated files. Therefore, the inferior performance of BF treated files when compared to the CN treated ones can be related to decarburization in the very teeth surface.

This work was carried out as a part of a project in collaboration with one of the most important file producers in the world, UMV Vallorbe, Switzerland. As such, it had a well defined technological objective: to understand the effects of a particular thermal treatment on the mechanical properties of carbon steel for the production of files. Namely, the objective was to explain the discrepancy in file performance for files thermally treated in a conveyor belt furnace (BF) and in a cyanide bath (CN). Traditional testing methods were not sufficient to find the cause of the lesser performance of BF treated files. Therefore, the problem has been investigated taking a scientific approach, using various experimental techniques.

The file material is a high carbon tool steel. The microstructure of the material is studied by transmission electron microscopy (TEM) and atomic force microscopy (AFM). These techniques reveal a complex structure of the material, composed of a matrix and embedded cementite carbides. The matrix is almost completely martensitic, with both lath and plate martensite present. A small amount of residual austenite is also found. The dislocation density in the material is very high. However, no clear difference in the microstructure is observed between BF and CN files. Also, no clear evidence of variation of the microstructure with distance from the surface is found.

Thermoelectric power (TEP) measured at room temperature is used as a very sensitive probe of the microstructural state of the material. It is sensitive enough to distinguish between the two types of thermal treatment. The measurements can be performed fast and in a completely non-destructive manner, using the whole files. Although no absolute value can be attributed to the particular heat treatment, because the TEP increases as a function of time after the quenching, the TEP is consistently higher for CN than for BF treated files. This difference is attributed to different concentrations of carbon in solid solution in the martensitic matrix: a higher TEP is related to a lower concentration of carbon. Therefore, the BF treated files have on average more carbon in solid solution in the martensitic matrix than the CN treated ones. The TEP measurements also indicate a variation of carbon content within the file profile that is different for BF and CN treatments. The BF treated files have a higher thermopower (and therefore less carbon in solid solution) in the teeth than in the bulk of the file and the opposite is found for CN treated files.

The results of the mechanical tests also display a difference between CN and BF treated files, seemingly contradictory to the file performance. Compression tests show that samples extracted from the bulk of BF treated files have a higher yield stress and compression strength.

The hardness measured by nanoindentation is also found to be higher for the BF as compared to the CN treated files. When compared to the TEP results, mechanical tests indicate that the resistance to deformation is proportional to the amount of carbon in solid solution.

Mechanical spectroscopy is used in order to study the micro-mechanical mechanisms responsible for the macro-mechanical properties of the material. Namely, it is used to examine the mobility of point defects and dislocations, and their interaction. It is found that significant aging occurs at room temperature shortly after quenching, and that the stabilized room temperature structure becomes again unstable with heating to temperatures higher than 375 K, causing a decrease of IF and an increase of the elastic modulus. The martensitic structure is characterized by a rich internal friction temperature spectrum composed of five peaks (named in increasing order) due to different relaxation and transition phenomena. The peak P1 is interpreted as a Snoek-Köster hydrogen peak. A mechanism is proposed for the peak P2, involving pipe-diffusion along kinks on screw dislocations. The peaks P3 and most likely also P4 are not relaxation peaks. They are related to tempering effects that occur at temperatures higher than 375 K. The peak P5 is interpreted as a Snoek-Köster carbon peak.

A small but significant difference between the IF spectra for the BF and CN treated materials is found in very precise high frequency measurements: the internal friction is slightly higher for the BF treated material. Upon heating, the difference becomes visible with the rise of the peak P2, and it continues to rise so that it is detectable also at room temperature. This difference is attributed to the existence of an athermal IF background proportional to the amount of carbon in solid solution. The background is related to long range dislocations - carbon interaction and this is the first observation of such a mechanism in steel. This mechanism is also responsible for the increase of the IF observed for as quenched samples.

The tempering of the material indicated by the transition peaks in the internal friction measurements is studied combining several techniques. Differential scanning calorimetry reveals two stages of tempering. They are attributed to the precipitation of transition η -carbides and to the transformation of residual austenite followed by precipitation of cementite, as confirmed by TEM observations. The recovery and recrystallization that occur at higher temperatures are also observed by TEM. The tempering is reflected in an increase of thermoelectric power and Young's modulus, and by a decrease of hardness and internal friction. All mentioned physical quantities start to change with the first stage of tempering observed around 375 K, which implies their sensitivity to soluted carbon. Their further evolution with tempering is somewhat different, reflecting different sensitivity to other mechanisms. The hardness continuously decreases with tempering and no precipitation hardening is observed.

Finally, X-ray diffraction experiments allow quantification of the amount of carbon in solid solution in the martensite. The carbon content is assessed from a comparison of the positions of the martensite peaks in the X-ray diffraction spectra with the position calculated for different levels of lattice tetragonality, which is linearly dependent on carbon content. The concentration of carbon in non-tempered martensite of 0.4 wt.% starts to decrease with tempering at 375 K. The further evolution of carbon concentration is smooth and the carbon content stabilizes at the solubility limit after tempering at 800 K.

The comparison of TEP, IF and X-ray diffraction results shows a strong correlation between the carbon content and room temperature IF and TEP. A linear proportionality of IF to carbon content is observed even in the absence of the carbon Snoek peak.

After demonstrating the applicability of X-ray diffraction to the determination of the evolution of the carbon content with tempering, the method is used to verify the variation of carbon con-

centration in the file profile. The variation of carbon concentration indicated by the thermoelectric power (for CN files the carbon concentration is higher in teeth than in the bulk, while the opposite is observed for BF files) is confirmed by X-ray diffraction. Moreover, the experiments with grazing incidence allow assessment of the concentration of carbon very close to the teeth tips. The carbon concentration in the surface layer is found to be higher for CN than for the BF treated files.

The above mentioned experiments enable us to interpret the difference between the two types of thermal treatment.

The mechanical tests by nanoindentation and compression performed on the file bulk show a higher hardness, compression strength and yield stress for BF treated files. The thermoelectric power is found to be lower for the BF than for CN file bulk, and this is related to the higher concentration of carbon in solid solution. The tempering experiments confirm that as the concentration of carbon soluted in the matrix is reduced by increasing the tempering temperature, the hardness decreases. No particular increase of the hardness due to the formation of carbides is observed. Therefore, it is concluded that the main hardening mechanism in our steel is due to solution hardening.

The TEP measurements indicate a variation of carbon concentration in the file profile. For BF files, a lower TEP in the bulk reflects a higher concentration of carbon than in the file teeth, and the opposite is found for CN files. But at the very surface of the file teeth, the part of file that actually participates in the filing process, the CN treated files have a higher concentration of carbon than the BF ones. This condition implies a higher hardness, and therefore better resistance to wear. Although the BF treated files have more carbon in solid solution in the bulk (presumably from a more drastic quenching), the concentration of carbon at the tips of the teeth is lower, and the resulting resistance to wear is unsatisfactory.

The observed gradient in carbon concentration can play an additional beneficial role in the case of CN treated files, due to the internal stresses. As the surface martensite contains more dissolved carbon than the bulk, the crystal lattice is more tetragonally distorted. Moreover, the specific volume of a unit cell is bigger than in the bulk of the file. This can lead to the existence of compressive stresses in the surface, preventing crack formation. The opposite is true for BF treated files: having less carbon in the teeth than in the bulk, the tensile stresses that develop at the surface could lead to easier crack formation and propagation and have a detrimental effect on the file quality.

Bibliography

- Astié P., Peyrade J.P., Groh P., Pics De Relaxation Des Dislocations Dans Le Fer Après Déformation a Basse Température, *Scripta Metallurgica* **14**, 611 (1980).
- Azcoïtia C., *Effets Magnéto-mécaniques Dans Des Alliages Ferromagnétiques Du Type Fe-Cr-X*, Ph.D. Thesis EPFL N° 2531, 2002.
- Bagramov R., Mari D., Benoit W., Internal Friction in a Martensitic High Carbon Steel, *Philosophical Magazine A* **81**, 2797 (2001).
- Barnard R.D., *Thermoelectricity in Metals and Alloys* (Taylor & Francis Ltd, London, 1972).
- Benkirat D., Merle P., Borrelly R., Effects of Precipitation on the Thermoelectric Power of Iron-Carbon Alloys, *Acta Metallurgica* **36**, 613 (1988).
- Benoit W., Dislocation: Description and Dynamics in *Mechanical Spectroscopy Q-1 2001: With Applications to Materials Science* (eds. Schaller R., Fantozzi G., Gremaud G.) (Trans Tech Publications, Uetikon-Zuerich, Switzerland, 2001).
- Blatt F.J., Flood D.J., Rowe V., Schroeder P.A., Cox J.E., Magnon-Drag Thermopower in Iron, *Physical Review Letters* **18**, 395 (1967).
- Blatt F.J., Schroeder P.A., Foiles C.L., Greig D., *Thermoelectric Power of Metals* (Plenum Press, New York, 1976).
- Bonjour C., Benoit W., Effect of Substitutional Impurities on the Low-Temperature Internal-Friction Spectrum of Coldworked Diluted Gold-Alloys, *Acta Metallurgica* **27**, 1755 (1979).
- Borrelly R., Applications Des Mesures De Pouvoir Thermoélectrique à L'étude Des Alliages Métalliques, *Memoires Scientifiques De La Revue De Metallurgie* **76**, 37 (1979).
- Borrelly R., Benkirat D., Sensibilité Du Pouvoir Thermoélectrique à L'état Microstructural Du Fer Et Du Fer-Azote, *Acta Metallurgica* **33**, 855 (1985).
- Borrelly R., Biron I., Delaneau P., Thomas B.J., Dosage Du Carbone En Solution Dans Les Aciers Extra-Doux Par Mesure Du Pouvoir Thermoélectrique. Application à La Détermination Des Teneurs En Carbone En Solution à Différentes Étapes D'un Cycle De Recuit Continu, *Revue De Metallurgie-Cahiers D Informations Techniques* **90**, 685 (1993).
- Chang L., Smith G.D.W., Olson G.B., Aging and Tempering of Ferrous Martensites, *Journal de Physique* **47**, 265 (1986).
- Cheng L., Bottger A., Dekeijser T.H., Mittemeijer E.J., Lattice-Parameters of Iron-Carbon and Iron-Nitrogen Martensites and Austenites, *Scripta Metallurgica et Materialia* **24**, 509 (1990).
- Cheng L., Brakman C.M., Korevaar B.M., Mittemeijer E.J., The Tempering of Iron-Carbon Martensite - Dilatometric and Calorimetric Analysis, *Metallurgical Transactions a-Physical Metallurgy and Materials Science* **19**, 2415 (1988).
- Cheng L., Vanderpers N.M., Bottger A., Dekeijser T.H., Mittemeijer E.J., Lattice Changes of Iron-Carbon Martensite on Aging at Room Temperature, *Metallurgical Transactions a-Physical Metallurgy and Materials Science* **22**, 1957 (1991).
- Clyne T.W., Withers P.J., *An Introduction to Metal Matrix Composites* (eds. Davis E.A., Ward I.M.) (Cambridge University Press, Cambridge, 1993).

- Cohen M., The Strengthening of Steel, *Transactions of the Metallurgical Society of AIME* **224**, 638 (1962).
- Eshelby J.D., The Determination of the Elastic Field of an Ellipsoidal Inclusion, and Related Problems, *Proc. R. Soc.* **241A**, 376 (1957).
- Formerod R., *Un Phénomène D'interaction Entre Défauts D'irradiation Et Dislocations Dans L'argent Polycristallin*, Ph.D. Thesis EPFL N° 70, 1968.
- Fuoss R.M., Kirkwood J.G., Electrical Properties of Solids. Viii. Dipole Moments in Polyvinyl Chloride-Diphenyl Systems, *Journal of the American Chemical Society* **63**, 385 (1941).
- Ghosh G., Olson G.B., The Isotropic Shear Modulus of Multicomponent Fe-Base Solid Solutions, *Acta Materialia* **50**, 2655 (2002).
- Gremaud G., Dislocation - Point Defect Interactions in *Mechanical Spectroscopy Q-1 2001: With Applications to Materials Science* (eds. Schaller R., Fantozzi G., Gremaud G.) (Trans Tech Publications, Uetikon-Zuerich, Switzerland, 2001).
- Gremaud G., Kustov S., Theory of Dislocation-Solute Atom Interactions in Solid Solutions and Related Nonlinear Anelasticity, *Physical Review B* **60**, 9353 (1999).
- Han K., Van Genderen M.J., Bottger A., Zandbergen H.W., Mittemeijer E.J., Initial Stages of Fe-C Martensite Decomposition, *Philosophical Magazine a-Physics of Condensed Matter Structure Defects and Mechanical Properties* **81**, 741 (2001).
- Honeycombe R., *Steels; Microstructure and Properties* (ed. R. Honeycombe P.H.) (1980).
- Inoue T., Haraguchi K., Kimura S., Analysis of Stresses Due to Quenching and Tempering of Steel, *Transactions of the Iron and Steel Institute of Japan* **18**, 11 (1978).
- Isoré A., *Etude De La Recristallisation Primaire De L'argent Par Mesures De Frottement Intérieur Et De Défaut De Module*, Ph.D. Thesis EPFL N° 159, 1973.
- Johnson R.A., Calculation of the Energy and Migration Characteristics of Carbon in Martensite, *Acta Metallurgica* **13**, 1239 (1965).
- Kamber K., Keefer D., Wert C., Interactions of Interstitials with Dislocations in Iron, *Acta Metallurgica* **9**, 403 (1961).
- Kis A., *Mechanical Properties of Mesoscopic Objects*, Ph.D. Thesis EPFL N° 2876, 2003.
- Klems G.J., Miner R.E., Hultgren F.A., Gibala R., Internal Friction in Ferrous Martensites, *Metallurgical Transactions A* **7**, 839 (1976).
- Krauss G., Tempering and Structural Changes in Ferrous Martensites in *Phase Transformations in Ferrous Alloys* (eds. Mader A.R., Goldstein J.I.) (The Metallurgical Society, 1984).
- Kurdjumov G.V., Martensite Crystal Lattice, Mechanism of Austenite-Martensite Transformation and Behavior of Carbon Atoms in Martensite, *Metallurgical Transactions A* **7A**, 999 (1976).
- Kustov S., Gremaud G., Benoit W., Golyandin S., Sapozhnikov K., Nishino Y., Asano S., Strain Amplitude-Dependent Anelasticity in Cu-Ni Solid Solution Due to Thermally Activated and Athermal Dislocation-Point Obstacle Interactions, *Journal of Applied Physics* **85**, 1444 (1999).
- Languillaume J., Kapelski G., Baudalet B., Cementite Dissolution in Heavily Cold Drawn Pearlitic Steel Wires, *Acta Materialia* **45**, 1201 (1997).

- Lavaire N., Massardier V., Merlin J., Quantitative Evaluation of the Interstitial Content (C and/or N) in Solid Solution in Extra-Mild Steels by Thermoelectric Power Measurements, *Scripta Materialia* **50**, 131 (2004).
- Mercier O., *Effets des impuretés sur le spectre et la restauration des pics de Hasiguti de l'or écroui ou irradié*, Ph.D. Thesis EPFL N° 180, 1974.
- MacDonald D.K.C., *Thermoelectricity: An Introduction to the Principles* (John Wiley & Sons, New York, London, 1962).
- Maddin R., A History of Martensite: Some Thoughts on the Early Hardening of Iron in *Martensite* (eds. Olson G.B., Owen W.S.) (ASM International, USA, 1992).
- Magalas L.B., Dufresne J.F., Moser P., The Snoek-Köster Relaxation in Iron, *Journal de Physique* **42**, 127 (1981).
- Mari D., Bolognini S., Feusier G., Viatte T., Benoit W., Experimental Strategy to Study the Mechanical Behaviour of Hardmetals for Cutting Tools, *International Journal of Refractory Metals & Hard Materials* **17**, 209 (1999).
- Massardier V., Lavaire N., Soler M., Merlin J., Comparison of the Evaluation of the Carbon Content in Solid Solution in Extra-Mild Steels by Thermoelectric Power and by Internal Friction, *Scripta Materialia* **50**, 1435 (2004).
- Mittemeijer E.J., Analysis of the Kinetics of Phase-Transformations, *Journal of Materials Science* **27**, 3977 (1992).
- Mittemeijer E.J., Wierszyllowski I.A., The Isothermal and Nonisothermal Kinetics of Tempering Iron-Carbon and Iron-Nitrogen Martensites and Austenites, *Zeitschrift für Metallkunde* **82**, 419 (1991).
- Moss S.C., Static Atomic Displacements in Iron-Carbon Martensite, *Acta Metallurgica* **15**, 1815 (1967).
- Mura T., Tamura I., Brittain J.O., On the Internal Friction of Cold-Worked and Quenched Martensitic Iron and Steel, *Journal of Applied Physics* **32**, 92 (1961).
- Nishiyama Z., *Martensitic Transformation* (Academic Press, New York, 1978).
- Nowick A.S., Berry B.S., *Anelastic Relaxation in Crystalline Solids* (Academic Press, New York, 1972a).
- Nowick A.S., Berry B.S., The High-Temperature Background in *Anelastic Relaxation in Crystalline Solids* (Academic Press, New York, 1972b).
- Numakura H., Koiwa M., The Snoek Relaxation in Dilute Ternary Alloys. A Review, *Journal de Physique IV* **6**, C8 (1996).
- Ohmori Y., Tamura I., Epsilon Carbide Precipitation During Tempering of Plain Carbon Martensite, *Metallurgical Transactions a-Physical Metallurgy and Materials Science* **23**, 2737 (1992).
- Oliver W.C., Phar G.M., An Improved Technique for Determining Hardness and Elastic-Modulus Using Load and Displacement Sensing Indentation Experiments, *Journal of Materials Research* **7**, 1564 (1992).
- Olson G.B., Introduction: Martensite in Perspective in *Martensite* (eds. Olson G.B., Owen W.S.) (ASM International, USA, 1992).

- Olson G.B., Cohen M., Early Stages of Aging and Tempering of Ferrous Martensites, *Metallurgical Transactions a-Physical Metallurgy and Materials Science* **14**, 1057 (1983).
- Owen W.S., The Strength of Ferrous Martensite in *Martensite* (eds. Olson G.B., Owen W.S.) (ASM International, 1992).
- Parke S., Logarithmic Decrements at High Damping, *British Journal of Applied Physics* **17**, 271 (1966).
- Petarra D.P., Beshers D.N., Cold-Work Internal Friction Peak in Iron, *Acta Metallurgica* **15**, 791 (1967).
- Rodriguez C.A.V.D.A., Prioul C., Hyspecka L., Isothermal Martensitic Transformation in Fe-Ni and Fe-Ni-C Alloys at Subzero Temperatures, *Metallurgical Transactions A* **15**, 2193 (1984).
- Rose A., Hougardy H., *Atlas Zur Wärmebehandlung Der Stähle* (Verlag Stahleisen m.b.H., Düsseldorf, 1972).
- Saitoh H., Yoshinaga N., Ushioda K., Influence of Substitutional Atoms on the Snoek Peak of Carbon in B.C.C. Iron, *Acta Materialia* **52**, 1255 (2004).
- Samuel F.H., Hussein A.A., A Comparative-Study of Tempering in Steel, *Materials Science and Engineering* **58**, 113 (1983).
- San Juan J., Fantozzi G., No M.L., Esnouf C., Hydrogen Snoek-Köster Relaxation in Iron, *Journal of Physics F: Metal Physics* **17**, 837 (1987a).
- San Juan J., Fantozzi G., No M.L., Esnouf C., Vanoni F., Analysis of Snoek-Köster (H) Relaxation in Iron, *Journal de Physique* **46**, C10 (1985).
- San Juan J., No M.L., Fantozzi G., Esnouf C., Experimental-Evidence of Relaxation Arising from the Motion of Geometrical Kinks on Screw Dislocations in Iron, *Philosophical Magazine Letters* **56**, 237 (1987b).
- Schaller R., Fantozzi G., Gremaud G. (eds.), *Mechanical Spectroscopy Q-1 2001: With Applications to Materials Science* (Trans Tech Publications, Uetikon-Zuerich, Switzerland, 2001).
- Schmidtmann E., Hougardy H., Schenk H., Investigation of the Decomposition of Martensite in the First Stage of Tempering by Measuring Elasticity Modulus and Damping at High Frequencies, *Archiv für das Eisenhüttenwesen* **36**, 191 (1965).
- Schultz H., Defect Parameters of B.C.C. Metals: Group Specific Trends, *Materials Science and Engineering* **A141**, 149 (1991).
- Seeger A., A Theory of the Snoek-Köster Relaxation (Cold-Work Peak) in Metals, *Physica Status Solidi. Section A. Applied Research* **55**, 457 (1979).
- Seeger A., Wüthrich C., Dislocation Relation Processes in Body-Centred Cubic Materials, *Il Nuovo Cimento* **33B**, 39 (1976).
- Snoek J.L., *Physica* **6**, 591 (1939).
- Speich G.R., Tempering of Low-Carbon Martensite, *Transactions of the Metallurgical Society of AIME* **245**, 2553 (1969).
- Speich G.R., Leslie W.C., Tempering of Steel, *Metallurgical Transactions* **3**, 1043 (1972a).
- Speich G.R., Leslie W.C., Elastic-Constants of Martensite, *Metallurgical Transactions* **4**, 1873 (1973).

- Speich G.R., Schwoebl.Aj, Leslie W.C., Elastic-Constants of Binary Iron-Base Alloys, *Metallurgical Transactions* **3**, 2031 (1972b).
- Speich G.R., Taylor K., Tempering of Ferrous Martensites in *Martensite* (eds. Olson G.B., Owen W.S.) (ASM International, 1992).
- Stark P., Averbach B.L., Cohen M., Internal Friction Measurements on Tempered Martensite, *Acta Metallurgica* **4**, 91 (1956).
- Stark P., Averbach B.L., Cohen M., Influence of Microstructure on the Carbon Damping Peak in Iron-Carbon Alloys, *Acta Metallurgica* **6**, 149 (1958).
- Taniyama A., Takayama T., Arai M., Hamada T., Structure Analysis of Ferrite in Deformed Pearlritic Steel by Means of X-Ray Diffraction Method with Synchrotron Radiation, *Scripta Materialia* **51**, 53 (2004).
- Timoshenko S., *Résistance Des Matériaux* (Librarie Polytechnique Béranger, Paris, 1963).
- Tkalcec I., Mari D., Mechanical Spectroscopy in Martensitic and Cold-Worked Carbon Steels, *Defects and Diffusion in Metals: An Annual Retrospective Iv* **203-205**, 253 (2002).
- Umemoto M., Liu Z.G., Masuyama K., Tsuchiya K., Influence of Alloy Additions on Production and Properties of Bulk Cementite, *Scripta Materialia* **45**, 391 (2001).
- Van Genderen M.J., Bottger A., Cernik R.J., Mittemeijer E.J., Early Stages of Decomposition in Iron-Carbon and Iron-Nitrogen Martensites - Diffraction Analysis Using Synchrotron-Radiation, *Metallurgical Transactions a-Physical Metallurgy and Materials Science* **24**, 1965 (1993).
- Van Genderen M.J., Isac M., Böttger A., Mittemeijer E.J., Aging and Tempering Behavior of Iron-Nickel-Carbon and Iron-Carbon Martensite, *Metallurgical and Materials Transactions a-Physical Metallurgy and Materials Science* **28**, 545 (1997).
- Vincent A., *Réalisation D'un Ensemble De Mesures Ultrasonores; Application à L'étude Des Défauts Cristallins Dans L'aluminium*, Ph.D. Thesis, Université Claude Bernard de Lyon, 1973.
- Vittoz B., Secrétan B., Martinet B., Frottement Interne Et Anélasticité Des Solides, *Zeitschrift für Angewandte Mathematik und Physik* **14**, 46 (1963).
- Ward R., Capus J.M., Internal Friction Effects in Martensite, *Journal of the Iron and Steel Institute* **201**, 1038 (1963).
- Weller M., The Snoek-Köster Relaxation in Body-Centred Cubic Metals, *Journal de Physique* **44**, C9 (1983).
- Weller M., Anelastic Relaxation of Point Defects in Cubic Crystals, *Journal de Physique IV* **6**, C8 (1996).
- Weller M., Point Defect Relaxations in *Mechanical Spectroscopy Q-1 2001: With Applications to Materials Science* (eds. Schaller R., Fantozzi G., Gremaud G.) (Trans Tech Publications, Uetikon-Zuerich, Switzerland, 2001).
- Wenzl H., Welter J.M., Electric Transport Properties of High-Purity Metals and Influence of Trace Impurities, *Zeitschrift für Metallkunde* **65**, 205 (1974).
- Zener C., Mechanical Behavior of High Damping Metals, *Journal of Applied Physics* **18**, 1022 (1947).
- Zener C., *Elasticity and Anelasticity of Metals* (Chicago University Press, Chicago, 1948).

Acknowledgments

It is a pleasure to thank the many people who made this thesis possible.

I am most grateful to my thesis director, Prof. Willy Benoit, for accepting me into his group and allowing me to work in such excellent conditions. But above all, I am thankful for his kindness, guidance, support and encouragement.

It would be difficult to overstate my gratitude to Daniele Mari who followed and guided my work closely. With his expertise, inspiration and endless optimism he helped me find my way.

I wish to thank Robert Schaller for passing onto me a little of his expertise and enthusiasm about mechanical spectroscopy, and Gérard Gremaud for helpful theoretical discussions and ideas. Many thanks must also go to Sybille Crevoiserat and Christian Azcoitia for the TEM images, and to Hermann Emerich and Wouter van Beek for their help with X-ray diffraction measurements at ESRF.

This work has been achieved in collaboration with UMV Vallorbe, Switzerland. I am grateful to Bruno Jouan, Géraldine Marlin and Marc Christen for the excellent contact I have had with them over the past four years and for their confidence in my work.

My measurements would not have been possible without careful sample preparation, for which I thank Antonio Gentile, Guillaume Camarda and especially Gérald Beney for spark-cutting and polishing to perfection.

I thank Bernard Guisolan for fixing everything that I broke, Alessandro Ichino for his humor and many electronics repairs and Philippe Bugnon for his help and whistling.

I owe a debt of gratitude to many doctorants, ex-doctorants and collaborators, who helped me when my French was at level zero, assisted me both at work and elsewhere, and who most of all made the atmosphere at EPFL really enjoyable. I would particularly like to thank Katharina Buß and Patrick Mayor who shared with me so much more than just the office and who were not only my colleagues, but true friends.

I am indebted to Ana Smontara and Prof. László Forró for inspiring me to do my Ph.D. in Lausanne.

Immense thanks to my big family, who let me go so far from them. I thank them for all their love and support.

And I thank Marko for driving me 6000 km and for fig. 3.21. And for everything else.

Curriculum vitae

Iva Tkalcec

born on January 27th, 1974 in Zagreb, Croatia

nationality: Croatian

Education:

- 2000-2004: Ph.D. student at EPF Lausanne, Faculty of Basic Sciences, Institute of Physics of Complex Matter under supervision of Dr. D. Mari and thesis director Prof. W. Benoit
- 2000: Diploma work “Anisotropy of thermal conductivity of $(\text{TaSe}_4)_2\text{I}$ ”, performed at Institute of Physics, Zagreb, Croatia
- 1992-2000: Physics at University of Zagreb, Faculty of Science, Croatia
- 1992: V Gimnazija, Zagreb, Croatia

Teaching:

- 2003: Assistant for “Introduction à la Métrologie”, with G. Gremaud and R. Schaller
- 2000-2003: Assistant for “Travaux pratiques des physiciens de 2eme année”, with G. Gremaud
- 2000: Assistant for “Travaux pratiques de Physique destinés aux étudiants des sections de Mécanique et de Microtechnique”, with R. Sanjines

Conferences:

- 2003: I. Tkalcec, C. Azcoitia, S. Crevoiserat, D. Mari: “Tempering effects on a martensitic high carbon steel”, oral presentation, 13th International Conference on the Strength of Materials, Budapest, Hungary
- I. Tkalcec, C. Azcoitia, D. Mari: “Tempering effects on the microstructure of martensitic carbon steel”, oral presentation, Annual meeting of the Swiss Physical Society, Basel, Switzerland

- 2002: I. Tkalcec, S. Crevoiserat, D. Mari: "Interaction between dislocations and point defects in martensitic carbon steels", poster, NATO Advanced Study Institute: Thermodynamics, Microstructures and Plasticity, Fréjus, France
- I. Tkalcec and D. Mari: "Internal friction in martensitic, ferritic and bainitic carbon steel; cold work effects", oral presentation, 13th International Conference on Internal Friction and Ultrasonic Attenuation in Solids, Bilbao, Spain
- I. Tkalcec, S. Crevoiserat, D. Mari: "Interaction between dislocations and point defects in martensitic carbon steels", poster, Colloque Plasticité 2002, Lyon, France
- Thermoelectric Phenomena in Metals and Alloys, workshop, INSA Lyon, France
- 2001: I. Tkalcec and D. Mari: "Mechanical spectroscopy in a martensitic carbon steel", poster, Mechanical spectroscopy Q-1, summer school, Aussois, France

Publications:

- I. Tkalcec, C. Azcoitia, S. Crevoiserat, D. Mari: "Tempering effects on a martensitic high carbon steel", Materials Science and Engineering A, In Press, Corrected Proof, Available online 26 June 2004
- I. Tkalcec, D. Mari: "Internal friction in martensitic, ferritic and bainitic carbon steel; cold work effects", Materials Science and Engineering A 370 (1-2), 213-217 (2004)
- I. Tkalcec, D. Mari: "Mechanical Spectroscopy in Martensitic and Cold-Worked Carbon Steels", Defect and Diffusion Forum Vols. 203-205, pp. 253-256 (2002)
- A. Smontara, I. Tkalcec, A. Bilusic, M. Budimir, H. Berger: "Anisotropy of the thermal conductivity in $(\text{TaSe}_4)_2\text{I}$ ", Physica B 316 (2002) pp. 279-282
- I. Tkalcec, A. Bilusic, H. Berger, L. Forro, A. Smontara: "Anisotropy of the transport properties of $(\text{TaSe}_4)_2\text{I}$ ", Synthetic Metals 120 (1-3): 883-884 Sp. Iss. SI MAR 15 (2001)
- I. Tkalcec, A. Bilusic, H. Berger, L. Forro, A. Smontara: Anisotropic thermoelectric properties of $(\text{TaSe}_4)_2\text{I}$, Fizika A 9 (2000) 4, 169-176